University of California
Santa Barbara

A Platform for Single Molecule Action Spectroscopy

A dissertation submitted in partial satisfaction
of the requirements for the degree

Doctor of Philosophy
in
Physics

by

Zeyun Peng

Committee in charge:

Professor David Patterson, Chair
Professor Matthew Fisher
Professor David Weld

June 2023

The Dissertation of Zeyun Peng is approved.

Professor Matthew Fisher

Professor David Weld

Professor David Patterson, Committee Chair

May 2023

A Platform for Single Molecule Action Spectroscopy

by

Zeyun Peng

To my parents, grandparents, and everyone who loves science and this world.

Acknowledgements

During the six years of my Ph.D. program, I have received invaluable help from many people. Their kindness and support helped me go through many difficult periods and eventually led me to here, completing my dissertation. I cannot express enough gratitude to them.

First and foremost, I would like to thank my advisor, Prof. David Patterson. I am so lucky that I met Dave during my first year at UCSB and gained a chance to build this brand-new lab and experiment with many great people. Dave always keeps great enthusiasm and an open mind to all kinds of experiments and ideas, inspiring everyone in the lab to go practice and test their either novel or freaky designs. He is also acknowledged enough to help us sort out thoughts and give practical advice for most of our discussions and questions. His consistent patience, support, and encouragement are even more valuable. Without the support of Dave, I could never go through the periods when the progress grew extremely slowly, as in the COVID days. The enlightenment of Dave's personality and attitude to research and life is the most important gift to me in this project.

Next, I would like to thank my main collaborators Aaron Calvin, Scott Eierman, and Lincoln Satterthwaite. We confront and overcome most challenges together in the long way of research. I received countless help from you in both work and life. I could not imagine what my Ph.D. life would be like without any of you.

I would also like to thank everyone else that has been in our lab, including and not limited to Greta Koumarianou, Merrell Brzeczek, Ce Pei, Tristan Richmond, Dylan Finestone, Luca Scharrer, Billy Murphy, Irene Wang, Ben Riley, Lia Yeh, and Simon Gan. It is such a pleasure to work together with you. Our lab is always full of laughing and fresh things that I have never heard of. They make the lab an enjoyable and lovely

place to stay in.

In addition, I would like to thank all my friends and everyone supporting me during graduate school. During these years, my friends studying here, such as Xinfeng Xie and Zhiran Zhang, shared a lot of relaxing time with me, allowing me to take a break and enjoy my life. I gained a lot of help from friends in other labs, like Mingyu Fan, and the staff members like Jennifer Farrar. It is also relaxing and enjoyable to talk remotely with all my friends living everywhere in the world. Thank you all for your time and kindness.

Finally, I would like to thank my parents and all family members for your care, love, and unconditional support. You all matter a lot.

Curriculum Vitæ

Zeyun Peng

Education

2023	Ph.D. in Physics (Expected), University of California, Santa Barbara.
2020	M.A. in Physics, University of California, Santa Barbara.
2017	B.S. in Physics, Peking University.

Publications

A. Calvin, S. Eierman, **Z. Peng (co-primary author)**, M. Brzeczek, L. Satterthwaite, and D. Patterson,"Single Molecule Infrared Spectroscopy in the Gas Phase", *Nature*, in press

S. Eierman, **Z. Peng**, A. Calvin, M. Brzeczek, L. Satterthwaite, and D. Patterson, "A Cryogenic Ion Trap for Single Molecule Vibrational Spectroscopy", *Review of Scientific Instruments*, in press.

Abstract

A Platform for Single Molecule Action Spectroscopy

by

Zeyun Peng

Spectroscopy is a key analytical tool that provides valuable insight into molecular structure and is widely used to identify chemical samples. Action spectroscopy combines spectroscopic methods with mass spectrometry, enabling the analysis of low-density gas phase molecular ions. So far, commonly reported action spectroscopy techniques destructively record spectra of ensembles of molecular ions, where the presence of multiple chemical and isomeric species greatly complicates the interpretation of the spectra. Here, we extend the action spectroscopy to the purest possible sample: a single gas phase molecule. The resulting single molecule vibrational spectroscopy is initially demonstrated by the first recorded spectrum of a single gas phase polyatomic molecule to our knowledge.

This thesis presents the experimental setup, method, and results of the achieved single molecule vibrational spectroscopy. The apparatus centers around a cryogenic ion trap, where a single molecular ion is confined after being mass-selected by a quadrupole mass filter. A laser-cooled $^{88}Sr^{+}$ ion is co-trapped with the molecular ion. The two ions are sympathetically cooled to a Coulomb crystal at milliKelvin temperatures. We developed nondestructive mass spectrometry based on the crystal's secular motion frequencies. This technique enables "tagging" spectroscopy with a single molecular ion, where vibrational transitions are monitored by a N_2 tag. The single molecule vibrational spectra are deduced based on the vibration-induced de-tagging rate. We showed this single molecule vibrational spectroscopy is generalizable to a broad class of molecular ions and is a powerful analytical tool for the nondestructive identification of single molecules.

Contents

Chapter 1

Introduction

The eye is a door to bring in the light. Human beings' knowledge is mainly acquired with the help of light, a unique type of electromagnetic wave in the narrow visible frequency range. A vast amount of information can be hidden in this frequency space, to which the sense of color provides a clue. Since Issac Newton split light with a prism, the frequency-dependent studies and experiments have evolved into a giant field, which is now known as spectroscopy. These spectroscopy experiments have greatly shaped our understanding of the world, from the early days of identifying the chemical elements to the latest tests of theories beyond the standard model with precision spectroscopy. Remarkably, it is the observation of the hydrogen spectral lines that led to the discovery of the Bohr model and the energy levels, which finally opened the door to the world of quantum physics. Nowadays, we know the frequency of light is directly related to the energy of a single photon by the Planck constant, following $f = E/h$. During the photon absorption and emission process, the coupling between the matter's quantum levels via the electromagnetic field follows the energy conservation law. The frequency of the interacting photons commonly corresponds to the energy difference between the quantum levels, which enables a general spectroscopic method to study the internal

energy structure of matter. This thesis focuses on a novel gas-phase single molecule vibrational spectroscopy method we designed and the experimental platform we built for it.

Today, the field of spectroscopy has been extended to almost everywhere in our life. Its research targets range from the tiny nuclei to the galaxies, from the simple two-level systems to the strongly interacting condensed matter systems. The frequency varies from the radio frequency to the gamma-ray frequency. The spectroscopic methods are widely used for studying internal energy structures, identification, and detection. A significant part of the spectroscopic methods directly detect the absorption, scattering, or emission signals. Nevertheless, detecting those radiation signals is not always possible, especially if the analyte sample is at low density and lacks efficient transitions. An alternative spectroscopic method called action spectroscopy (or consequence spectroscopy) enables the measurement in these cases, where the light-matter interaction is detected via the consequence of the interaction on the matter rather than light. Action spectroscopy is found to be a powerful tool for probing the electronic, vibrational, and rotational transitions of gas-phase molecular ions, where Coulomb repulsion prevents the forming of high-density samples.[1] These measurements are usually achieved based on mass spectrometry, where a mass shift of the analyte ion caused by the light-matter interaction is destructively detected.

Molecules and molecular ions are complicated and fascinating quantum systems containing multiple nuclei and electrons. The nuclei and electrons are held together by the Coulomb interaction, forming covalent bonds and different molecule structures. Their structures and properties are essential research topics in chemistry. The various compositions and the enriched structures of molecules lead to a tremendous amount of molecular species, which enables the construction of all lives and this colorful world. For polyatomic molecular systems, different stable structures may exist with the same composition (the

same molecular formula). They are called isomers. Due to the heavy masses of the nuclei, the isomers may have a near-zero tunneling probability through the potential barrier to the ground state, resulting in a practically permanent lifetime. These stable or meta-stable isomers are commonly observed in organic chemicals.

The isomers may have distinct chemical and physical properties, offering great potential for various of applications. However, the existence of isomers sometimes causes issues. To better understand the nature of the chemicals, the properties of isomers shall be measured individually, but they usually co-exist as a mixture experimentally. In the mass spectrometry-based experiment, an ion ensemble is needed for analysis. They are typically generated by the ionization of neutral molecules. The isomeric ions are commonly produced together and are hard to be separated due to their same mass. Although the ion mobility spectrometry (IMS) and the "hole-burning" method offer possibilities to separate them[2, 3, 4], isomerically pure ion ensembles are generally hard to obtain for further analysis. Existing action spectroscopy techniques typically record spectra of ensembles of molecular ions, where the presence of multiple isomeric species greatly complicates the interpretation of the resulting spectra. This issue motivates our extension of the action spectroscopy to the purest possible sample: a single gas phase molecule. It gives birth to our single molecule vibrational spectroscopy, demonstrated by the first recorded spectrum of a single gas phase polyatomic molecule to our knowledge. This approach enables the nondestructive identification of single molecules, which provides a new analytical tool for multi-component mixtures analysis, cold chemical dynamics analysis, and rare sample characterization.

Taking a step back, the single molecule experiment is also of interest from the view of quantum physics. The molecules and molecular ions, in particular, can be attractive quantum systems for multiple unique features, including the enriched energy structures in different frequency regions, large internal electric field, high sensitivity to symmetry

violating physics, and a variety of molecular symmetries as well as chirality. Benefiting from the trapping and laser cooling technique, physicists managed to isolate and confine atoms and atomic ions, where ground-state cooling and robust manipulation are achieved for multiple atomic species.[5, 6] These well-developed systems are ideal platforms for studying atomic systems and light-matter interaction. These techniques enable quantum simulation with ultracold atom gas, high-precision spectroscopy for time standard and testing the physics theories beyond the standard model, the development of sensitive sensors, and trapped ion quantum computers. These experiments commonly require suitable electronic transitions for efficient laser cooling and detection. Nevertheless, more atoms and almost all the molecules lack such a transition. Molecules and molecular ions, in particular, can not be efficiently cooled by laser due to the commonly non-zero overlapping (Franck-Condon factors) between vibrational wave functions at different electronic states.[7] A method called sympathetic cooling is developed to cool these atoms, molecules, and ions.[8, 9, 10] The sympathetic cooling is achieved by the interaction with nearby directly laser-cooled atoms or ions. For ions in particular, two ions are typically co-trapped in a Paul trap, where the Coulomb interaction strongly couples their translational motions. This setup has been employed by quantum logic spectroscopy, which has been a fruitful area of research for over a decade.[11, 12, 13] The pure quantum state preparation and manipulation of single molecular ions has been achieved with this method but so far is limited to the diatomic molecular ions.[12, 14, 15] We were enlightened by these experiments and employed a similar experimental setup to achieve our single molecule vibrational spectroscopy.

In our experiment, we produce molecular ions via electron impact ionization and load one of them at a time to a cryogenic linear Paul trap. The molecular ion is co-trapped with and sympathetically cooled by a laser-cooled $^{88}Sr^{+}$ to a translational temperature at the milliKelvin level. The two co-trapped ions form a two-ion Coulomb crystal, where

the trapping lifetime of the molecular ion can reach more than a few days. At the same time, the rotational and vibrational temperature of the molecular ion is cooled by the cryogenic buffer gas to about 8 K. We adapt non-destructive mass spectrometry methods that are uniquely possible with the laser-cooled Coulomb crystals[16], and we apply these tools to perform action spectroscopy with single molecules. The traditional version of our action spectroscopy method is called cryogenic ion vibrational predissociation (CIVP)[4] or "tagging" spectroscopy, in which an inert neutral tag molecule (RG) is attached to the analyte molecular ion (A^+) to monitor the vibrational transitions. If one of the vibrational transitions associated with A^+ is coherently driven, the tag RG will readily dissociate:

$$A^+ \cdot RG + h\nu \rightarrow A^+ + RG \tag{1.1}$$

In our single molecule vibrational spectroscopy, the presence and absence of the tag is monitored by our non-destructive mass spectrometry. The repeated de-tagging measurements enable us to deduce the frequency-dependent de-tagging rate analogous to the absorption spectra.

Our single molecule vibrational spectroscopy is generalizable to a broad class of molecular ions. Similar to the traditional "tagging" spectroscopy, our method features far greater sensitivity than other action spectroscopy methods[4] and does not rely on any specific properties or transitions of the molecule. Moreover, our method's single molecule sensitivity provides absolute isomer-selectivity, and the long lifetime of the ions enables the detection of weak spectral features. Our obtained vibrational spectra enable the characterization of the molecule structure and the identification of the molecule species. As a result, our single molecule vibrational spectroscopy is a general analytical tool for single molecular ions. Our apparatus is compatible with quantum logic spectroscopy and can be potentially upgraded to achieve pure-state preparation and manipulation of single

polyatomic molecules. It is also a promising tool for chemistry analysis, such as analyzing ion-neutral reactions and photon-dissociation processes. In this thesis, I will introduce the experimental platform and techniques we designed for single molecule vibrational spectroscopy and several experimental results.

During the six years of my Ph.D. program, my labmates and I designed, constructed, and tested this whole experiment from sketches. It has been an exciting period to adjust and witness everything from not working to performing as expected, and finally, we see the signals caused by only one molecule absorbing one photon. E. Schrödinger wrote in 1952: "... we never experiment with just one electron or atom or (small) molecule." Now we can cross the gas-phase polyatomic molecule from the list. I am so glad I have had the opportunity to participate in this project, working, learning, and exploring with everyone in the lab.

1.1 Dissertation Overview

Chapter 1 briefly discusses the background of single molecule spectroscopy and our achievement. **Chapter 2** reviews the background theories and related experiments. **Chapter 3** introduces the experimental setup we built for the single molecule vibrational spectroscopy. **Chapter 4** introduces the three basic experimental techniques employed in single molecule vibrational spectroscopy, including the two-ion crystal preparation, nondestructive mass spectrometry, and tagging method. **Chapter 5** reviews the spectral results of the single molecule vibrational spectroscopy. A part of this chapter is reproductions of the articles I co-authored. The first result is expected to be published in the article "*Single Molecule Infrared Spectroscopy in the Gas Phase*". **Chapter 6** contains a brief overview of our experiments and discussions about the future of single molecule vibrational spectroscopy. The appendices include a collection of technique notes

about some side projects and studies I was involved in.

1.2 Permissions and Attributions

1. The experimental setup is the result of a collaboration with Aaron Calvin, Scott Eierman, Lincoln Satterthwaite, Merrell Brzeczek, Ce Pei, and David Patterson.

2. The content of section 5.1 and section 5.2 is the result of a collaboration with Aaron Calvin, Scott Eierman, Lincoln Satterthwaite, Merrell Brzeczek, and David Patterson, and has previously appeared in *Nature* ("Single Molecule Infrared Spectroscopy in the Gas Phase", in press). It is reproduced here with the permission of Springer Nature: `https://www.nature.com/`

3. The content of chapter 3 and section 5.4 is the result of a collaboration with Scott Eierman, Aaron Calvin, Lincoln Satterthwaite, Merrell Brzeczek, and David Patterson, and has previously appeared in *Review of Scientific Instruments* ("A Cryogenic Ion Trap for Single Molecule Vibrational Spectroscopy", in press). It is reproduced here with the permission of AIP Publishing: `https://publishing.aip.org/`

4. The spectroscopic data in section 5.3 is the result of a collaboration with Aaron Calvin and Samuel Kresch.

5. Figure 2.1 is reprinted with permission from [17]. Copyright 1986 American Chemical Society.

6. Figure 2.2 is reprinted with permission from [4]. Copyright 2014 American Chemical Society.

7. Part of the spectroscopic data in figure 5.13 is measured and provided by Prof. Michael A. Duncan and his group. Reprint(adapted) with permission from [18].

Copyright 2018 American Chemical Society.

8. The content of Appendix C is the result of a collaboration with Ce Pei and David Patterson.

9. ComponentLibrary by Alexander Franzen is licensed under a Creative Commons Attribution-NonCommercial 3.0 Unported License.

Chapter 2

Chapter 2 Background

In this chapter, we will go through some fundamental theories and concepts of the quadrupole ion trap, molecular spectroscopy, action spectroscopy, and quantum logic spectroscopy.

2.1 Quadrupole Ion Trap

Quadrupole ion trap (Paul trap or radio frequency trap) and quadrupole mass filter are both designed based on the fact that the charged particles can be stabilized at the saddle point of an oscillating electric field at radio frequency. The motion of the particles near the saddle point is characterized by the Mathieu equations. [6]

2.1.1 Mathieu Equation and Paul Traps

It is well-known that a charged ion can not be stably trapped in a charge-free static electric field due to Gauss's flux theorem. Wolfgang Paul and his colleagues found an alternative way to trap the ions with an alternating electric field in the mid of last century, the setup of which is now known as the quadrupole ion trap or Paul trap. The charged

ion's motion in a Paul trap is mainly driven by the electric field. In general, the electric field consists of two components, the static (or quasi-static low-frequency) field and the radio frequency (rf) field. The charged ion tends to oscillate near the saddle point of the rf field but is also driven by the static field. Assuming a zero static electric field intensity at the saddle point of the rf field, the electric potential near the saddle point can be approximately described by the quadrupole terms:

$$\Phi(\vec{r},t) = U(\alpha x^2 + \beta y^2 + \gamma z^2) + V\cos(\Omega_{rf}t)\frac{1}{2}(\alpha' x^2 + \beta' y^2 + \gamma' z^2) \tag{2.1}$$

Ω_{rf} is the angular frequency of the rf field. The potential has to follow the the Laplace equation $\Delta\Phi(r,t) = 0$ for all the r and t, which leads to restrictions in the geometric factors,

$$\alpha + \beta + \gamma = 0, \quad \alpha' + \beta' + \gamma' = 0 \tag{2.2}$$

Different choices of geometric factors represent various geometries of the Paul traps. For cylindrical ion traps,

$$\alpha = \beta = \gamma = 0, \quad \alpha' + \beta' = -\gamma' \tag{2.3}$$

For linear Paul traps,

$$-(\alpha + \beta) = \gamma > 0, \quad \alpha' = -\beta', \quad \gamma' = 0 \tag{2.4}$$

For quadrupole mass filter,

$$\alpha = -\beta, \quad \gamma = 0, \quad \alpha' = -\beta', \quad \gamma' = 0 \tag{2.5}$$

The ion's three-dimensional motions along x, y, and z axes in the electric field are

decoupled and, therefore, can be analyzed individually. Taking the motion in the x direction for instance, the motion of an ion with mass m and charge Q follows,

$$\ddot{x} = -\frac{Q}{m}[U\alpha + V\alpha' \cos(\Omega_{rf} t)] \tag{2.6}$$

where we can define the Mathieu parameters a_x, q_x, and the nondimensionalized time t:

$$a_x = \frac{4QU\alpha}{m\Omega_{rf}^2}, \quad q_x = \frac{2QV\alpha'}{m\Omega_{rf}^2}, \quad \xi = \frac{\Omega_{rf} t}{2} \tag{2.7}$$

Now the equation of motion is transformed to the form of the Mathieu differential equation,

$$\frac{\mathrm{d}^2 x}{\mathrm{d}\xi^2} + [a_x - 2q_x \cos(2\xi)]x = 0 \tag{2.8}$$

This motion has been studied with both numerical simulations and the Floquet theorem.[19, 20] Notably, the stability of the motion and the nondimensionalized period $\frac{\Omega_{rf} T}{2}$ of the secular motion only depend on the two Mathieu parameters. The parameter space (q_x, a_x) where the stable confinement is achieved (stability region) is shown in the stability diagram.[21]

When the three pairs of Mathieu parameters in all three dimensions are in the stable region, the ion is stably trapped in the electric field. In our experiment, we adopt the linear Paul trap geometry. We typically let the radial Mathieu parameters stay at the center of the lowest stable region to achieve robust trapping.

The quadrupole mass filter has a similar geometry to the linear Paul trap but without a static axial confinement. In a quadrupole mass filter, the rf field only exists along the radial directions. If the radial confinement is stable, the ion can move along the central axis of the quadrupole mass filter. Otherwise, the radial oscillation of the ion will be amplified, and the ion will be removed. Note that the ratio between the Mathieu

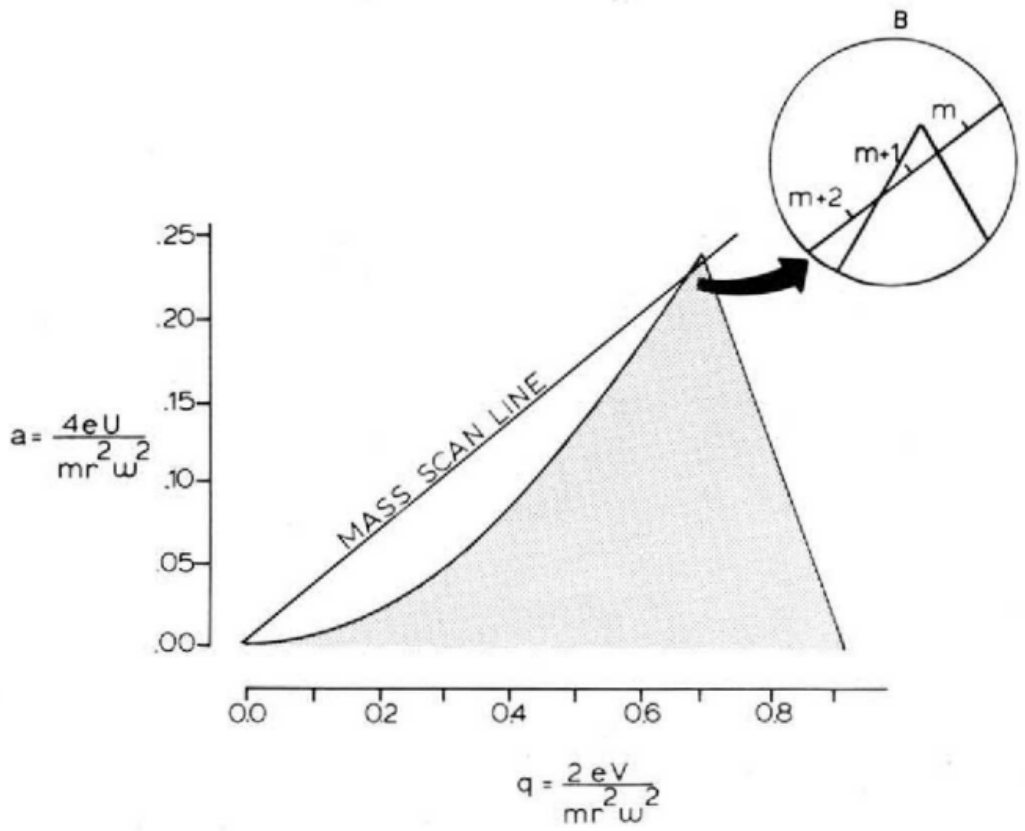

Figure 2.1: The a-q stability diagram. The shaded area represents the lowest stable region. **B**)The one amu bandpass mass filter: Only the ions with a mass-to-charge ratio at $m + 1/e$ fall within the stability diagram. Reprinted with permission from [17]. Copyright 1986 American Chemical Society.

parameters a and q is independent of the ions. The parametric equation $(q_r(m), a_r(m))$ gives a straight line crossing the origin in the parameter space. The slope of the line is controlled by $\frac{U\alpha}{V\alpha'}$. The field intensity U and V can be adjusted so that only the ion in a narrow mass range is stably confined, where the linear quadrupole field will act as a mass filter. Currently, the commercial quadrupole mass filters can achieve a mass resolution better than 0.3 Dalton.

2.2 Electric Dipole Transition

Electric dipole transitions are usually the dominant term of the light-matter interaction when they are allowed. These transitions enable Doppler cooling, coherent manipulation, and the observation of absorption and emission spectra of the atoms and molecules. The semi-classical model of a two-level system commonly covered in textbooks (for example, see in Foot (2004)[22], Demtrö der(2010)[23]) well describes the stimulated and spontaneous emission processes when a laser drives the transition. This model can be applied to explain the transitions of both atomic and molecular systems. The single-molecule vibrational transitions measured in this thesis are mostly electric dipole transitions and follow the selection rule of electric dipole transitions.

2.3 Molecular Transition and Spectroscopy

The Hamiltonian of a molecular system consists of the electron's kinetic energy, the nuclei's kinetic energy, and the Coulomb potentials. This complicated quantum system is generally analyzed with the Born–Oppenheimer (BO) approximation. Under the BO approximation, the electrons always stay at a specific electronic state while the nuclei move around, resulting in an effective potential (Born–Oppenheimer or adiabatic potential energy surfaces) for the nuclei depending on the particular electronic state. The nuclei motion is further separated into vibrational, rotational, and translational motions. As a result, the internal quantum state of the molecule can be marked by the electronic, vibrational, and rotational quantum numbers $n, \nu, J(, m, K)$. Based on the changes in these quantum numbers, the molecular transitions and spectra can be divided into three categories: electronic, vibrational, and rotational.

Molecular electronic transitions typically have frequencies higher than 240 THz (1 eV

or 8000 cm^{-1}). These transitions are not observed in our spectra but are related to photo-dissociation and direct laser cooling. The high energy scale of these transitions leads to a natural line width above MHz, similar to the electronic transitions of the atoms used for laser cooling. However, the molecular electronic transitions do not have a restricted selection rule for the vibrational quantum numbers. The spontaneous emission probability depends on the overlap of the vibrational wave functions, known as the Franck-Condon factor. The Born–Oppenheimer potential energy surfaces are typically different at different electronic states. Thus the Franck-Condon factors are usually not zero, leading to vibrational heating during the spontaneous emission process. This fact makes it nearly impossible to achieve efficient laser cooling. In addition, the varied potential energy surface at the excited state may lead to photo-dissociation and photo-isomerization of stable molecules.

Molecular vibrational transitions are what we observed in the single molecule vibrational spectra. These transitions are typically observed at the electronic ground state. The rotational quantum number may change during the vibrational transitions, so these transitions are also called ro-vibrational transitions. The selection rule of these transitions varies based on the molecule's symmetry, but in general, $|\Delta J|$ is no more than 1. The vibrational excitation energy (10 - 120 THz or 300 - 4000 cm^{-1}) is typically larger than the rotational energy scale, so the ro-vibrational transitions of a specific vibrational excitation are usually observed together in the vibrational spectra forming a vibrational band (see in figure 5.9). The frequency of the vibrational band strongly depends on the related vibrating structure and chemical bonds, so the vibrational spectra are extensively used to study the molecules' structures.[4]

The pure rotational transitions of the molecules are typically observed at microwave frequencies. These transitions are not observed in our work but naturally exist due to the background black-body radiation. In the cryogenic environment of our experiment,

all the electronic and vibrational modes of the molecule are frozen in the absence of the lasers, but the rotational motion is still excited.

2.4 Action Spectroscopy

In this section, I will focus on the traditional gas-phase action spectroscopy. Action spectroscopy methods are widely used to measure the electronic, vibrational, and rotational spectra of mass-selected molecular ions in the gas phase. A detailed summary of the action spectroscopy techniques can be found in the review articles.[1, 4]

The absorption of a photon typically behaves as a mass shift of the molecular ions in action spectroscopy. This mass shift can be caused by photo-dissociation, light-induced reaction, tagging photo-dissociation, or laser-induced inhibition of complex growth (LIICG). The photo-dissociation and light-induced reaction will change the chemical bond structure and, therefore, destroy the molecule. In the latter two methods, on the contrary, the mass difference results from the presence and absence of a loosely attached neutral particle (tag). The tag can be bound to the ion via ion-induced dipole interaction, forming a van der Waals complex, where the molecule's chemical bonds are barely affected. When the molecule is vibrationally or electronically excited, the van der Waals bond will be destroyed or be prohibited from forming. With tagging photo-dissociation method, molecular ions are tagged at first and then de-tagged with a laser. The transition frequency is disturbed by the ion-tag interaction, but the spectral lines are broadened and easily detected. It has been demonstrated that this "Tagging" spectroscopy features far greater sensitivity and flexibility than other action methods. For vibrational spectroscopy in particular, this method leads to cryogenic ion vibrational predissociation (CIVP) spectroscopy. On the other hand, the LIICG method features an undisturbed transition frequency and a narrow linewidth, typically used in rotationally resolved high-

precision spectroscopy. Our experiments adopt the tagging photo-dissociation method for its nondestructive nature to the molecular ion and high sensitivity.

The mass of the ions is typically determined by time of flight (TOF) or quadrupole mass spectrometry in traditional action spectroscopy. During the experiment, the ions are shuttled through multiple mass-selection equipment and the experimental area. Only the ions with the selected mass can pass through the mass-selection equipment and reach the detector that reads out the ion flows. Figure 2.2 shows a typical apparatus for action scpectroscopy.

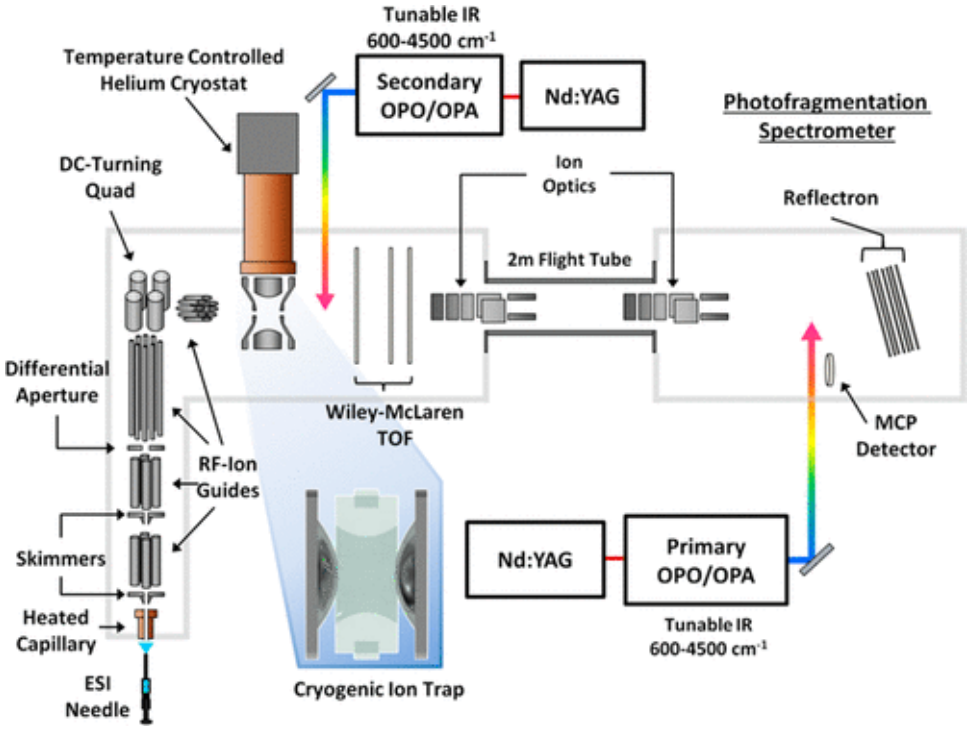

Figure 2.2: In the Yale tandem time-of-flight photofragmentation spectrometer, ions are extracted from solution with electrospray ionization (ESI) and guided into a 10 K 3D quadrapole ion trap. After collisional cooling, ions are extracted from the trap and mass selectively (to unit m/z) interrogated by one or two pulsed infrared lasers. Reprinted with permission from [4]. Copyright 2014 American Chemical Society.

The TOF and quadrupole mass spectrometry allow the traditional action spectroscopy experiments to take data efficiently every 0.1 s but will destroy the analyte ions after

each measurement. These methods also require an ion ensemble for detection. Hence, they are not suitable for single-molecule experiments. In section 4.2, I will introduce the nondestructive mass spectrometry methods we developed to replace the TOF and quadrupole mass spectrometry for single molecule vibrational spectroscopy.

2.5 Quantum Logic Spectroscopy

Quantum logic spectroscopy is a general method for precision spectroscopy of ions without suitable transitions for laser cooling. This technique was developed in early this century.[24] It has been applied to study the transitions of atomic and diatomic ions.[11, 12, 25]

In quantum logic spectroscopy, a single analyzed "spectroscopy" ion is co-trapped with a laser-cooled "logic" ion in a linear Paul trap, forming a two-ion crystal. The Coulomb interaction couples the motions of the two ions, which enables the sympathetic cooling of the normal modes of the crystal.[10] At the start of the experiment, the logic ion sympathetically cools the whole crystal to the translational ground state. A quantum logic operation maps the possible internal excitation of the spectroscopy ion to a shared translational mode and finally to an internal mode of the logic ion available for readout.[24] The process is realized by coherently driven sideband transitions, which couple an axial motional mode of the crystal to the internal transitions of each ion.

Quantum logic spectroscopy can precisely determine the transition frequency of the spectroscopy ion but could be hard to apply if the transition frequency of the spectroscopy ion is unknown. Therefore, quantum logic is invaluable for fundamental physics and precision measurement experiments, but impractical as a tool for chemical analysis. Our novel single molecule approach, however, is technically simple to implement and generalizable to a broad class of polyatomic ions.

Chapter 3

Chapter 3 Experimental Setup

In this chapter, we will focus on the experimental setup employed in this work for realizing gas phase single molecule infrared spectroscopy. The primary apparatus is constructed centering around a cryogenic ion trap in our main chamber, where the ions are confined during the experiment. Multiple designs used in cryogenic ion trap experiments and action spectroscopy are adjusted and combined in our setup. As shown in Figure 3.1, the sub-systems surrounding the main chamber enable the controls of the ions and the experimental environment. The main components include the cryogenic system, the vacuum system, the laser system, the imaging system, and the ion generation system (the Extrel Chamber). In the following sections, we will review these components individually.

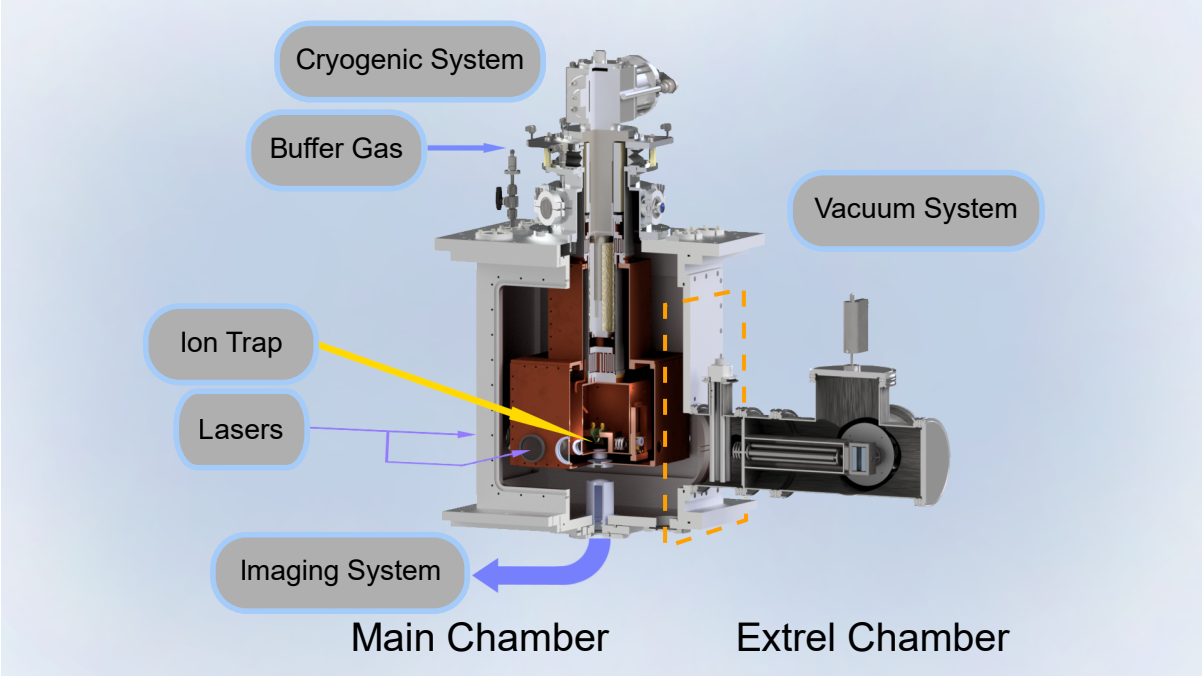

Figure 3.1: Overview of the experimental setup

3.1 Cryogenic System and Vacuum System

A well-controlled thermal and vacuum environment is essential for single molecular ion experiments. Unlike atomic ions and some small diatomic molecules, most polyatomic molecules have enriched and complicated rotational manifolds. Those rotational modes, as well as low energy vibrational modes and Van der Waals bonds, which have an energy scale between GHz and 30 THz, are sensitive to the room temperature black-body radiation and the collisions with the neutral molecules. Moreover, reactive collisions with background gas could dramatically shorten the lifetime of the ions. To avoid those problems, we employ a cryogenic ion trap design and obtain an ultra-high vacuum (UHV) and cryogenic environment. In this section, we will discuss how our main chamber, the vacuum system, and the cryogenic system collaborate to achieve the goal.

3.1.1 Cryogenic System

The cryogenic system consists of a Gifford-McMahon style (GM) cryocooler system (Sumitomo SRDK-415D) and an ultra-low vibration interface from Coldedge Technologies Inc. The GM-style cryocooler uses high-pressure helium as the working fluid shuttled between the cold head and a water-cooled compressor. During a full cooling cycle of about 1 s, helium undergoes a compression and expansion cycle and takes up heat from the cold stage.[26] The process efficiently cools the cold stage but causes persistent vibration. To minimize the impact of this vibration, the low-vibration interface is used to connect the cold head and the experiment platform. It provides an excellent thermal connection while isolating the mechanical vibration.

As shown in Figure 3.2, the SRDK-415D cryocooler has two cold stages. The first stage provides a high cooling power of 40 W at 45 K; the second state has an ultimate temperature of 3.2 K, while it only has a low cooling power of 1.5W at 4.2 K.

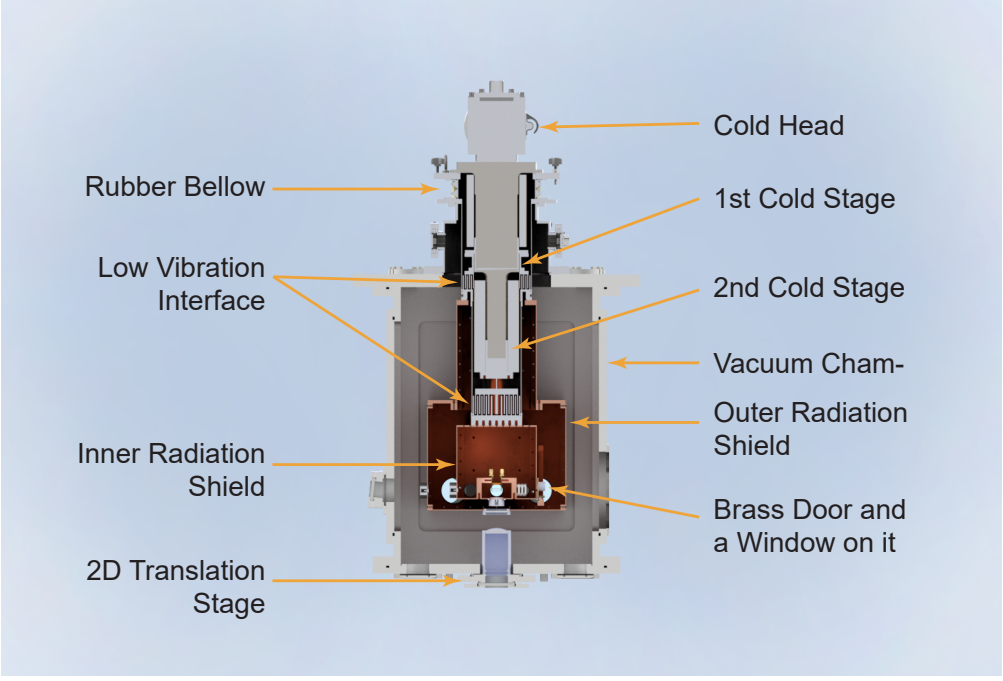

Figure 3.2: A cross-sectional view of the SRDK-415D cryocooler and the main chamber

The low vibration interface consists of two metal parts connected with a rubber bellow. The two parts are hard connected to the cold stages and the experiment chambers, respectively. They are mechanically decoupled from each other, while they have mating fringes-like structures creating a narrow gap in between. Ultra-high purity (UHP) helium gas is used to fill the gap, and the collisions of the gas provide an efficient thermal link between the two parts. We typically run the second cold stage above 4.2 K to prevent the UHP helium from condensing. In this case, the displacement of our experiment chamber is reduced from a typical value of about 25 μm[27] to a few μm level.

3.1.2 Main Chamber

As illustrated in Figure 3.2, the main chamber of our apparatus has a three-layer structure, including an aluminum cuboidal vacuum chamber, an outer radiation shield, and an inner radiation shield. The aluminum chamber can hold a vacuum as low as 2×10^{-8} Torr. The outer and inner radiation shields are not vacuum tight but can thermal-isolate the ion trap from the room temperature environment.

The vacuum chamber is 24 inches tall, 17 inches wide, and 13 inches deep. It consists of an aluminum frame and five customizable aluminum panels that maximize the flexibility and compatibility of the setup. The top of the chamber frame mates the cryocooler via an ISO-160 flange, and the other five faces are sealed by the panels with Viton© fluoroelastomer o-rings. The o-ring face seals sacrifice the vacuum tightness compared to the knife edge seals but enable the use of aluminum parts that can be customized and rapidly fabricated in-house. Such a design achieves a leak rate lower than 10^{-9} mbar·L/s . And when all the pumps and the cryocooler are on, the chamber can reach 2×10^{-8} Torr. The main chamber provides plenty of KF HV flanges for vacuum devices and feedthroughs, as well as seven viewing ports. In addition, an ISO 160 port for our primary high-speed

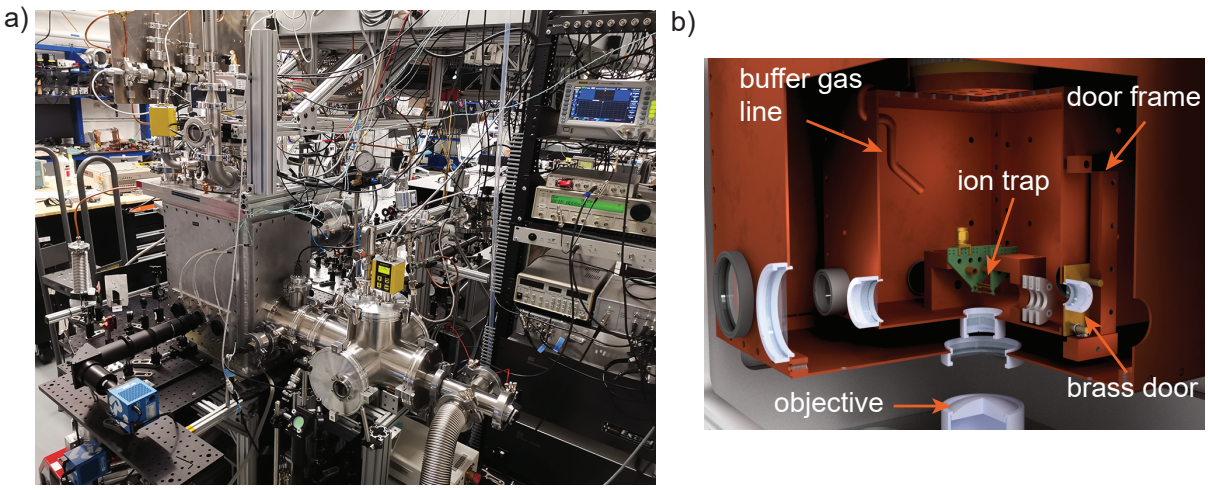

Figure 3.3: a) A photo of the main chamber. A large turbo pump (Agilent TV 551, 500 l/s) is mounted on the back panel. The 80/20 frame on the top is extended from the cloud and holds the cold head above the main chamber. The 80/20 frame at the bottom fixes the main chamber to the optical table. b) The three-quarter section view of a CAD model of the inner and outer radiation shields. The ion trap is hold by a pair of copper stands at the center. The copper tube pointing toward the trap is the gas line for buffer gas cooling and tagging experiment. The yellowish part on the right is a brass door. It is confined in a frame made of OFHC copper bars and can only move up and down.

turbo pump and a 2D translation stage for the primary objective are also fabricated on the panels.

The outer and the inner radiation shields are mounted on the interfaces thermal-connecting to the two cold stages separately. They are made of oxygen-free high-conductivity (OFHC) copper. OFHC copper panels are bolted to two frames constructed with OFHC copper bars with Belleville washers to maintain high contact pressure and good thermal contact while they reach a cryogenic temperature. High thermal conductivity Apiezon N grease is applied in between the contact surface to further improve the thermal behavior. The two radiation shields are well-thermalized to the cold stages, and their temperature is monitored with silicon diode sensors.

The outer radiation shield is typically cooled to about 60 K during the experiment. It shields the inner radiation shield from the room temperature environment, blocking

most of the room temperature gas molecules and the black-body radiation. It also acts as a heat sink that pre-cools all cables and a gas line before they reach the inner shield region. Such a design greatly reduces the second cold stage's thermal load and helps achieve a lower temperature inside the inner shield. Seven 2-inch diameter high thermal conductivity sapphire windows and a 1-inch one are attached to the outer radiation shield with standard anodized aluminum lens tubes from Thorlabs Inc. They have a high optical transmission for light in the wavelength range between 200 nm and 5 μm providing good optical access to the ion trap while still blocking most of the room temperature black-body radiation that peaks at 10 μm. Only a 1-inch diameter hole is left for sending in the ions.

The inner radiation shield creates an enclosed cryogenic volume for the experiment. The ion trap is mounted right above the center of the inner radiation shield's bottom panel. The inner shield provides the ion trap with better shielding than the outer radiation shield, with a total cross-section of gaps and holes smaller than 0.5 cm^2. And there is no direct path from the outside to the center of the ion trap. Nine sapphire windows are secured in Thorlabs' vacuum-compatible lens tubes with spring washers. Such lens tubes have no anodized layer and provide better thermal contact. When the inner shield is stabilized at the normal operating temperature of 5.7 K, the temperature at the window center is measured to be 7 K. There is a 1-inch hole on the path of the ion loading trajectory, which is normally covered by a cold brass door with a 12.7 mm sapphire window. The brass door acts as a mechanical shutter. When ions are loaded, it is raised by a stainless steel cable, which exposes the ion trap to the ion source. This motion is controlled by a linear motion feedthrough that pulls the cable attached to the door. During the other time, the door is held closed by springs, keeping the inner volume isolated.

3.1.3 Vacuum System

A set of mechanical vacuum pumps are used in our experimental setup. It includes a primary high-speed turbo pump (Agilent TV 551) backed by a dry scroll pump, two combination pumping stations (Pfeiffer HiCube Eco 80), and another dry scroll pump (Agilent IDP-07, 2.5 l/s) used as a roughing pump. The Agilent TV 551 is directly mounted onto the main chamber and has the largest pumping speed (500 l/s). The two pumping stations each have a pumping speed of 67 l/s and are connected to the main chamber with bellows. For reference, the inner volume of our whole vacuum chamber is about 100 liters. The lowest pressure that can be reached with this pump set alone and without baking is about 8×10^{-7} Torr. It is mainly limited by the outgassing. The pressure is monitored with an ion gauge (InstruTech IGM401) fixed on the room-temperature main chamber.

On the basis of the high vacuum achieved with the mechanical pumps, the cryo-pumping effect can further improve the vacuum in our chamber to the UHV regime. At cryogenic temperatures, the cryogenic surface (in our case, mainly the radiation shields) efficiently cryo-pumps the gas species with low vapor pressures.[28] When the radiation shields are well-cooled by the cryocooler, the outer radiation shield stays below 65 K, and the inner shield typically stays at 5.7 K. A significant amount of gas species, such as water vapor, carbon dioxide, and organic molecules (except methane), would start to condense at the outer radiation shield. And at the inner radiation shield's temperature, only helium isotopes and hydrogen isotopes could maintain a non-negligible pressure. If the temperature is slightly increased to around 14 K, neon gas could also exist. When cryo-pumping and the mechanical pumps work together, the readout of the ion gauge on the main chamber can reach 2×10^{-8} Torr. And we expect the inner radiation shield region has a similar or lower pressure at 6 K. It results in a typical mean free time between

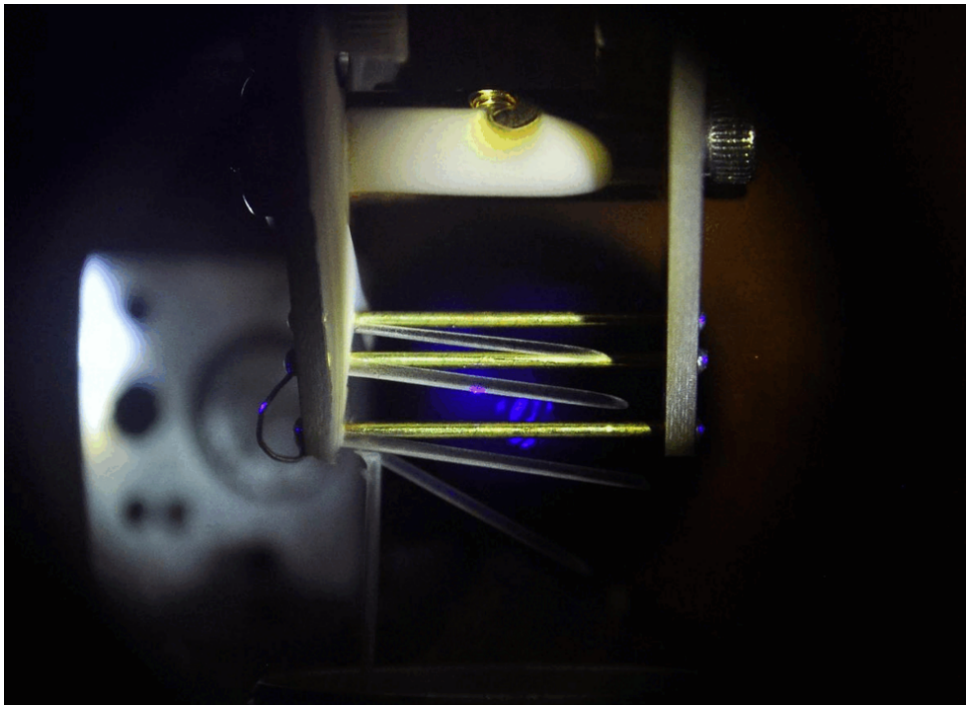

Figure 3.4: A layer of neon ice starts to fall from the ion trap when the system is warmed up to 20 K.

0.01 s and 1 s for a single ion rest at the trap center.

Although the cryo-pumping effect has an overwhelming pumping efficiency, it has a finite pumping capacity. As the gas is removed from its gas phase, it condenses at the cryogenic surface and becomes ice. We have observed a macroscopic layer of neon ice that forms on the ion trap as we constantly puff in neon to the inner shield. Figure 3.4 shows the moment the neon ice layer collapses around the phase transition temperature. The ice layer could not only potentially block the beam path of the laser and the hole used for ion loading but also create an insulation surface where charges can accumulate and cause a stray electric field, which may affect the ion trap's performance. As the system approaches the pumping limit, a warm-up cycle back to room temperature is performed to reset the system.

3.1.4 Cool-down and Warm-up Procedure

The cool-down and warm-up procedures of our experiment are described in this section. The warm-up process takes about 20 hours, and the cool-down process takes about 12 hours. Such a fast warm-up and cool-down cycle helps rapid resets and fast iterative development of our experimental design. Our apparatus can test a new trap or a new experimental design within an operating cycle of a few days and be ready for further adjustment again.

To cool down the system, the chamber is first pumped to 50 mTorr from atmospheric pressure by the roughing scroll pump (Agilent IDP-07, 2.5 l/s). Then the two combination pump stations (Pfeiffer HiCube Eco 80) and the high-speed turbo pump (Agilent TV 551) take the job and further pump the chamber down to 5×10^{-6} Torr. The roughing pump is blocked by a right-angle valve from this point. This procedure takes about two hours and can be extended if a better vacuum and cleaner environment are desired. After reaching a high vacuum, the cryocooler is then turned on and cools the system. Figure 3.5 shows the temperatures at different parts drop and stabilize over time. The system will be ready for experiments in 10 hours after the cryocooler is turned on.

The warm-up procedure starts by turning off the cryocooler. The inner radiation shield usually reaches 20 K in 10 minutes. If an intensive amount of neon has been injected into the chamber during the operating cycle, the neon ice formed will start to melt and boil off. As pressure rapidly increases, the two combination pump stations are turned off before the pressure exceeds the turbo-molecular pumps' operating limit. The roughing pump is turned on and connected to pump out the neon. The neon accumulated during an operating cycle can bring the pressure up to a few Torr for about a minute and is eliminated in a few minutes by the roughing pump and the high-speed turbo pump (Agilent TV 551). When the pressure gets below 1 mTorr, the roughing pump

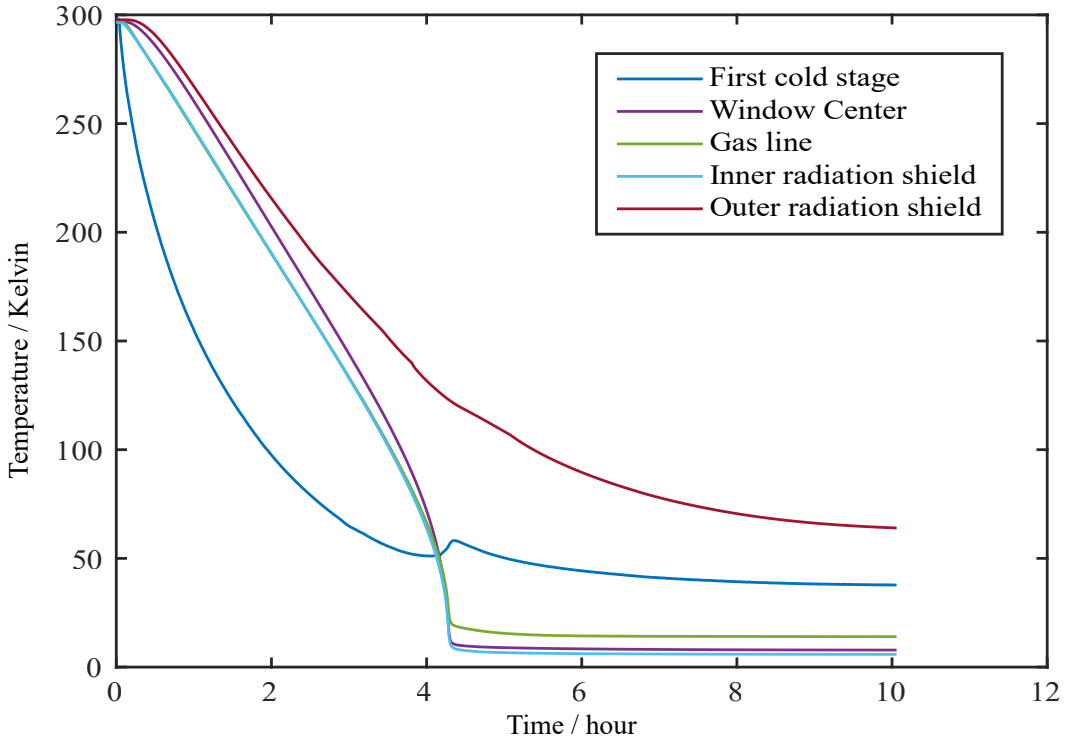

Figure 3.5: Temperature logs during the cool-down process. The inner radiation shield reaches the base temperature within 5 hours, and the out shield gradually stabilizes in 10 hours.

is disconnected, and the pumping stations are turned back on. Then it takes 20 hours for the apparatus to get above the dew point and be ready to vent. The high vacuum during the warm-up process prevents water from condensing on the inner surface, which is time-consuming to remove.

3.2 Ion Trap

The ion trap is the center and one of the most critical parts of our experimental setup. As shown in figure 3.3, it is fixed to the inner radiation shield and located right on the central axis of our main chamber. In the experiments discussed in this thesis, the molecular ion studied is transferred to the ion trap and co-trapped with a $^{88}Sr^{+}$ ion

after being produced in the Extrel chamber. The experiment is then performed in the ion trap. This section will discuss our ion trap's design, properties, pros, and cons.

3.2.1 Trap Design

We adopt a linear Paul trap configuration which has a well-defined axial axis. As shown in figure 3.6 a), the trap is built in between two printed circuit boards (PCB) about 17 mm apart. The two PCBs are fixed relative to each other, bolted to a pair of parallel brass stand-offs. The linear Paul trap consists of four brass bars providing the quadrupole RF field, two end caps providing the axial confinement, and an additional brass compensation rod. The brass rods are soldered and fixed to the two PCBs. And the two end caps are provided by the copper ring electrodes fabricated on the PCBs. Thus a rigid linear Paul trap is obtained.

The brass rod closest to the compensation rod and the one on its diagonal opposite are used as the RF electrodes and are connected to each other near the trap. The other pair of rods are employed as low-frequency electrodes. They have separated electric connections and can be controlled independently. Slow-varying low voltages compared to the RF can be applied to those rods and be used to control the radial motion of the ions. We typically use one of them and ground the other one. The working low-frequency rod and the compensation rod provide full two-dimensional controls of the ions' radial motion and the radial compensation for stray electric fields.

Electric signals are sent into the main chamber through vacuum-compatible BNC feedthroughs. They are connected to PCBs and finally the ion trap via SMA cables and connectors. Between the room-temperature vacuum chamber and the PCBs, two sets of copper SMA feedthroughs are used to thermally anchor the cables to the outer and inner radiation shields. The entire trap is typically cooled to 7 K for an inner shield

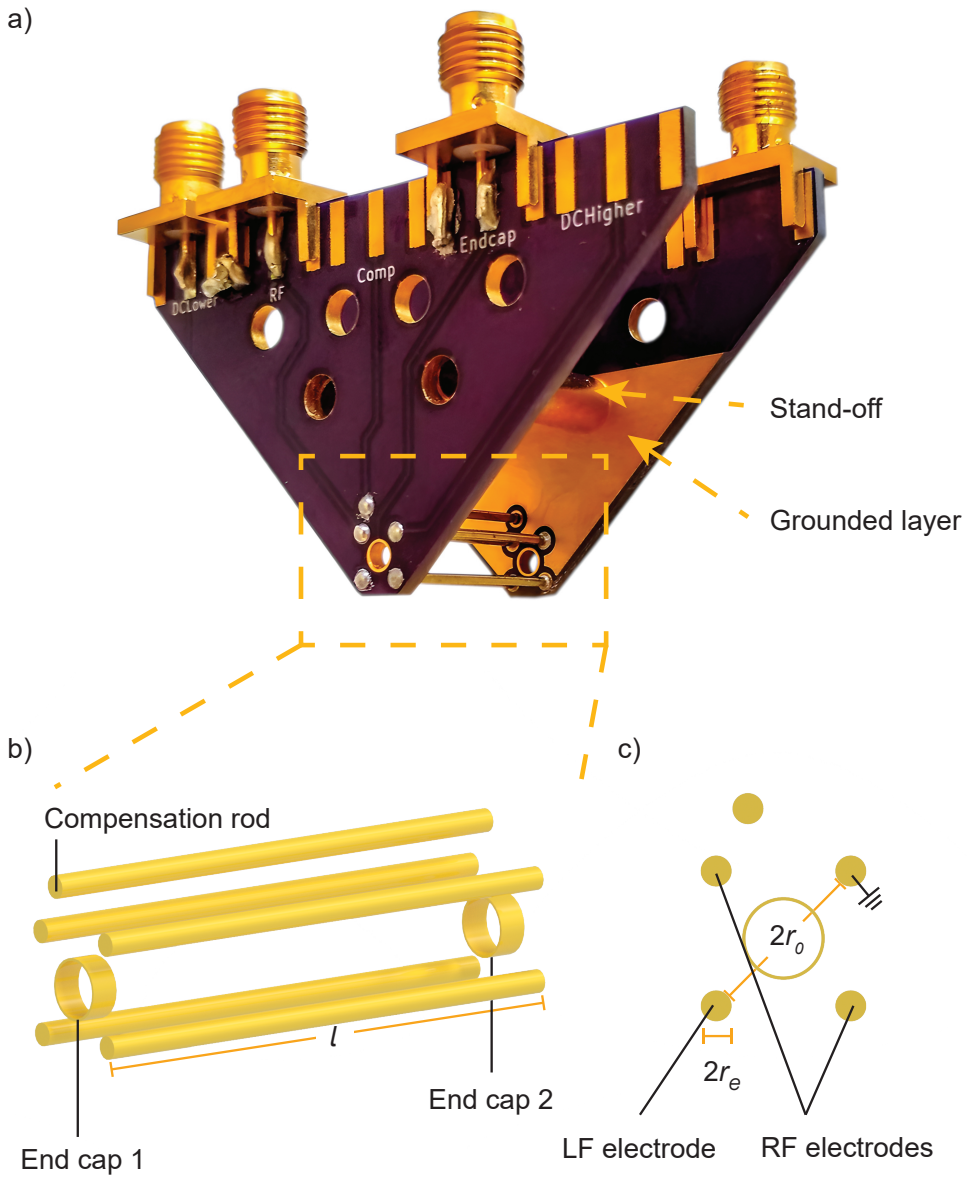

Figure 3.6: a)Linear Paul trap between the printed circuit boards. b) A 3D CAD model of all the effective electrodes. c) The side view of the CAD model

temperature of 5.7 K.

The RF electrodes are driven by an arbitrary waveform generator (RIGOL DG4102) at $\Omega_{rf} = 2\pi \times 1.63$ MHz, signal-amplified by a toroidal resonator. The loaded Q-factor of the resonator is about 12, and the gain is about 6. The other electrodes' DC and low-

frequency AC components are controlled by DC power supplies and arbitrary waveform generators, respectively. Near the trap's center, the RF electric field is dominated by the quadrupole term, and the motion of the ions follows the prediction of the classical ion trap theory and the Matthieu equation. When the ion trap works with our typical voltage settings, we observe an axial secular frequency of 28 kHz and a radial secular frequency of 195 kHz for $^{88}Sr^{+}$, corresponding to a Mathieu q parameter of about 0.34. These parameters are optimized for robustly trapping ions in an extensive mass range near the atomic mass of strontium. The detailed trap parameters are listed in table 3.1.

Parameter	Expression	Value	Unit
Electrode rod radius	r_e	0.42	mm
Electrode rod length	l_e	18	mm
Inscribed radius	r_0	4.1	mm
End cap inner radius	r_{ec}	1	mm
End cap voltage	U_{ec}	40	V
RF amplitude	V_{rf}	90	V
RF angular frequency	Ω_{rf}	$2\pi \times 1630$	kHz
Radial secular frequency of $^{88}Sr^{+}$	$\omega_{r,88}$	$2\pi \times 195$	kHz
Axial secular frequency of $^{88}Sr^{+}$	$\omega_{z,88}$	$2\pi \times 28$	kHz
Mathieu q parameter for $^{88}Sr^{+}$	q_{88}	0.34	–
The mass of ions	m	40 - 300	Da

Table 3.1: Ion trap parameters

The trap assembly is held by a pair of Γ-shaped OFHC copper stands, which are bolted to the bottom panel of the inner radiation shield. The trap axis that goes through the two centers of the two end caps is aligned with the central axis of the ion guide and the quadrupole mass filter in the Extral system. As shown in figure 3.7, this axis is the central axis of the whole experimental setup. It passes through a series of windows and holes as well as the brass door shutter on the inner radiation shield, allowing both the primary laser beam and the ions to be transferred along it. A series of windows are located right under the ion trap. And a NA ~ 0.28 objective lens stack collects the light scattered by the ions through those windows, for the primary imaging system. The other

windows on the side provide excellent optical access to the ion trap from six different directions for multi-proposes.

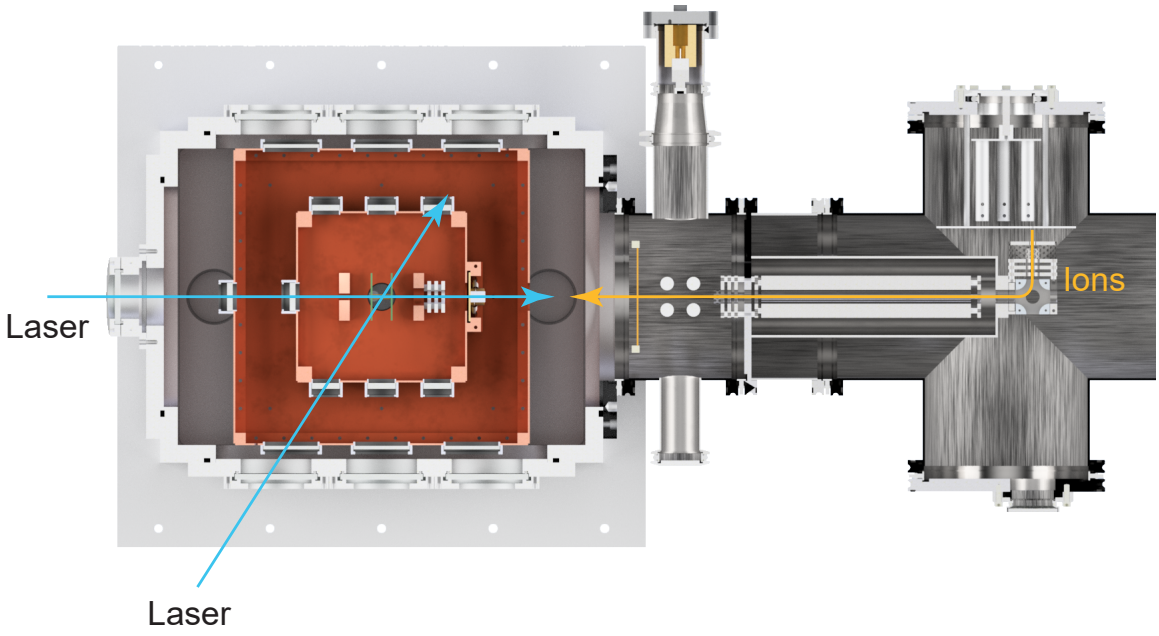

Figure 3.7: A cross-section view of the main chamber and the Extrel chamber. The two laser beams cross the center of the ion trap. The ion beam path is co-aligned with the axial laser beam.

The ion trap is in a relatively isolated electric environment. The inner radiation shield and the Γ-shaped stands are all grounded and are at least 15 mm from the trap's center. The inner surfaces of the two PCBs facing toward the trap are also covered with a grounded copper layer to screen the external electric field and minimize the insulating area exposed to the trap. This design significantly reduces the impact of stray electric fields and enables robust and controlled ion trapping.

3.2.2 Ion Dynamics: near the trap center

The following subsections introduce several simplified models to characterize the ions' motions inside the trap. These include motions near the trap's center, large-scale radial

motions, and the slow-down process during ion loading.

The electric field near the center of our linear Paul trap is well-described by the quadrupole terms, ignoring the stray field and its compensation field. Similar to quadrupole mass filters, the particles with charge Q and mass m can be trapped if their Matthieu parameters are in the stable region. In our cases, where the radial Matthieu parameter a is about 0, the radial Matthieu parameter q should be smaller than 0.9. Practically, we have observed trapped single-charged ions in a mass range between 40 and 300 Dalton (Da). In our experiments, we focus on those ions that can be well-crystallized with the $^{88}Sr^{+}$ ions, the masses of which are typically between 55 and 160 Da. Recall the Matthieu parameters in a quadrupole field described with equation 2.1 follow,

$$a_r = \frac{4QU\alpha}{m\Omega_{rf}^2}, \quad q_r = \frac{2QV\alpha'}{m\Omega_{rf}^2} \tag{3.1}$$

$$a_z = \frac{4QU\gamma}{m\Omega_{rf}^2}, \quad q_z = \frac{2QV\gamma'}{m\Omega_{rf}^2} \tag{3.2}$$

Assuming a perfect C_4 symmetry and a translational symmetry of the RF field along the trap axis, we have $-2\alpha = \gamma > 0$, $\gamma' = 0$.

For single-charged ions in the mass range from 55 Da to 160 Da, the Matthieu parameters satisfy the condition $(|a|, q^2) \ll 1$. In this case, we can adopt the lowest-order approximation and get the secular frequency and the motion of a single ion:

$$\omega_r \approx \sqrt{a_r + q_r^2/2}\frac{\Omega_{rf}}{2}, \quad r(t) \approx A\cos(\omega_r t + \phi)[1 - \frac{q_r}{2}\cos(\Omega_{rf} t)] \tag{3.3}$$

$$\omega_z \approx \sqrt{a_z}\frac{\Omega_{rf}}{2}, \quad z(t) \approx A'\cos(\omega_z t + \phi') \tag{3.4}$$

This result is identical to the solution obtained from the pseudopotential approximation. [6, 29, 30] The radial motion of the ion is a combination of the secular motion

at the radial secular frequency ω_r and the micromotion at the RF frequency Ω_{rf}. And the solution of axial motion is a simple harmonic oscillator. Ignoring the high frequency and small amplitude micromotion, the ion is effectively doing the secular motion in a three-dimensional harmonic potential described by the secular frequencies,

$$U_{pseudo} = \frac{1}{2}m\omega_r^2 r^2 + \frac{1}{2}m\omega_z^2 z^2 \tag{3.5}$$

With the same RF and end cap voltages, the terms αU, γU, and $\alpha' V$ are constants for all the ions, which can be determined from the axial and radial secular of $^{88}Sr^{+}$. Therefore, the Matthieu parameters and the secular frequencies of different ion species can be calculated. In the experiments, we always run out trap under the limit,

$$\omega_z \ll \omega_r \ll \Omega_{rf}, \tag{3.6}$$

, which indicates the ions are tightly confined radially and are loosely bound axially.

3.2.3 Ion Dynamics: large scale radial motion

In the previous subsection, we introduced the pseudopotential near the trap center. Though the ions in our trap are tightly confined radially, we sometimes coherently drive them to high orbits. To better characterize this process, I build a model to analytically describe the RF field and pseudopotential on the radial plane in the whole trapping region using the method of images.

If hyperbolically-shaped electrodes are used, equations 2.1 and 3.5 will be valid in the whole trapping region. If rod-shaped electrodes are used, high-order terms will appear in those equations. Those terms, corresponding to the anharmonicity of the pseudopotential, will become significant as the ion's distance to the trap center r becomes larger.

It has been predicted that the leading-order term contribution to anharmonicity can be minimized when the optimal ratio between the rod electrodes' radius and the inscribed radius $\frac{r_e}{r_0} = 1.14511$ is achieved.[31] Nevertheless, our electrodes' radius is considerably smaller than the predicted optimal value to optimize the optical access and minimize the effect of the stray field. Hence, it is necessary to consider those terms to characterize the ion's motion in our trap.

To obtain the pseudopotential, an approximate analytical solution of the RF electric field is found with the method of images. At the radio frequency $\Omega_{rf} = 2\pi \times 1.63$ MHz, we have $\lambda_{rf} \gg r_0, l$, satisfying the quasistatic condition. Thus we can use the electric potential at $t = 0$ to characterize the RF field. The electric potential inside the charge-free trapping region should follow Laplace's equation, a special case of Poisson's equation. Based on the uniqueness theorem for Poisson's equation, the solution of the equation is unique with a given boundary condition.[32] Thus, if a solution matching the boundary condition is found, it will be the right solution. Such a solution is obtained by considering an image system of four line charges.

The electric field of systems consisting of one or two infinitely long conductive rods can be solved precisely with the method of images. However, such a simple solution does not exist in the four-rod cases. Instead of finding an exact solution, an approximation solution is obtained by considering an imagined system consisting of four line charges, where the equipotential surfaces match the inner surfaces of the rods. The optimal positions of the line charges are $r_{image} = 2.5$ mm away from the trap center on the electrode directions. The form of the RF potential is found to be,

$$V_{rf}(x, y) = -A \cdot \ln\left(\frac{r_1 \cdot r_3}{r_2 \cdot r_4}\right) \tag{3.7}$$

where r_i $(i = 1 \sim 4)$ is the distance between the point and the four line charges. The

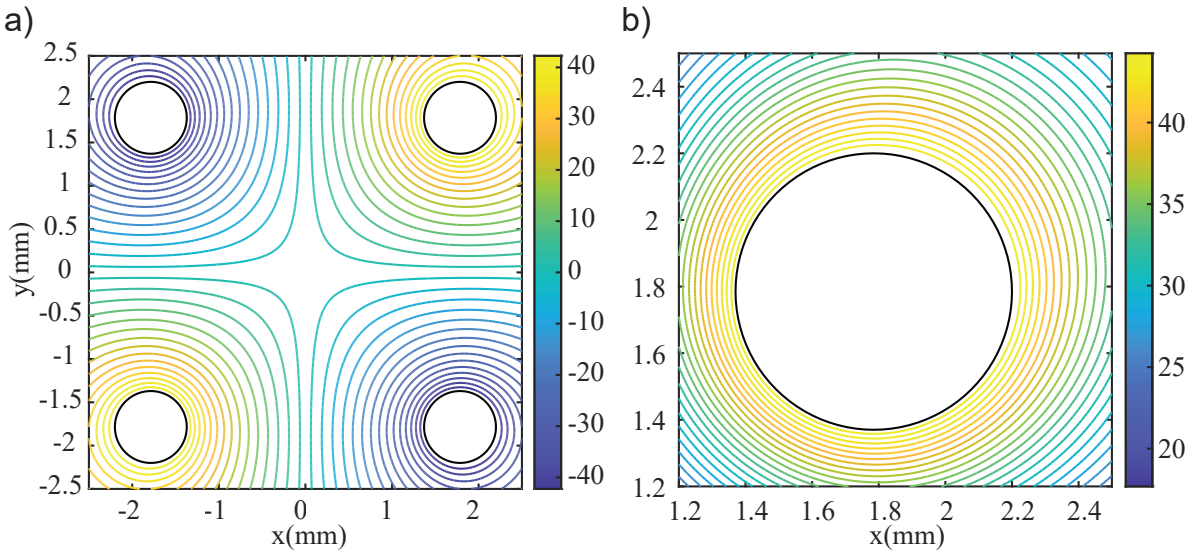

Figure 3.8: The equipotential maps of the simulated RF electric potential (in V). a) The whole trapping region. The black cycles refer to the electrodes. b) A close view near the top right electrode. The inner side of the electrode is perfectly matched, while the outer side is missed by about 0.02 mm.

equipotential surface almost perfectly matches the electrodes' boundary, as shown in figure 3.8. It indicates the method gives an accurate prediction of the RF field.

The pseudopotential approximation is adopted. So we have the micromotion in the RF field to be,

$$\vec{E} = (-\vec{\nabla} V_{rf}) \cos(\Omega_{rf} t) \tag{3.8}$$

$$\vec{a} = \frac{Q}{m}(-\vec{\nabla} V_{rf}) \cos(\Omega_{rf} t) \tag{3.9}$$

$$\Delta\vec{r} \simeq \frac{Q}{m\Omega_{rf}^2}(\vec{\nabla} V_{rf}) \cos(\Omega_{rf} t) \tag{3.10}$$

The lowest order term of the time-average acceleration is,

$$< \vec{a} > \simeq \frac{\int_0^T \vec{a}(\vec{r} + \Delta\vec{r}, t) \cdot dt}{T} \simeq -\frac{1}{4\Omega_{rf}^2} \vec{\nabla} a^2(t = 0) \tag{3.11}$$

, where $T = \frac{2\pi}{\Omega}$. And therefore, we have the pseudopotential of the trap to be,

$$U_{pseudo} = \frac{1}{4\Omega_{rf}^2} a^2 m = \frac{1}{4\Omega_{rf}^2} \frac{Q^2}{m} |\vec{\nabla} V_{rf}|^2 \tag{3.12}$$

Near the center of the trap, the RF potential can be Taylor expanded,

$$V_{rf}(x,y) = -A \cdot [-\frac{4xy}{r_{image}^2} + \frac{4}{r_{image}^6}(x^5 y - \frac{10}{3}x^3 y^3 + xy^5) + O((\frac{r}{r_{image}})^{10})] \tag{3.13}$$

The first term of 3.13 corresponds to the quadrupole field, and the other terms are higher-order multipoles. Substituting the lowest order term into equation 3.12, we can get the harmonic term of the pseudopotential near the trap center. The coefficient A in equation 3.7 can now be determined based on the secular frequency of $^{88}Sr^+$ near the trap center,

$$A = \frac{\sqrt{2}}{4} \Omega_{rf} \frac{m_{Sr}}{Q_{Sr}} r_{image}^2 \omega_{Sr} \tag{3.14}$$

Based on this result, the RF amplitude on our RF electrodes is determined to be about 90 V. (An additional coefficient of 2 has been counted since we only apply the RF voltage to two electrodes.) And now, we can predict the pseudopotential and the scale of micromotion for any ions. The pseudopotential and the micromotion of $^{88}Sr^+$ are calculated and shown in figure 3.9 and 3.10.

Based on the pseudopotential, ions' secular motion can be numerically simulated. For instance, the period of $^{88}Sr^+$ ion's secular motion along the diagonal direction is calculated and is shown in figure 3.11. The difference of the period is minor than 0.5% if the secular motion amplitude is smaller than 0.5 mm. And the period starts to decrease as the amplitude of the secular motion gets larger. Such a feature makes it possible to keep mass-selectively exciting an ion into a high-energy orbit without driving them out of the trap.

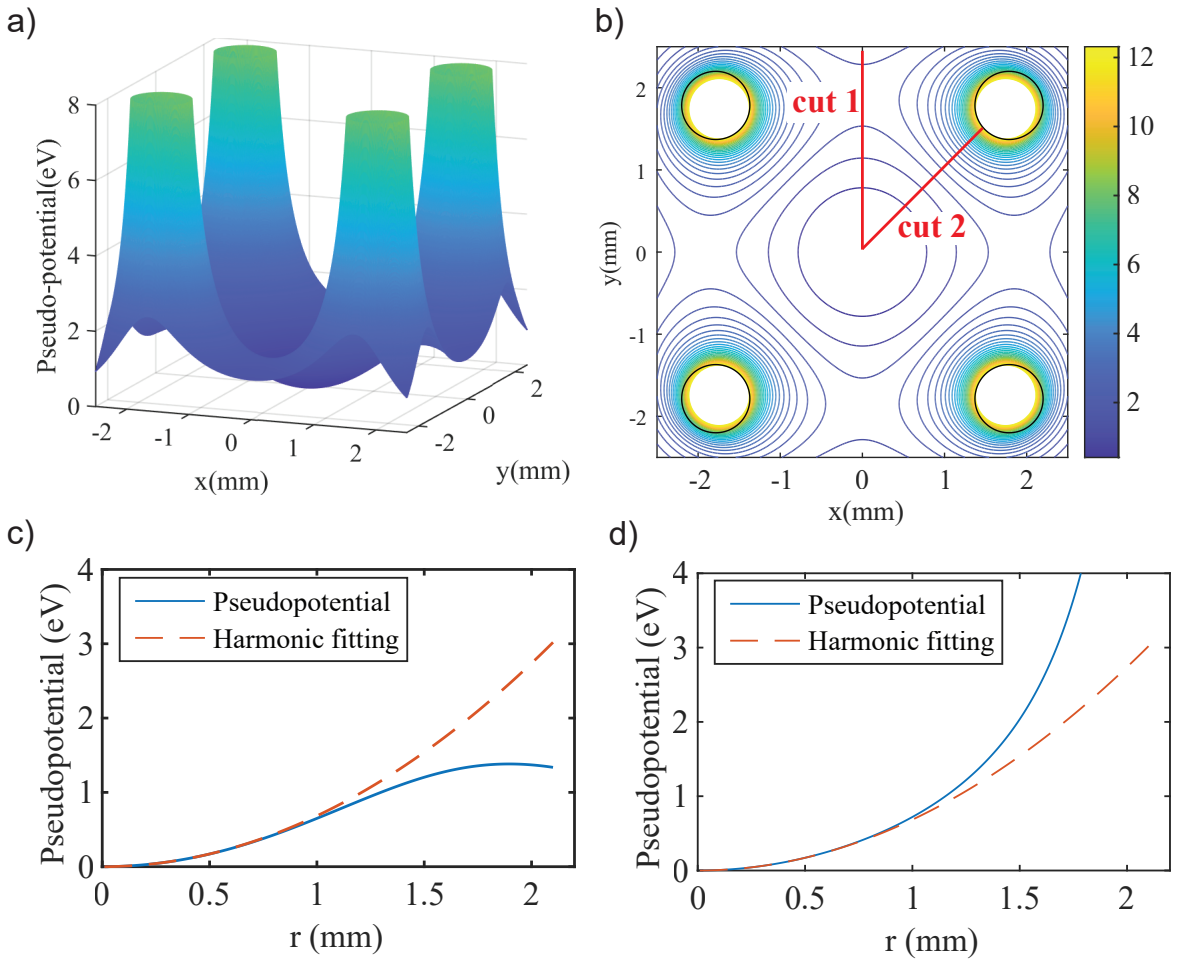

Figure 3.9: The pseudopotential of $^{88}Sr^{+}$ around the trapping region. It reaches the minimum at the trap center and spikes near the electrode. It has an approximate cylindrical symmetry and quadratic relationship with r near the center, which is broken by the high-order terms for large r. a) A mesh plot of the pseudopotential. It is cut off at 8 eV. b) A equipotential map of the pseudopotential. The black cycles refer to the electrode boundaries. c) and d) The pseudopotential along cut 1 and cut 2.

Moving diagonally, the maximum distance to the trap center r that $^{88}Sr^{+}$ can reach is about 1.7 mm. The pseudopotential at that point is about 3 eV. If the ion moves closer to a electrode, the micromotion will be large enough to throw it on the electrode. Moving along the x or y axis, the maximum r is about 2 mm, where the pseudopotential reaches a saddle point at about 1.3 eV. In general, any orbits having high energy will not

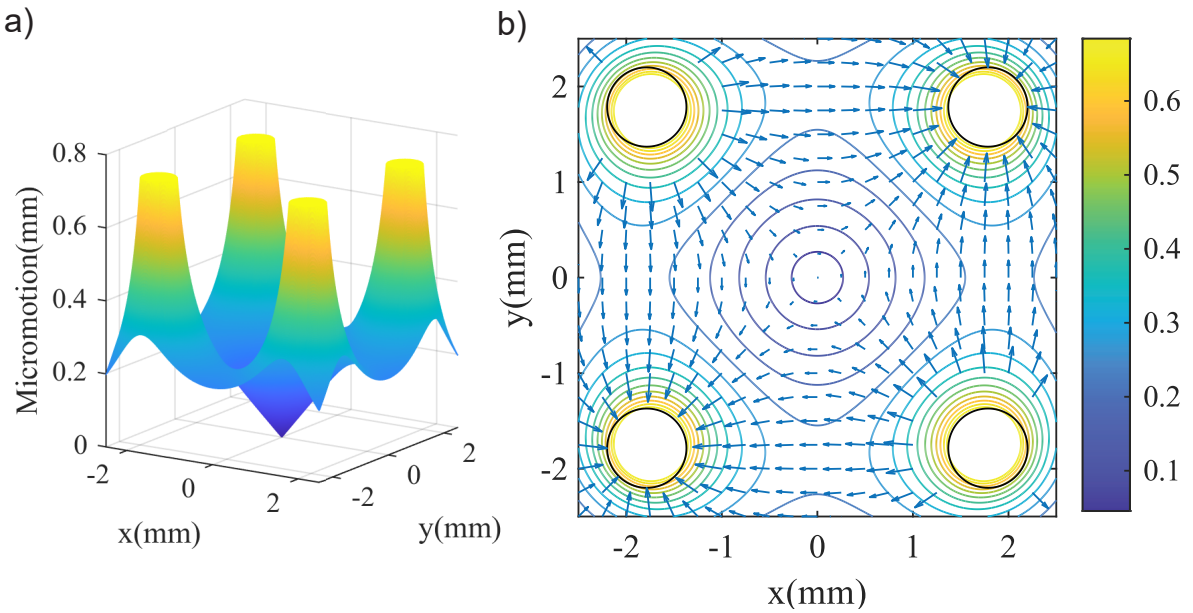

Figure 3.10: a) A mesh plot of the micromotion amplitude of $^{88}Sr^{+}$. The amplitude of micromotion is proportional to r near the trap center. b) A equipotential map of the micromotion amplitude. The arrows indicate the directions of micromotion.

be stable.

3.2.4 Ion Dynamics: axial motion

The axial confinement of ions is mainly provided by a static field. The static field is induced by the positive voltages U_{ec} applied to the end caps. It is partially shielded by rod-shaped electrodes and yields a harmonic potential along the trap axis near the center. The anharmonicity becomes significant near the end caps. The highest electric potential on the trap axis is about the end cap voltage and is located at the two centers of the two end caps. During the experiments, we typically apply 40 V on both end caps, which results in an axial secular frequency of 28 kHz for $^{88}Sr^{+}$.

The end cup voltages are reduced to under 15 V during ion loading. The ions generated in the Extrel chamber are shuttled into the ion trap through the end cap. The ions need an initial energy higher than the end cap voltage to pass the electric barrier. And to

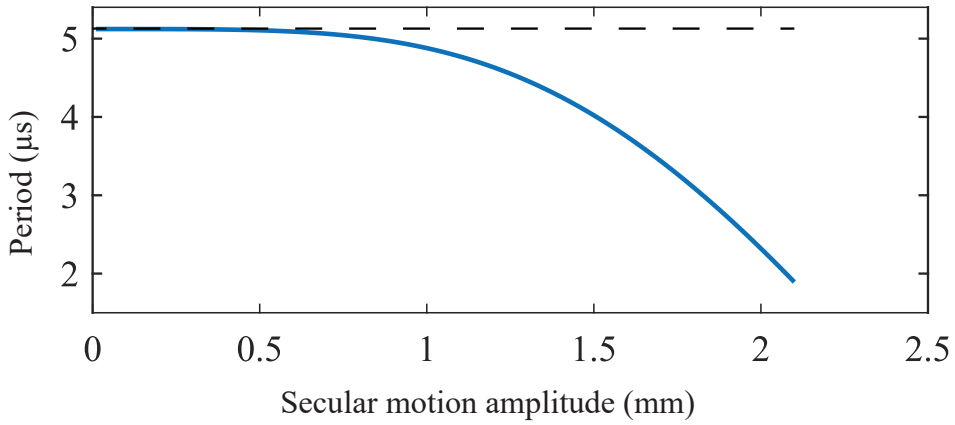

Figure 3.11: $^{88}Sr^{+}$ secular motion's period vs. amplitude. The dashed line shows $\frac{2\pi}{\omega_{r,88}}$, which is the upper limit of the period near the trap center.

stay in the trapping region, the energy more elevated than the end cap voltage needs to be dissipated before the ion leaves the trap through an end cap again. The dissipation is usually realized by collisions with buffer gas. We typically generate the ions with initial energy between 8 eV and 18 eV and set the end cap voltage 3 V lower than it. Such an energy scale is chosen to optimize the behavior of the quadrupole mass filter (QMS) in the ion generation system and lower the energy of collisions when loading molecular ions. The collisions more energetic than 20 eV can easily cause complicated collision-induced fragmentation[33, 34] and isomerization[35], which we want to avoid.

3.2.5 Discussion

Among a variety of types of ion traps, the linear Paul trap has an outstanding performance in molecular ion and sympathetic cooling related experiments, including high-precision quantum logic spectroscopy[24, 11, 12, 25], cold chemistry[36, 37, 38, 39], and quantum information experiments[40]. The large field-free trapping volume around the naturally-defined trap axis suits the requirement of high-precision experiments and large coulomb crystals.[41] In our experiment, we leverage this property to form a micromotion-

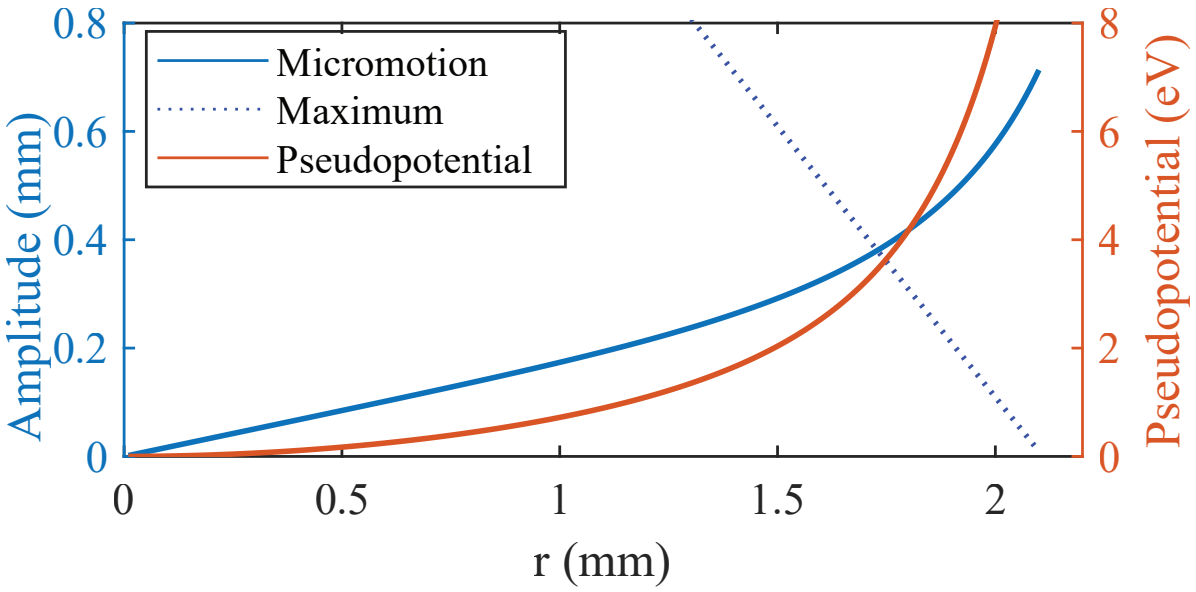

Figure 3.12: Micromotion amplitude and the pseudopotential along the diagonals. The doted line shows the distance to the electrode surface. It indicates the maximum micromotion amplitude that is physically allowed.

free two-ion coulomb crystal along the trap axis and drive it axially in the RF-free region.

Our trap geometry is optimized for robust tickle scans and action spectroscopy. The features like small $\frac{r_e}{r_0}$ ratio and large axial length l play a role in achieving optimal performance.

The tickle scan technique, used to precisely determine the secular motion frequencies and the mass of the ions, requires good optical access and a disturbance-free environment. Tickle scan read out the secular motion frequency based on the photon scattering rate's modulation of $^{88}Sr^{+}$. The considerable trap length guarantees a harmonic axial potential in a large volume for the experiment. The small $\frac{r_e}{r_0}$ ratio of about 0.2 provides good optical access to the ions at the trap center, which enables the efficient collection of scattered photons in a large solid angle. The large gap between the electrodes also helps to cut down the scattering background of the incident laser at the electrodes' surface. These two advantages greatly enhance our detection efficiency.

The stray electric field is one of the major sources of systematic error in the tickle scan based mass spectrometry. The uncontrolled electric field fluctuation could significantly impact the axial motion due to the loose axial confinement and is hard to distinguish from changes in ions' mass. The stray field could be induced by the photoelectric effect, ions accumulation, and spontelectric effect[42, 43, 44]. All of them cause an electric field on a solid surface, which in our case is mainly the four long rod-shaped electrodes.

Several designs are adopted to reduce those effects. First, the small $\frac{r_e}{r_0}$ ratio minimizes the exposed surface area and the solid angle of the electrodes to the trap center, greatly relieving the impact of the three types of stray field. Secondly, the end cap's inner diameter and the gap between the electrodes are designed to be sufficiently large compared with the laser beam width to reduce the photoelectric effect. Thirdly, the insulator surface is minimized near the trap center. The charges accumulated on those surfaces can hardly be dissipated. Unfortunately, ice forming on the electrodes is inevitable to perform buffer gas cooling and action spectroscopy, as shown in figure 3.4. However, we managed to minimize the use of dipolar gases near the trap and the amount of ions that can reach the icy surface to reduce the charge accumulation rate. We also occasionally perform a warm-up procedure to reset the accumulated ice and charges and clean the stray field. Based on our experience in these years, a warm-up cycle to 80 K can remove most of the ice layer, but the accumulated charge may still survive. The best practice we found to remove the charge is to warm up the whole system to room temperature and fill the chamber with air for a few minutes.

Moreover, the ions are sent into the trap axially through the end cap but not radially. If the ions are loaded radially and accumulated on the electrode rods, it could cause an irregular electric field that affects the ions both radially and axially. Such a field not only displaces the ions from the trap center but also makes the electric potential inharmonic, which is impossible to compensate for. Figure 3.13 is an example where such a stray field

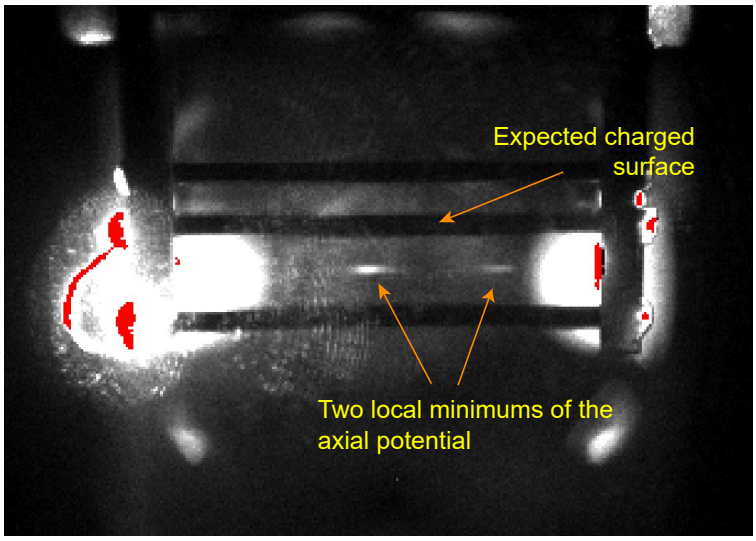

Figure 3.13: An extreme case where the axial confinement is strongly disturbed by charges accumulated on the rods when the ions are loaded radially from an ion source. The two local minimums of potential are observed, and the axial secular frequency becomes position dependent.

causes a failure of the experiment.

When loaded axially through the end cap, ions can only attach to the outer surface of the PCB. The field induced by those charges is shielded by the end cap electrode and the grounded layer on PCB's inner surface, barely affecting our experiments. It sometimes causes a displacement within 50 μm when the end cap voltages are below 15 V. Such an effect can be ignored or easily compensated with a slight bias of the end cap voltages. Although high ions flux passing through the small aperture of the end cap could cause a significant space charge effect, limiting our loading efficiency and causing rapid expansion after the hole [45, 46], we still find loading through the end cap is the best choice.

We have tested several other linear Paul trap designs and observed diverse failures. Most of the failures relate to the charges accumulation on the insulator or icy surfaces near the trap center. Several photos of those traps are shown in figure 3.14.

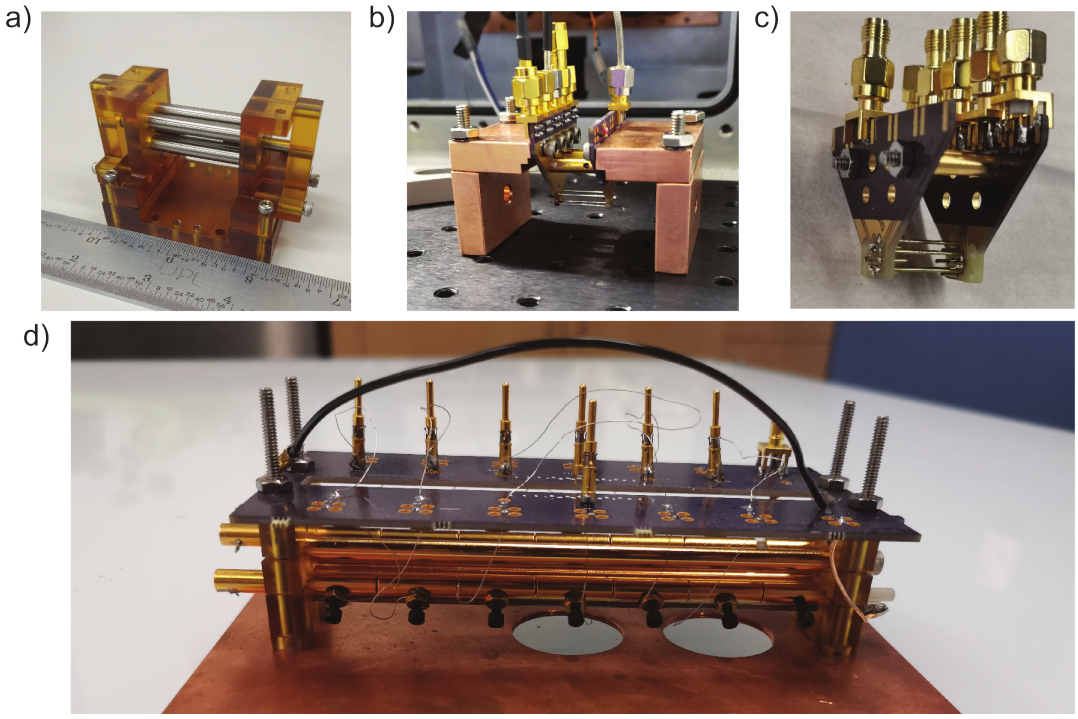

Figure 3.14: a) Our first ion trap that I fabricated in the student machine shop. It has a large $\frac{r_e}{r_0}$ ratio. b, c) Ion traps with different end caps and PCB designs. d) A segment trap. Charge accumulates on the insulator surface, which is exposed by the tiny gaps between the segments.

3.3 Ion Generation System and Extrel Chamber

In this section, I will introduce our ion generation system located in the Extrel chamber. The system is built based on a commercial quadrupole mass filter, Extrel CMS. It is capable of atomic and molecular ions production, mass selection, ion transfer, and output detection.

3.3.1 Chamber Design

The Extrel chamber is attached to a side panel of the main chamber via an ISO-160 flange. The chamber's main body consists of a 5-way ISO-160 style cross and several ISO-160 nipples. The quadrupole mass filter (QMF) is fixed along the chamber axis by

an ISO-160 double-sided blank flange, as seen in figure 3.15 a). The flange separates the Extrel chamber from the main chamber, only leaving a small hole around the QMF. A dedicated combination pumping station (Pfeiffer HiCube Eco 80) is connected to the Extrel chamber to keep it at a good vacuum. When the cryo system is on, the pressure in the Extrel chamber can reach 3×10^{-7} Torr, read from an ion gauge (InstruTech IGM401) connected to the Extrel chamber.

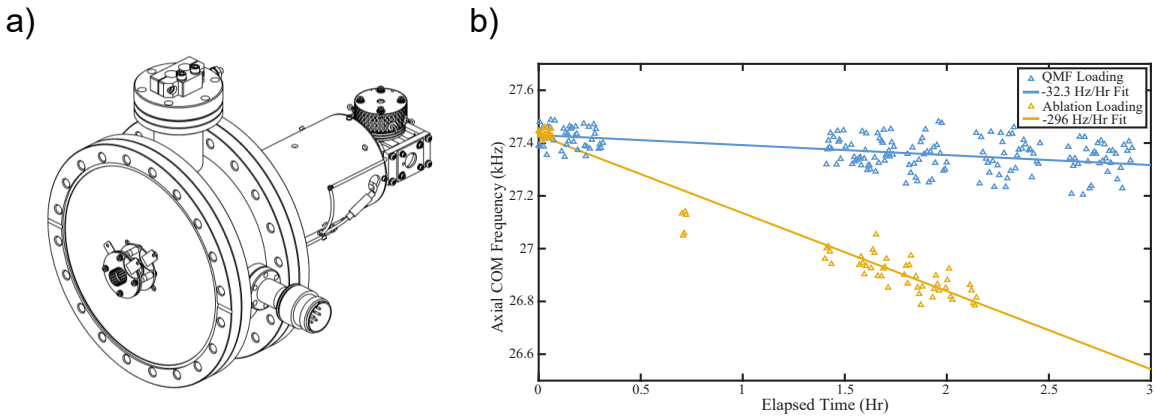

Figure 3.15: a) A CAD drawing of the Extrel CMS quadrupole mass filter. b)$^{88}Sr^{+}$ axial secular frequency drift over time for filtered and unfiltered ion loading. Mass–filtered loading has reduced this drift by an order of magnitude compared to ablation-photoionization.

The relatively separated design of the ion generation system is adopted to minimize the disturbance to the electric circumstance of the experimental volume during the ion generation process. The neutral molecules used to generate molecular ions are retained in the Extrel chamber, limiting the spontelectric effect mentioned in the ion trap section near the ion trap. The QMF and the separation also limit the amount of ions reaching the trap region. The impact of the ion loading process with this system has been compared with a photoionization method of strontium loading by monitoring the drift of the $^{88}Sr^{+}$ axial secular frequency. In the photoionization scheme, a low-power 532 nm laser ablation on a strontium aluminum alloy surface heats the alloy and produces neutral strontium

atoms. Following the ablation, the strontium atoms are driven to an autoionizing state by 461 nm and 405 nm laser, undergoing a two-step doubly-resonant process, and then ionize to $^{88}Sr^{+}$ ions. The photoionization scheme was reported to be a clean, efficient, and controlled loading method in room temperature setups. [47] On the other side, with the Extrel QMF, the $^{88}Sr^{+}$ ions are directly produced by high-power 532 nm laser ablation, which generates neutral plasma containing both neutral and ionized strontium. The results are shown in figure 3.15 b). Loading with our QMF cuts down charging-induced secular frequency drift by an order of magnitude, showing the superior advantage of our ion generation system for cryogenic ion trap setups. Notably, QMF can filter both a short ion pulse and a steady ion flow, while the other options, like time of flight mass filter, only work for the ion pulse.

The layout of the Extrel chamber is shown in figure 3.16. The ions are initially produced on the right-hand side via electron impact ionization or ablation. A standard off-axis electron impact (EI) ionizer is integrated with the quadrupole mass filter. The neutral molecules are ionized during collisions with electrons, which are emitted by a hot filament and accelerated by a local electric field. This process produces molecular ions, the initial energy of which is controlled by the ionizer's bias. The ions are then extracted out from the ionizer by a negatively biased electrode closer to the axis and sent in the quadrupole bender.

Laser ablation is commonly used to generate ions from solid samples.[48] We use a 532 nm Nd:YAG pulsed laser (Minilite II from Continuum) as our ablation laser. The laser is focused onto the solid samples held in a rotating holder(see a in figure 3.16) with a $f = 400$ mm lens, going through the viewport and apertures in the center of the quadrupole bender and the ionizer. The ablation method is mainly used to produce $^{88}Sr^{+}$ ions in our experiment. Focused on a strontium-aluminum (10%/90%) alloy sample, a laser pulse of about 1 mJ can produce more than a hundred thousand $^{88}Sr^{+}$ ions. The

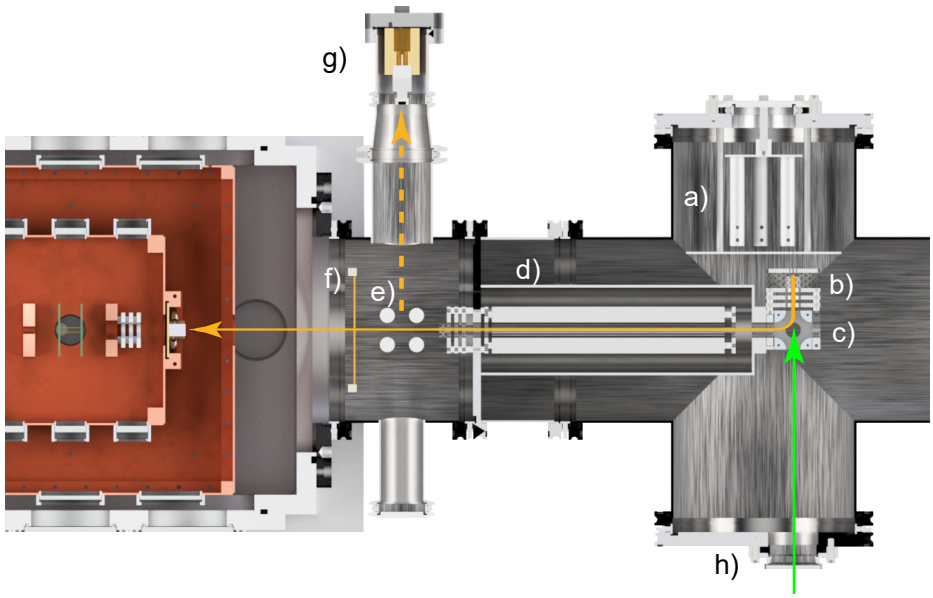

Figure 3.16: A cross-section view from the top. The green arrow shows the beam path of the 532 nm pulse laser, and the orange ones show the ion trajectories. a) Rotating holder for solid samples. It is covered by an aluminum sheet with a port for laser ablation and ion ejection. b) Off-axis EI ionizer. c) Quadrupole bender (or quadrupole deflector). d)Quadrupole mass filter with a shield. e) Four electrodes for horizontal steering. They also can serve as the second quadrupole bender, which deflects the ions to a channel electron multiplier along the orange dashed line. f) Horizontal electrodes for up-down steering. g) Channel electron multiplier for ion detection. h) Viewport for ablation laser.

ions with suitable velocities would go through the ionizer and follow the same trajectory of molecular ions to the QMF.

The quadrupole bender produces a static electric field, deflecting the generated ions to the QMF (see c in figure 3.16). It prevents most of the thermal radiation and neutral plasma produced with the ion generation process from reaching the trap region together with the ions. The bender also acts as an energy filter. Our initial tests with a QMF in a residual gas analyzer (SRS RGA 300) show that the ablation-produced ions could be fast enough to pass the QMF at a wrong mass setting. As a result, the mass resolution of the QMF is significantly broadened to a few Dalton. Further experiments with a time-of-flight (TOF) setup show laser ablation can produce ions with initial energy from 0 to

more than 30 eV. Initial kinetic energies of more than 100 eV are also observed when the ablation laser's pulse energy is higher than 10 mJ. Those fast ions can hardly be mass-selected with QMF. To solve the problem, we made an electrostatic energy analyzer (ESA) with a quarter-cylindrical design and found it capable of selecting ions, the energy of which is within 20% of the predicted target energy [49]. The quadrupole bender plays a similar role to the ESA over here.

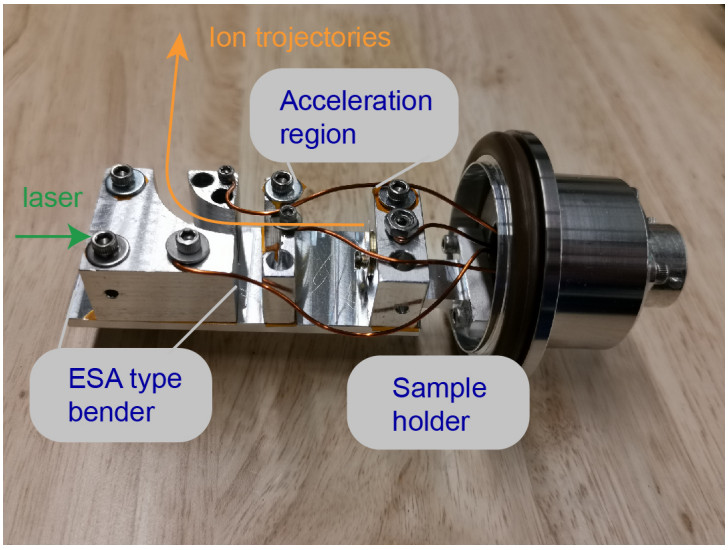

Figure 3.17: The homemade ESA-type bender for the TOF experiments. It is integrated with the sample holder and acceleration plate.

Passing the bender, ions are selected based on the mass-to-charge ratio in the Extrel quadrupole mass filter. The QMF is shielded by a conductive cylinder, which screens the external field. The QMS is typically biased several volts below the ionizer voltage, so that the ions are slowed down to perform the high-resolution (within 0.2 Dalton) mass selection. The ions with the correct mass are stably confined along the axis and transferred toward the ion trap. And at the end of the QMF, a set of Einzel lenses helps to focus the out-coming ion beam.

The mass-selected ions can be shuttled in the ion trap or deflected to a channel electron multiplier(CEM) to verify the ion production by changing the voltages applied

to the second quadrupole bender. When the ion beam is deflected toward the CEM, we can detect the ion flux and use the system as a standard quadrupole mass spectrometer. To load the ions, the second bender is used as steering optics together with a pair of horizontal electrodes, focusing the ions to the ion trap.

3.3.2 Molecular Sample Lines

To generate a certain molecular ion species, the parent molecule gas is prepared in an external gas line manifold and sent into the Extrel chamber via an all-metal leak valve above the ionizer. Our current gas manifold design can work with liquid and solid samples with a vapor pressure higher than 50 mTorr. Via the leak valve, the vapor of the samples can be controllably leaked into the Extrel chamber. We usually adjust the leak valve so that the pressure in the Extrel chamber is stabilized between 6×10^{-7} and 1.5×10^{-6} Torr. At that pressure, about 10^5 ions can typically be detected at the primary peak of the sample's EI mass spectrum in a second.

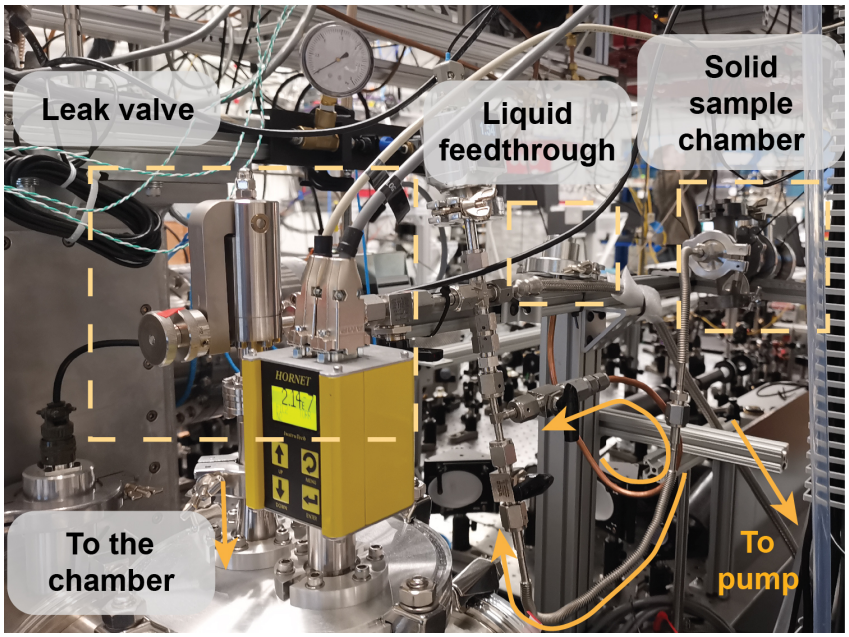

Figure 3.18: Molecular Sample Lines

When a liquid sample is used, the gas line is firstly pumped to about 5 mTorr with a dry scroll pump (Agilent IDP-07, 2.5 l/s). The pump is disconnected, and the liquid sample is injected into the gas line through a rubber feedthrough with a syringe. As the sample vaporizes in the gas line, the pressure in the gas line will be stabilized around the vapor pressure, and the vapor will be ready for leak-in.

If a solid sample is used, it will be placed into a four way cross connected to the manifold before pumping.

3.3.3 Mass Spectra

As mentioned in the previous subsection, our ion generation system can be used as a standard quadrupole mass spectrometer and also a residual gas analyzer with the CEM. The mass spectra of the background and new molecule samples are usually taken before the experiment. Aiming at a specific kind of molecular ion, we always ensure the number of ions produced from the sample is much higher than that from the background.

A typical mass spectrum of the residual background in our chamber is shown in figure. The highest peak corresponds to water, indicating that water vapor contributes significantly to the pressure in the Extrel chamber. The full width at half maximum of each peak is about 0.25 Dalton, and an absolute zero background can be achieved 0.3 Dalton away from the peak centers. It indicates our ion generation system can accurately distinguish ions with different integer masses.

3.4 Buffer Gas

The cryogenic buffer gas plays an important role in our ion cooling and action spectroscopy experiments. The buffer gas technique has been demonstrated as a powerful tool to cool the atoms, molecules, and ions to cryogenic temperature.[50, 51, 52, 53] It is

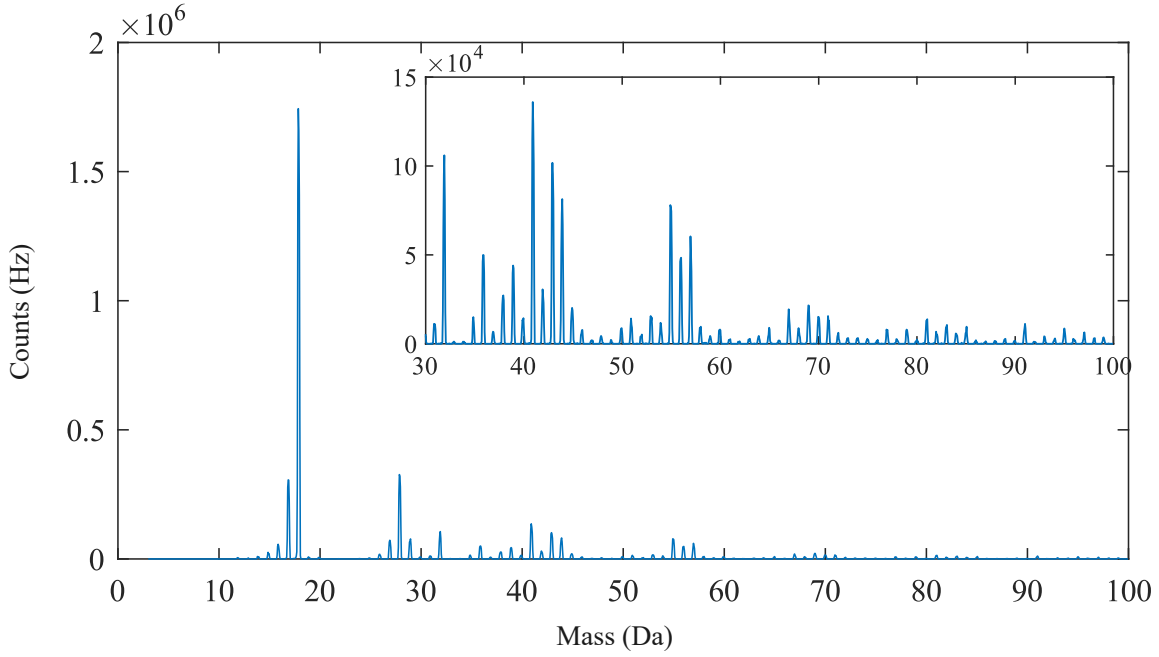

Figure 3.19: A typical mass spectrum of the background

used as a general method to cool all the translational, rotational, and vibrational degrees of freedom of the particles. In our experiment, neon buffer gas is used to perform the initial cooling of all the ions' translational motion, as well as the molecular ions' rotational and vibrational cooling. Another helium-nitrogen mixture gas is used to further cool the molecules below the neon temperature (about 14 K) and form the ion-messenger complex (tagged ion) for our cryogenic ion vibrational predissociation (CIVP) experiment.

The major challenge of designing our buffer gas system is to avoid impurity-induced reactions while keeping a high buffer gas flux for efficient cooling and tagging. The primary ion-losing mechanism in our experiment is ions' irreversible reaction with reactive gas molecules like oxygen leaked into the trap, the existence of which is confirmed by the observed formations of strontium oxide ions. The cryo-pumping effect efficiently exhausts those reactive molecules in the main chamber at the radiation shields. However, they can go directly to the ions through the buffer gas line. Hence, minimizing the production

of impurities is the top concern in designing buffer gas lines.

We use the compressed gas cylinders ordered from Airgas® as our gas source. The neon is at research grade (99.999% purity, NE R33A250LT). The helium is at chromatographic grade (99.9999% purity, HE CH80). And the nitrogen is at research grade(99.9997% purity, NI R200). The gas cylinders are connected to two-stage high-purity gas regulators(Harris KH1139) and then to the gas line manifold outside the main chamber.

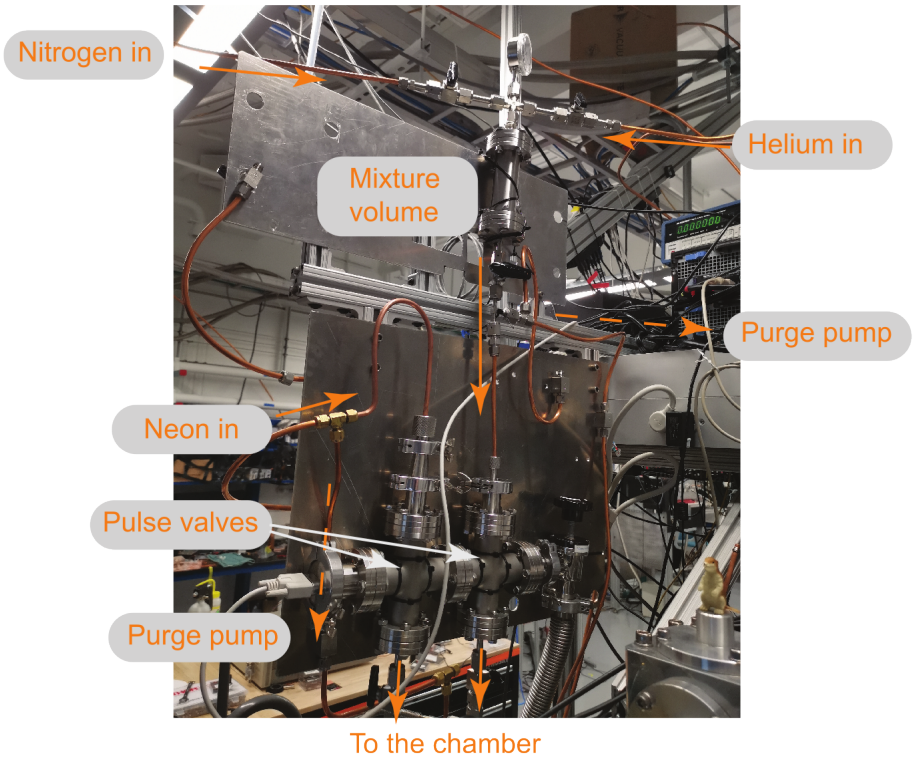

Figure 3.20: Buffer gas manifold. The two pulse valves are protected in a vacuum environment in ConFlat® crosses.

The gas line manifold outside the chamber is shown in figure 3.20. One gas line is used for neon buffer gas, and another line is used to prepare the helium-nitrogen mixture. Two solenoid-actuated pulse valves (Parker-Hannifin 009-1645-900) control the firing of the neon and helium-nitrogen mixture gas pulse independently. The pulse valves are isolated from the atmosphere environment in two constantly-pumped ConFlat® crosses, which

significantly reduces the oxygen contamination through the pulse valve's non-perfect sealing. The pressure in the crosses is kept below 4×10^{-6} Torr.

The gas is sent to the pulse valves via 1/4-inch copper tubes and tube fittings. The copper tube is chosen for its flexibility and low permeability. As a comparison, the commonly used Teflon-PFA tubing and PTFE tubing have oxygen permeability at the level of 10^{-8}[cm^3(stp) mm]/[cm^2 s cm Hg][54, 55], which would theoretically result in an oxygen pressure increase of more than 0.1 Torr/day in the gas line if used. When we were using the PTFE tubing and exposing the pulse valves to the air, the average lifetime of strontium ions was about two hours during the experiment. And with the copper tubing and vacuum-sealed pulse valves, the lifetime is extended to a few days.

The helium-nitrogen mixture is prepared in a ConFlat® nipple. The nitrogen versus helium ratio can be tuned arbitrarily, with the total pressure below 2.5 bar. We typically use the mixture with 20% nitrogen and 80% helium. To prepare the mixture gas, we charge the nipple with 1.6 bar of helium, then increase the total pressure to about 2 bar with nitrogen, and let the gas mix in the nipple for six hours. When the mixture is ready, it is sent to back the mixture pulse valve for the experiment. The neon pulse valve is always backed by 2 bar of neon directly coming from the cylinder and regulator.

The pulse valves' vacuum sides are connected together to a tube going to the ion trap region. Once the pulse valve is opened, the gas will first pass through a vacuum feedthrough on the main chamber and a flexible stainless steel bellows, the middle of which is thermally anchored to the outer radiation shield via copper wires. Afterward, the gas will get into a copper tube mounted on the inner radiation shield (see figure 3.3 b). The copper tube has a weak thermal connection to the inner radiation shield via a stainless steel shim. And with a heater and a silicon diode temperature sensor mounted together with the tube, we are able to control tube temperature between 12 and 18 K. The buffer gas will approximately thermalize to the copper tube temperature

and then be transferred to the ion trap. Notably, the cold copper tube helps to remove the contamination in the buffer gas but also reduces the nitrogen concentration at the same time. The neon pressure is also limited if the tube temperature is below 13 K.

3.5 Laser System

Our laser system includes two lasers for laser cooling $^{88}Sr^{+}$ and a mid-infrared laser to drive the ro-vibrational transitions of the molecular ions.

3.5.1 Energy Levels of $^{88}Sr^{+}$

$^{88}Sr^{+}$ is the atomic ion used to sympathetically cool the molecular ions and read out the information. It is chosen for its suitable mass and the alkali-like electronic configuration, which leads to a simple energetic structure. Its energy levels and transitions are well studied and shown in figure 3.21.[56, 57] In this work, we use a 422 nm laser to drive the cooling transition 5s $^2S_{1/2} \rightarrow$ 5p $^2P_{1/2}$, and a 1092 nm laser to prevent the accumulation on the meta-stable 4d $^2D_{3/2}$ by repumping it back to the 5p $^2P_{1/2}$ state. The two lasers are stabilized to Doppler-cool the $^{88}Sr^{+}$ ions and the coulomb crystal to milliKelvin temperatures. Additional lasers can enable optical pumping to the 4d $^2D_{5/2}$ state, which enriches the readout methods, but are not used in this work.

3.5.2 422 nm Laser

Our 422 nm laser source is a Littrow design narrow linewidth external cavity diode laser (MOGLabs LDL) controlled by the Moglabs DLC202HC controller. The laser has an output power of about 27 mW in the desired frequency range, which decreases to 18 mW after the isolator. The laser frequency is fine-detuned by the diode current and the

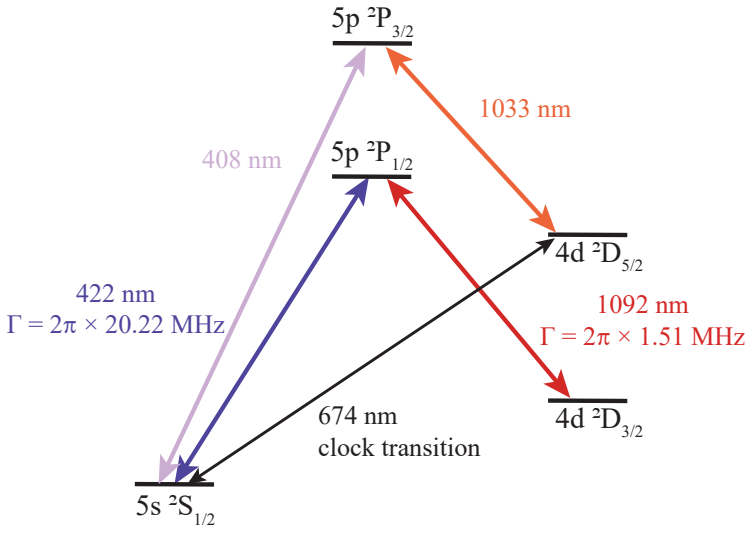

Figure 3.21: The partial energy level diagram of $^{88}Sr^{+}$

piezo-controlled cavity. And it is stabilized, referring to Rubidium's saturated absorption spectrum (SAS), and coupled to a single mode fiber to the trap. (Note: Most fiber couplings in our lab are done with Thorlabs' FC/APC adjustable aspheric collimators.) The layout of the optics is shown in figure 3.22.

The frequency of the 5s $^2S_{1/2} \rightarrow$ 5p $^2P_{1/2}$ transition of $^{88}Sr^{+}$ is known to be about 440 MHz higher than the 5s $^2S_{1/2}(F = 2) \rightarrow$ 6p $^2P_{1/2}(F' = 3)$ transition of neutral ^{85}Rb at 710.9624013 THz.[58, 59] Leveraging this fact, we can stabilize our 422 nm laser relative to the saturated absorption lines of the 5s $^2S_{1/2}(F = 2) \rightarrow$ 6p $^2P_{1/2}(F' = 2, 3)$ hyperfine transitions in neutral ^{85}Rb, and frequency-shift it closer to the cooling transition frequency of $^{88}Sr^{+}$ with an acousto-optic modulator (AOM).

Two Double-pass AOM setups are used in the 422 nm laser system. The AOM in the upper half of figure 3.22 is driven at 260 MHz, and the one in the lower half is driven by a frequency-modulated signal around 80 MHz. The two AOMs are from IntraAction Corp. (ATM - 2601A23 and ATM - 801A23). Phonons are generated in a longitudinal acoustic mode of the optical crystal in the AOM, which interact with the laser photons.

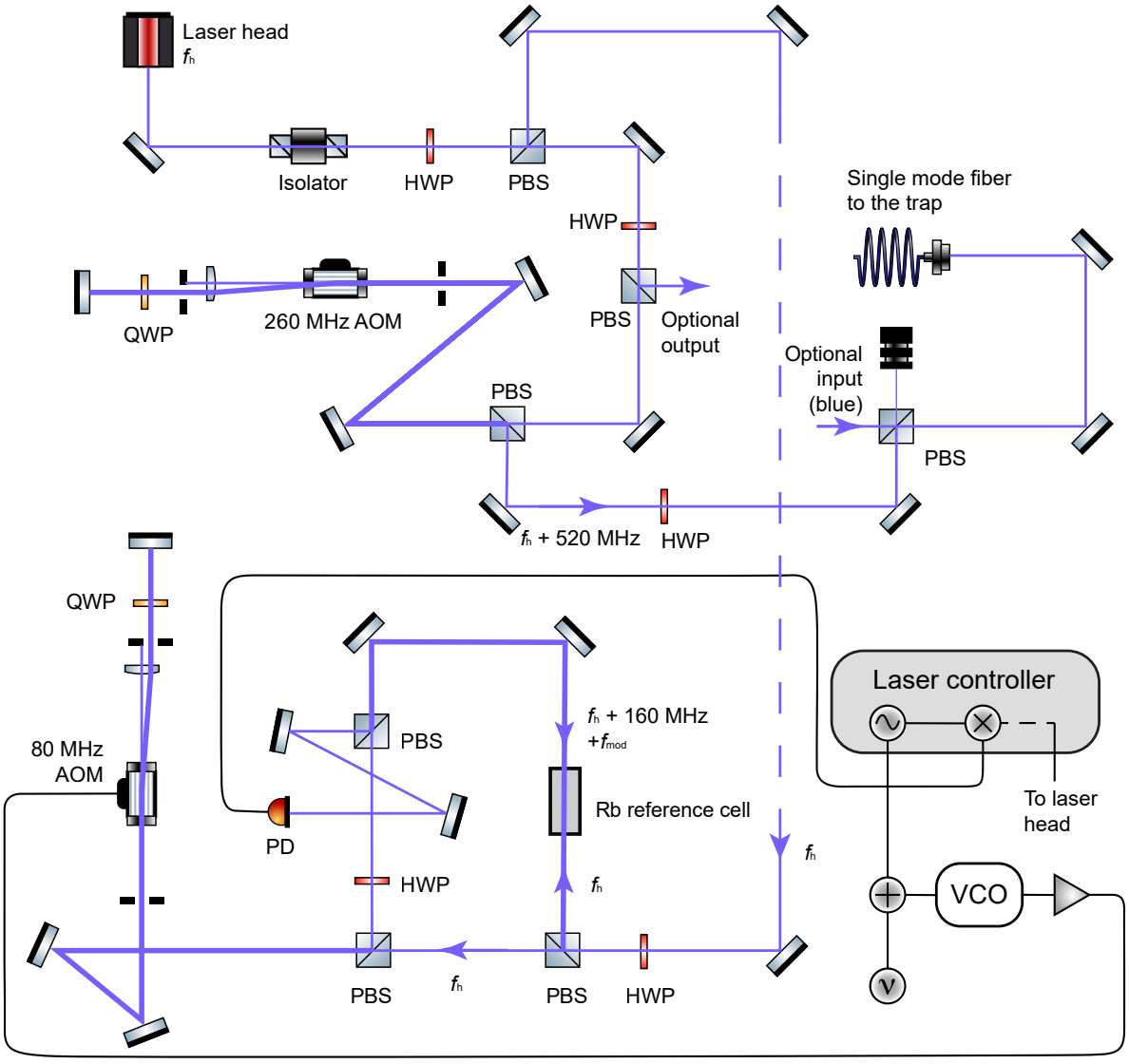

Figure 3.22: The layout of the optical system for 422 nm laser. About 5 mW of the laser is sent to the Rb reference system shown in the lower half of the figure. The rest is sent toward the ion trap after frequency-shifted for 520 MHz by double-pass an acousto-optic modulator (AOM). The bold line indicates co-aligned counter-propagating beams. HWP half wave plate, QWP quarter wave plate, PBS polarizing beamsplitter cube, AOM acousto-optic modulator, PD photon detector, VCO voltage-controlled oscillator.

The photon can either absorb or emit n phonons at the driving frequency, forming the $\pm n$ orders of the output. The energy and momentum are conserved during this process,

resulting in a spatial separation and varied optimal conditions for different orders of the output. In the experiment, we only use the +1 order, and the AOM orientations are optimized for it. A plano-convex lens focuses the outputs of the AOM, and the orientations of the beams become parallel to the original beam. They are all focused onto a mirror, which is fixed to be normal to all beams. Between the lens and the mirror, an optical iris and a quarter wave plate (QWP) are set to select the +1 order and change the polarization of the laser. Being retro-reflected by the mirror, the first-order output goes back to the AOM along its original beam path. The beam interacts with the phonons again and generates a new series of outputs. The new +1 order output counter-propagates the original incident beam and is selected by another iris as the output of the double-pass AOM configuration. It is split from the incident beam at the polarizing beamsplitter cube (PBS) due to the 90° polarization shift double-passing the QWP. The output frequency is higher than the input by two times the AOM driving frequency. The efficiency of our double-pass AOM setups is about 50%. And the output orientation is independent of the AOM driving frequency.

The saturated absorption spectroscopy of Rubidium is performed as shown in the lower half of figure 3.22. The laser is separated into a high-power pump beam and a low-power probe beam at a PBS. The probe beam is deflected directly to the Rb reference cell (Thorlabs GC19075-RB), and the pump beam is sent toward a second PBS. After going through the second PBS, the pump beam double-passes an AOM driven by a frequency-modulated signal around 80 MHz. The double-pass configuration shifts the laser frequency up by 160 MHz and an additional small modulation frequency oscillating at 250 kHz. It is then directed to the Rb reference cell by a pair of mirrors, counter-propagating the probe beam. In the Rb reference cell, the counter-propagating probe and pump beam interact with the same set of Rb atoms, which enables Doppler-free saturated absorption spectroscopy.[60] Passing the Rb cell, the probe beam is deflected

by a PBS to a photon detector, the count of which is used to represent the transmittance of the Rb vapor cell. By scanning the laser head frequency, we can measure the saturated absorption spectrum of the Rb vapor near 422 nm. The spectrum is recorded, assigned, and shown in figure 3.23.

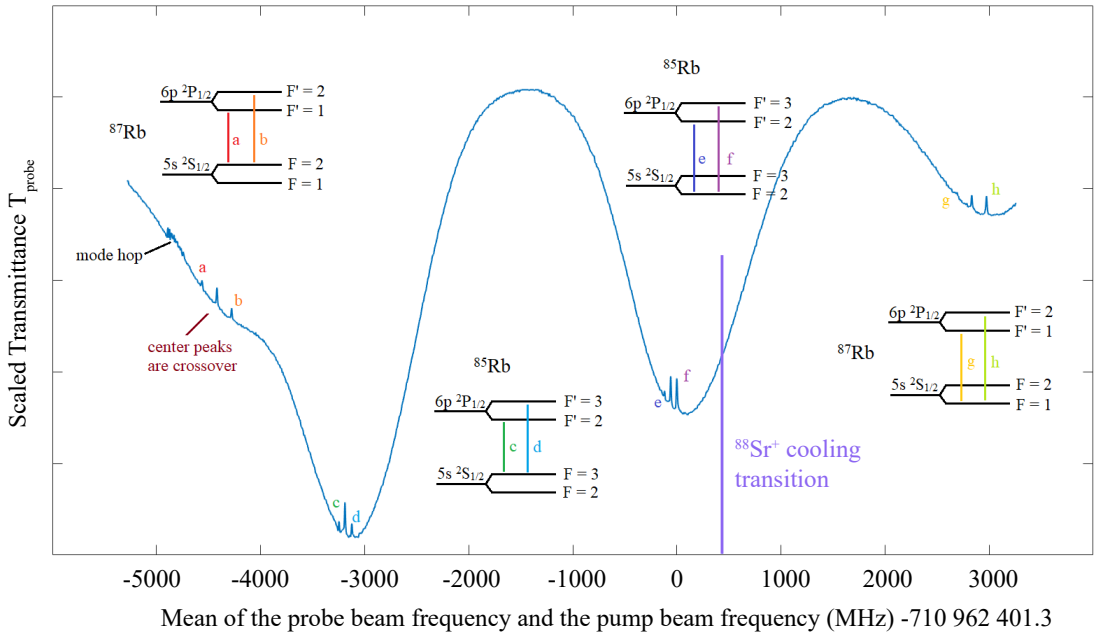

Figure 3.23: The saturated absorption spectrum of Rubidium. The broad features show Doppler-broadened absorption. And the narrow peaks are the saturated absorption lines where the pump beam saturates a part of the atoms the probe beam is driving. All the 5s $^2S_{1/2} \rightarrow$ 6p $^2P_{1/2}$ hyperfine transitions of neutral ^{85}Rb and ^{87}Rb are observed. Crossover peaks are seen in between each pair of adjacent hyperfine transitions. The center of the broad feature tends to have a higher frequency than the SAS lines due to the frequency difference between the probe and pump beams.

The Rb sample in the reference cell contains two isotopes, ^{85}Rb and ^{87}Rb. To produce enough gas phase Rb, the Rb reference cell is heated to above 90°C by three rod-heaters wrapped together with the cell in thermal insulating materials. The average speed of the Rb atoms' thermal motion is about 200 m/s, which leads to a Doppler-broadened absorption linewidth of about 0.5 GHz. This broad linewidth indicates the probe beam is always absorbed with some Rb atoms with a specific velocity. The frequencies of the two

beams in the atom frame are shown in figure 3.24 as functions of the atom velocity. In a fairly large rest frequency range, the probe laser frequency coincides with the transition frequency at velocities where Rb vapor has a significant thermal population. However, in special cases where the mean frequency of the two beams equals the transition frequencies or the mean of the two adjacent transition frequencies, the two beams are absorbed by the Rb atoms at the same velocity. In those cases, the pump beam optical pumps the Rb atoms to excited states, leaving a limited amount of Rb atoms at the 5s $^2S_{1/2}$ state for the probe beam to interact with. Hence, increases in the transmittance are observed in those cases, which give the SAS peaks. Figure 3.24 shows the case where the crossover peak between the 5s $^2S_{1/2}(F = 2) \rightarrow$ 6p $^2P_{1/2}(F' = 2, 3)$ transition of neutral ^{85}Rb is observed. We typically lock the laser to this peak or free-run the laser close to this peak to obtain a laser output 60 MHz red-detuned from the $^{88}Sr^+$ cooling transition.

The frequency modulation of the AOM enables the locking of the laser. A 250kHz modulation signal provided by the laser controller is added to the 9.3 V static input of the voltage-controlled oscillator (VCO, Mini-Circuits® ZX95-100-S+), the output of which is amplified to drive the 80 MHz AOM. Thus the frequency of the pump beam is modulated by the 250kHz signal. Near the saturated absorption peaks, the frequency shift affects the saturation effect, so the photon detector signal is also modulated at 250 kHz. The modulation's phase and amplitude depend on the relative position between the laser frequency and the transition, and this information is extracted to get the error signal. The error signal can be used as the feedback signal to control the current and the piezo voltage, which locks the laser frequency. The laser frequency is stabilized within a few MHz by this method.

The 422 nm output frequency and power are fine-tuned by the amplitude and frequency of the 260 MHz AOM's driving signal.

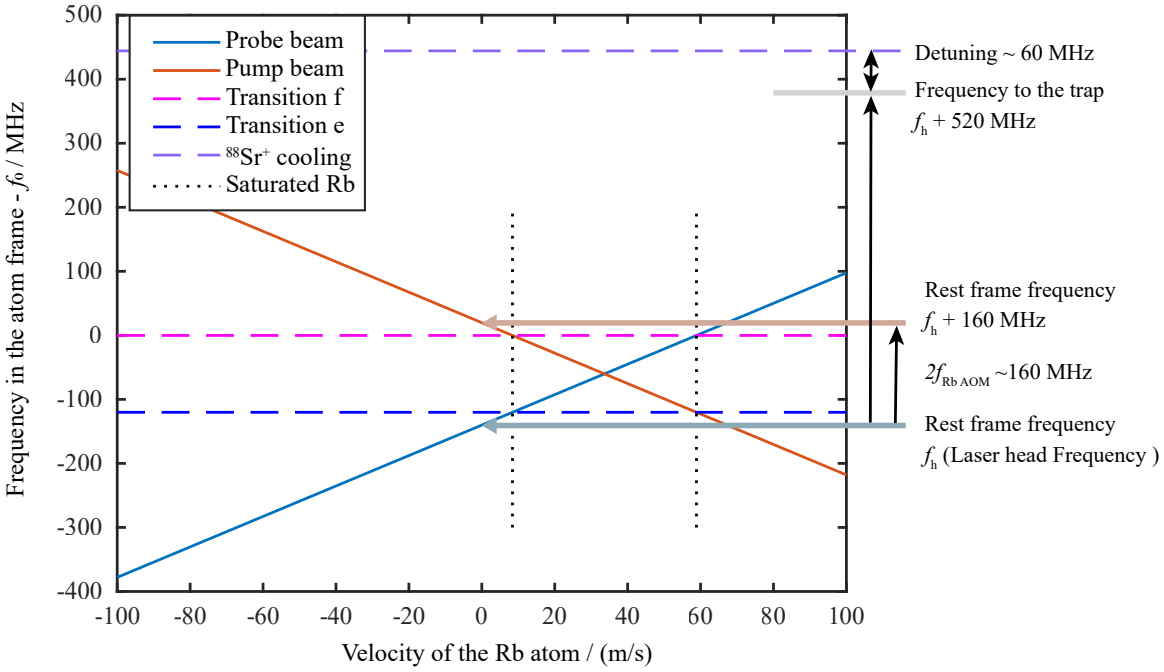

Figure 3.24: The Doppler-shifted frequencies of the pump and probe beams in the atom frame versus the atom's velocity. If the shifted frequency hits a transition frequency, the beam will drive the transition and be absorbed by the atoms at that velocity. If both beams are absorbed by the atoms at the same velocity, those atoms will be saturated, and the absorption of the probe beam will be suppressed. When the crossover peak between the transition e and f is observed, the mean of the probe beam frequency and the pump beam frequency equals the mean of the two transition frequencies. The frequencies of the laser output to the ions and the $^{88}Sr^{+}$ cooling transition are also marked in the figure.

3.5.3 1092 nm Laser

Our 1092 nm repump laser is generated by a DBR monolithic wavelength-stabilized laser diode (PH1092DBR080T8 from Photodigm) on a heat sink mount with a laser diode controller from Stanford Research Systems (LDC501). The diode has a temperature coefficient of wavelength of about 0.08 nm/K. The 1 mK temperature resolution and stability of the heat sink and the controller can stabilize the laser frequency to about 20 MHz level. The power output of the diode is about 35 mW with an 80 mA driving current, but the beam quality is poor.

The layout of the optics for the 1092 nm laser is shown in figure 3.25. The major part of the optics is designed to improve the beam quality. An adjustable slit right after the collimating lens removes the two wings from the near elliptical central beam. Two cylindrical lenses with a focal length ratio close to the axial ratio of the beam focus the beam in both dimensions to a pinhole (an almost closed iris), which acts as a spatial filter. After the iris, the beam becomes near Gaussian and is collimated by a spherical lens. Then, it is split and sent to two wavemeters and the ion trap. Near the end, a pair of cylindrical lenses further improve the beam quality for a higher coupling efficiency to the single mode fiber to the trap. About 2 mW of the 1092 nm laser is sent to the trap center, which always saturates the 4d $^2D_{3/2} \rightarrow$ 5p $^2P_{1/2}$ transition of $^{88}Sr^+$.

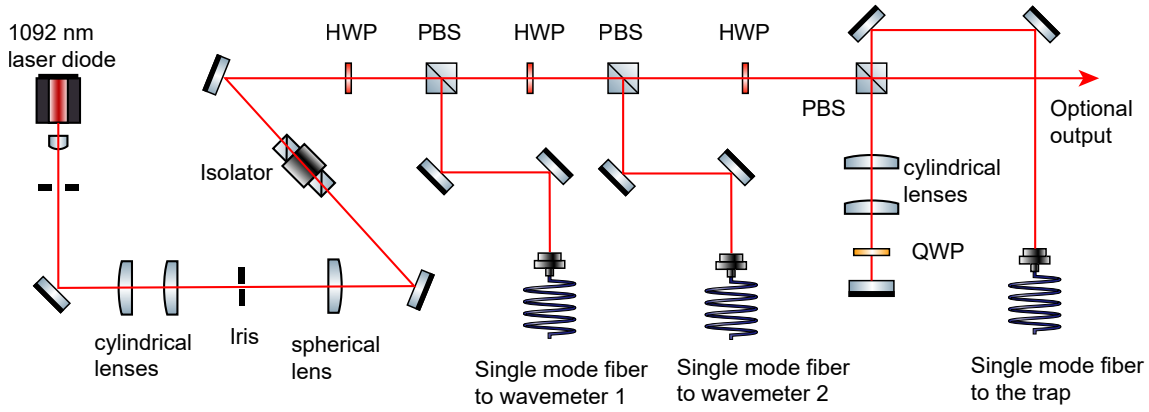

Figure 3.25: Optical layout of the 1092 nm laser system

The 1092 nm laser frequency is monitored by two wavemeters, a WA-1000/WA-1500 from Wavemeter® and a WaveMaster™ Laser Wavelength Meter from Coherent. Both of them have a frequency resolution of 100 MHz and an accuracy of a few hundred MHz. Fortunately, they tend to have opposite temperature responses, and the average of the readouts gives a good enough reference for rough adjustment so that we can obtain a signal from the $^{88}Sr^+$ ions. We typically adjust the temperature until the frequency is close to 274.5888 THz and then fine-tune the temperature to maximize the $^{88}Sr^+$

fluorescent.

3.5.4 Mid-infrared Laser and Co-alignment

In our experiments, we tried two mid-infrared (mid-IR) lasers to drive the rovibrational transitions of the molecular ion. They are used in the same way, and only one is used at once.

The first mid-infrared laser is a pulsed mid-IR optical parametric oscillator (OPO) light source (M Squared Lasers, Firefly IR). It is tunable from 2700 cm^{-1} to 4000 cm^{-1} (from 2.5 μm to 3.7 μm), and has a linewidth of about 6 cm^{-1}. It has a repeating rate of 150 kHz, which can be considered as a quasi-continuous wave in our experiment. The frequency of the Firefly IR laser is determined based on internal calibration. We verified the calibration by recording the absorption spectra of solid polystyrene and ammonia vapor, compared with the data provided by NIST.

We have temporarily replaced our first mid-infrared laser with a rented narrow linewidth CW laser, TOPTICA's mid-infrared tunable laser (TOPO). We use the idler output from the OPO sytem. It has a linewidth of 2 MHz (0.00006 cm^{-1}), which is significantly smaller than that of the Firefly laser and the linewidth of the tagged complexes' rovibrational transitions. This laser helps to determine the resolution limit of our experimental method and may have allowed us to resolve the P, Q, and R branches of the rovibrational transitions. The frequency of the output is calculated based on the monitored frequencies of the pumping light and the signal output.

The mid-infrared laser is coaligned with the axial beam going to the ion trap center. Figure 3.26 shows their beam path near the trap. The mid-infrared laser has a beam waist of about 0.5 mm near the trap center.

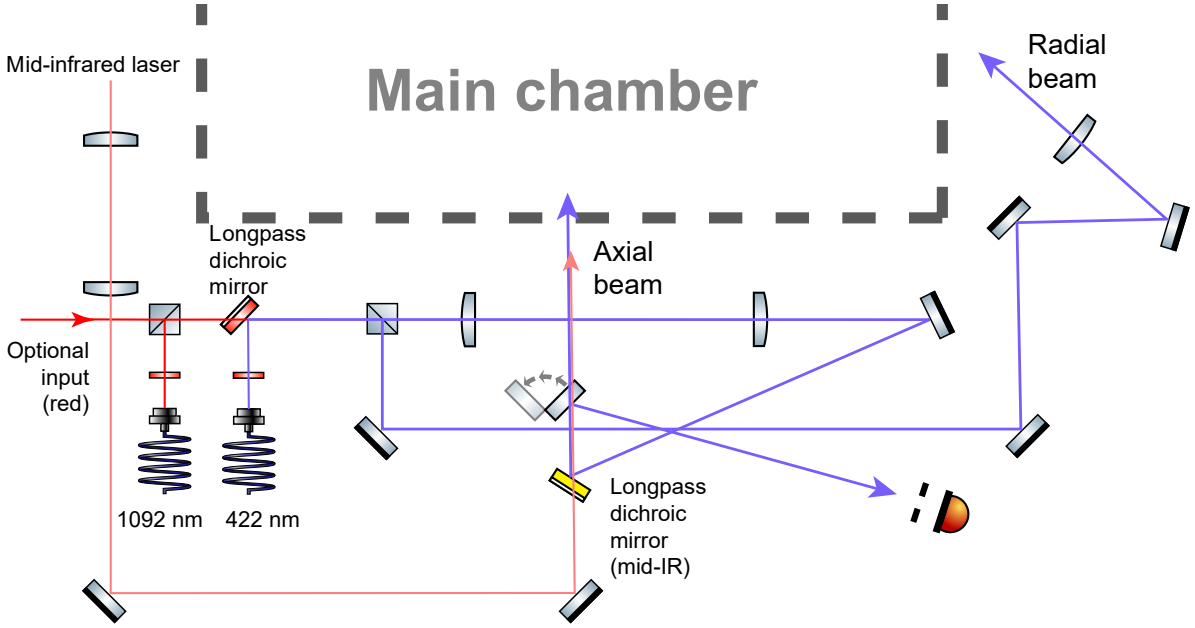

Figure 3.26: The optical layout near the main chamber. The 1092 nm laser is co-aligned with the 422 nm laser. They are split into axial and radial beams to laser cool the axial and radial motions of the $^{88}Sr^{+}$ ions. A flip mirror and an iris, the image of which is aligned with the trap center, are used to align the axial beam through the trap's end caps. The beam width of the axial beam is about 0.2 mm near the trap center. The mid-infrared laser is co-aligned with the axial beam.

3.6 Imaging System

We built two imaging system sets to monitor the $^{88}Sr^{+}$ ions at 422 nm from the side and the bottom, respectively. The one below the trip is our main imaging system, featured with a 0.28 NA objective lens set and $\times 5$ magnification. And the side imaging system, which has a simple optical design and $\times 2.5$ magnification, is integrated on an optical breadboard and is easy to set up and remove (see in figure 3.3 a)).

The layout of the two imaging systems are shown in figure 3.27. The 3D imaging of the ions are achieved with two CCD cameras (Retiga R1^{TM} from Q Imaging). The cameras have a 1360 $\times$ 1024 CCD array and 6.45 μm $\times$ 6.45 μm pixel size. The quantum efficiency is about 50 %. And the exposure time is tunable between 25 μs and 3600s. Working with the imaging system, the bottom camera provides a spatial resolution of

about 1.5 μm at the trap center, and the side one has a resolution of about 3 μm. A better resolution may be achieved by mounting the camera on a micrometer driven translation stage. Two photos of the same ion chain taken by the bottom and side camera are shown in figure 3.28.

Our main imaging system on the bottom collects photons efficiently without sacrificing the imaging quality. The objective is mounted on a 2D translation stage attached to the room-temperature main chamber. The objective is to be as close as possible (about 50 mm away) to the trap center for a short working distance. The lens set consists of four spherical lenses and two precisely machined spacers, the geometry of which is optimized for minimal spherical aberration and distortion. Its effective numerical aperture of 0.28 allows the collection of 2% of the total scattered photons from $^{88}Sr^{+}$ ions. The objective can be moved horizontally in a few centimeters to roughly align to the trap center. The image of the ion is centered on the adjustable mechanical slit (see g in figure 3.27) with the elliptical mirror. The mechanical slit is used to manually select the field of view and limit the number of photons from the background. It can be moved together with the lens h in figure 3.27 within the travel of the adjustable collimation adapter to be fine-aligned with the image plane of the ions. This type of adjustment can compensate for an ion's vertical motion of about 1 mm. The lens i further focuses the light to the camera and the PMT. Figure 3.29 shows a 2D Gaussian fitting to a photo of a single $^{88}Sr^{+}$ ion in the trap taken by the bottom camera. The standard deviation of the axial distribution is about 2.8 pixels, and that of the radial distribution is approximately 1.4 pixels, which correspond to 3.6 μm and 1.8 μm, respectively. The axial distribution corresponds to a thermal distribution at about 4 mK. And the radial spread is mainly caused by the resolution limit of the imaging system.

About 70 % of the photons collected by the bottom objective are shuttled to a PMT (HAMAMATSU H10682-210). With the adjustable mechanical slit spatially selecting

these photons, we can efficiently analyze the temporal distribution of the photons scattered by the ions. The pulsed PMT signal is counted by a frequency counter (BK Precision 1823A). During the experiment, the PMT typically has a count rate of 6 kHz from a single $^{88}Sr^{+}$ ion when the cooling laser is 60 MHz red-detuned and about two times the saturation intensity. The rate will rise to 28 kHz if the detuning is near zero. And the typical background count rate is about 10 kHz. The PMT signals can also be analyzed by spectrum card and lock-in amplifier after being converted to longer pulses by a Stanford Research Systems DG535 Digital Delay / Pulse Generator.

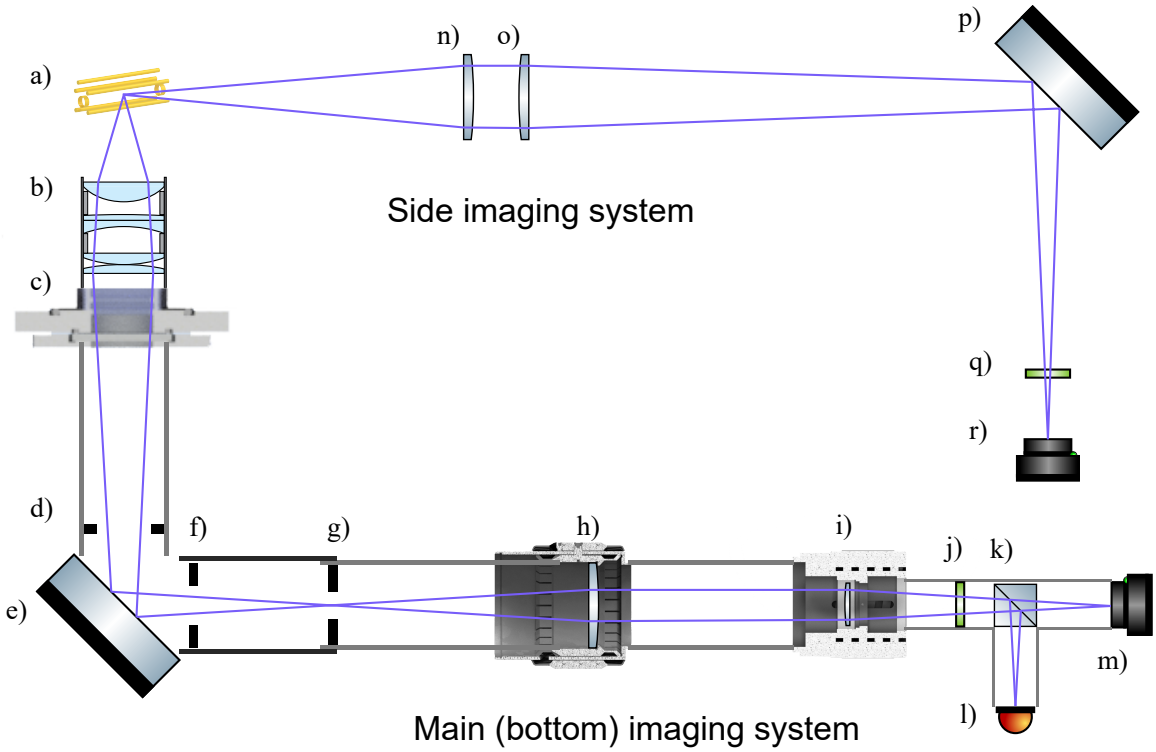

Figure 3.27: The side and bottom (main) imaging system. a) $^{88}Sr^{+}$ scattering photons at the center of the ion trap. b)0.28 NA objective lens set. It has a working distance of 50 mm and $\times 5$ magnification. c) 2D translation stage to roughly align the objective. d) and f) Fixed optical apertures to cut down background scattering. e) and p) A two-inch elliptical mirror in a kinematic mount. g) A two-dimensional adjustable mechanical slit located at the image plane of the objective. h) Two-inch diameter $f = 150$ mm plano-convex lens in an adjustable collimation adapter (Thorlabs SM2F). The slit g is fixed to its focal plane. i) One-inch diameter $f = 150$ mm plano-convex lens in a non-rotating zoom housing (Thorlabs SM2NR1). j) and q) 420 nm bandpass filter (Thorlabs FBH420-10). k) 70:30 (R:T) cube beamsplitter. 1) PMT. m) and r) CCD camera. n) Two-inch diameter $f = 200$ mm plano-convex lens on a linear translation stage. o) Two-inch diameter $f = 500$ mm plano-convex lens

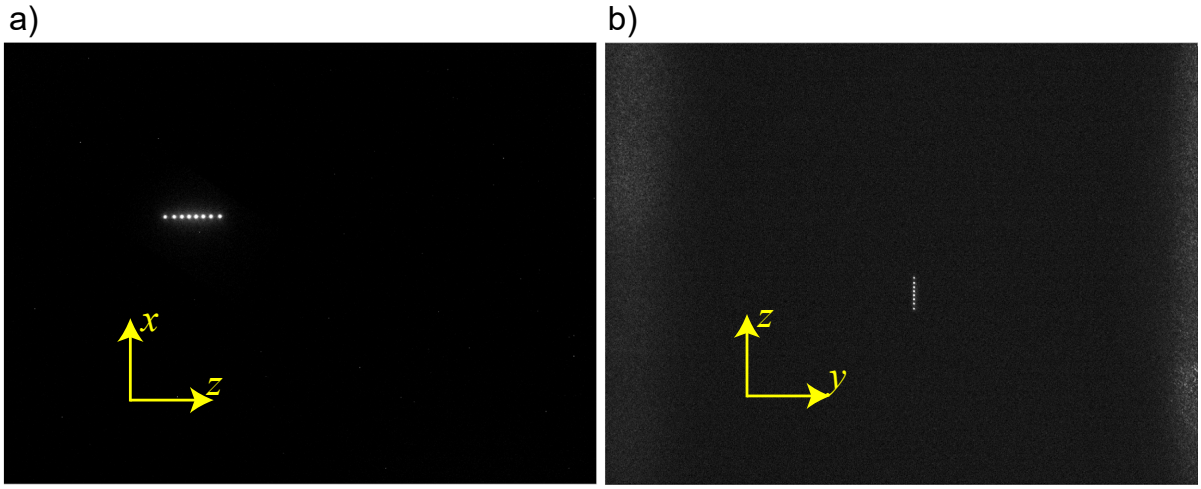

Figure 3.28: A chain of ions imaged from the a) bottom camera and b) side camera. The x and y indicate the two radial axes of the ion trap, and the z-axis is along the axial direction. The whiteish color on the left and right sides of image b is due to the scattered light from the trap rods.

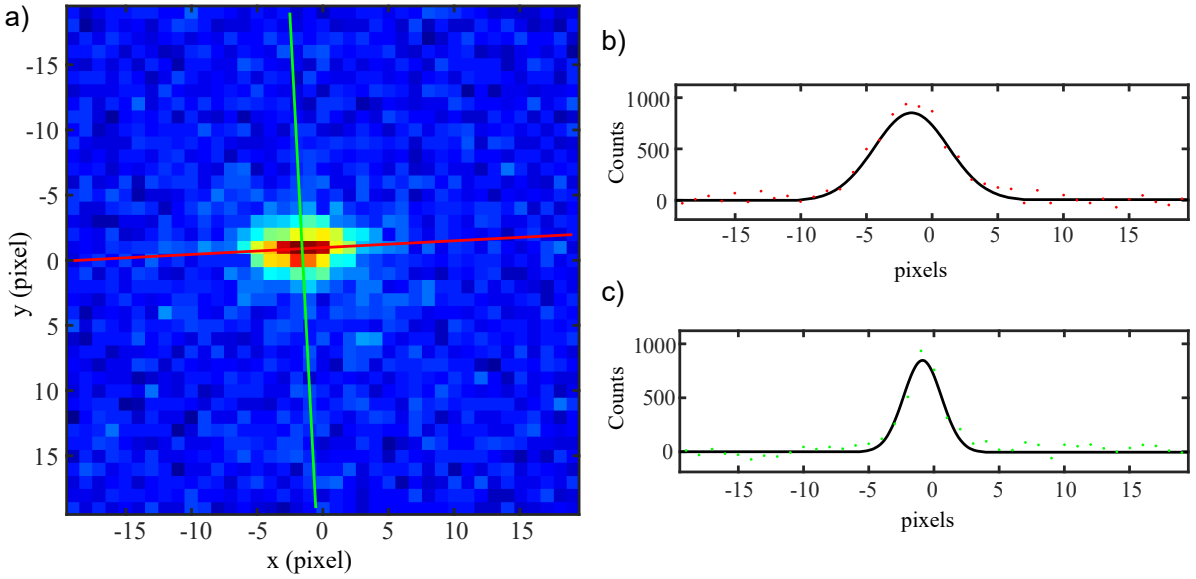

Figure 3.29: a) A zoomed-in image of single $^{88}Sr^{+}$ in the ion trap. The axial secular frequency is measured to be 28 kHz. b) Gaussian fitting along the axial direction (the red line). c) Gaussian fitting along the radial direction (the green line).

Chapter 4

Chapter 4 Experimental Technique

This chapter discusses the basic experimental techniques served in our single molecular ion experiment, including buffer gas cooling, sympathetic cooling, nondestructive mass spectrometry, and preparing the molecular ion–tag Van der Waals complex. They are the essential tools that allow us to study the ions and record vibrational spectra with single molecular ions via the cryogenic ion vibrational predissociation (CIVP) method. With these tools, we can robustly prepare a $^{88}Sr^{+}$-molecular ion Coulomb crystal at milliKelvin temperatures, determine the mass of the molecular ion, and tag the molecular ion with a single nitrogen molecule.

4.1 Prepare the Coulomb Crystal

Ion Coulomb crystal is a unique ordered state of an assembly of trapped ions with the same sign of charge.[61, 62] It is observed in laser-cooled ion trap experiments where the ions' motion is at or below milliKelvin temperatures.[63] At higher temperatures where the average kinetic energy is comparable to the electric potential energy between ions, the ions have a liquidlike behavior, which look like a cloud on the camera. When the

electric potential energy between the adjacent ion pair is larger than 170 k_BT, the ions become localized and spatially separated to a crystal-like structure, which is called the ion Coulomb crystal.[64, 65] The distance between the adjacent ions in the crystal are usually in the range of 5 - 50 μm. With such a short distance, the strong Coulomb repulsion between ions becomes the dominant term of the translation motion. It results in a strong coupling of ions' motion and enables spatial addressing of individual ions. The spatial separation prevents short-range interactions between ions that affect the internal degrees of freedom. Such a stably isolated environment makes the ion Coulomb crystal an ideal platform to address and study single molecules.

The structures of ion Coulomb crystals vary based on the trapping potential, the number of ions, and the ions' species. To simplify the problem, our experiment mainly focuses on two or three-ion crystals containing one molecular ion. And only two-ion crystals are used to take the single molecule vibrational spectra. The following of this section discusses how we prepare such crystals.

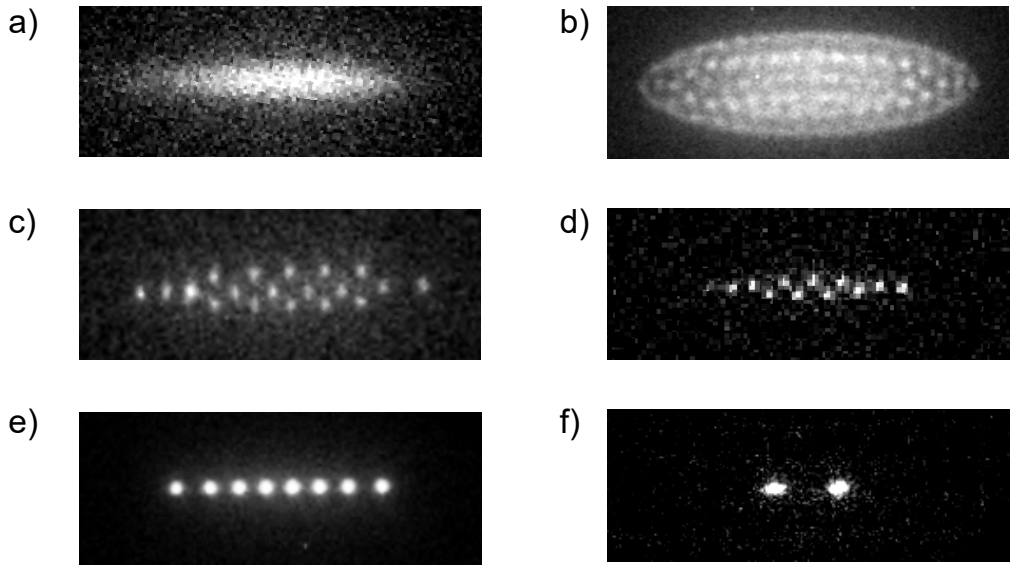

Figure 4.1: $^{88}Sr^{+}$ ion cloud and ion Coulomb crystals. a) Ion cloud. b) A large ion crystal with multiple layers. c) A smaller ion crystal with a zigzag-like structure. d) Zigzag ion chain. e) Linear ion chain. f) Two-ion crystal.

4.1.1 Ion Loading with Buffer Gas

Our ions are generated in the Extrel chamber and shuttled to the ion trap through the quadrupole mass filter (QMF) as illustrated in section 3.3. The kinetic energy of these ions ranges between 7 eV and 20 eV. The barrier of the axial confinement set by the end cup is typically a few Volts lower than the ions' energy. In order to let the ions remain in the conservative trapping potential, an initial cooling procedure with the buffer gas is necessary to dissipate the excess energy within μs time scale. The collisions with buffer gas efficiently take energy away from the ions and eventually cool the ions that stay in the trap to about 10 Kelvin, where laser cooling and sympathetic cooling take the job to further cool the ion. In this subsection, we will focus on the ion loading schemes of the $^{88}Sr^{+}$ and the molecular ions with buffer gas. These schemes are optimized to load the few-ion crystals controllably.

Neon is chosen to be the collision partner and the buffer gas for initial cooling. Our buffer gas must be chemically inert and have a non-negligible vapor pressure at the cryogenic temperature to interact and exchange energy with the ions efficiently. As introduced in the buffer gas section 3.4, the ultimate temperature of the buffer gas tube is around 14 K. At this temperature, only neon, hydrogen gas, helium, and their isotopes can remain at a good pressure. Among them, the neon atom has the largest mass of 20 Dalton. A larger mass indicates the particle can take away more kinetic energy during a collision with the high-energy ion. As a result, fewer collisions are needed to dissipate the same amount of energy with neon than that with helium or hydrogen. Notably, the probability of having a collision event is low at low pressure. The probability that a high-speed ion confronts a certain amount of collisions in the trapping region decreases exponentially as the number of collisions increases. Hence, hydrogen and helium could hardly suit the initial cooling purpose. And neon is the best buffer gas choice to load at

our temperatures.

After firing the pulse valve in the neon gas line, it takes about 20 ms for the gas pulse to reach the trapping region. The gas pulse can induce a temporary pressure increase before the neon gas is mechanically pumped or cryo-pumped. For a tens of millisecond long neon pulse, the peak pressure detected near the room temperature main chamber is at the order of 10^{-6} Torr, and the time constant of pressure dropping varies in between 0.3 s and 1 s. We expect the trapping region experiences a higher peak pressure and shorter pumping time due to the cryo-pumping effect at the 5.7 K inner radiation shield's surface.

$^{88}Sr^{+}$ is always the first ion species to load in our multi-species ion crystal. Its loading scheme is shown in figure 4.2. The ions are generated via laser ablations on aluminum-strontium alloy and mass-selected by the QMF. The energies of the $^{88}Sr^{+}$ ions vary greatly. But the energy of those ions, which can pass through the ion generation system, is typically around 18 eV. Those ions reach the trapping region within 300 μs after the firing of the laser. The total ion flow near the trap depends on the pulse laser's power, typically about a few hundred ions per pulse. We usually open the neon pulse valve for 50 ms 75 ms earlier than the laser pulses. If the ions arrive at the trapping region when the pressure is high enough to cause enough collisions, the ions will possibly be slowed down and trapped. The laser power, neon pulse length, and delay time can be adjusted so that the average number of ions loaded per pulse is below 0.3. Then the expected number of $^{88}Sr^{+}$ ions to load can be fine-controlled by the number of gas pulses in a sequence. We typically skip the first three laser pulses, where the laser pulse energy and ion generation efficiency are unstable, and eject neon before the subsequent three laser pulses. This sequence will likely load zero or one $^{88}Sr^{+}$ into the trap and barely affect any initially trapped ions. Thus, we can prepare a crystal consisting of an arbitrary number of $^{88}Sr^{+}$ ions by repeating this sequence and verifying the result with the camera.

A single molecular ion to study is loaded into the trap after the $^{88}Sr^{+}$. In this work, the

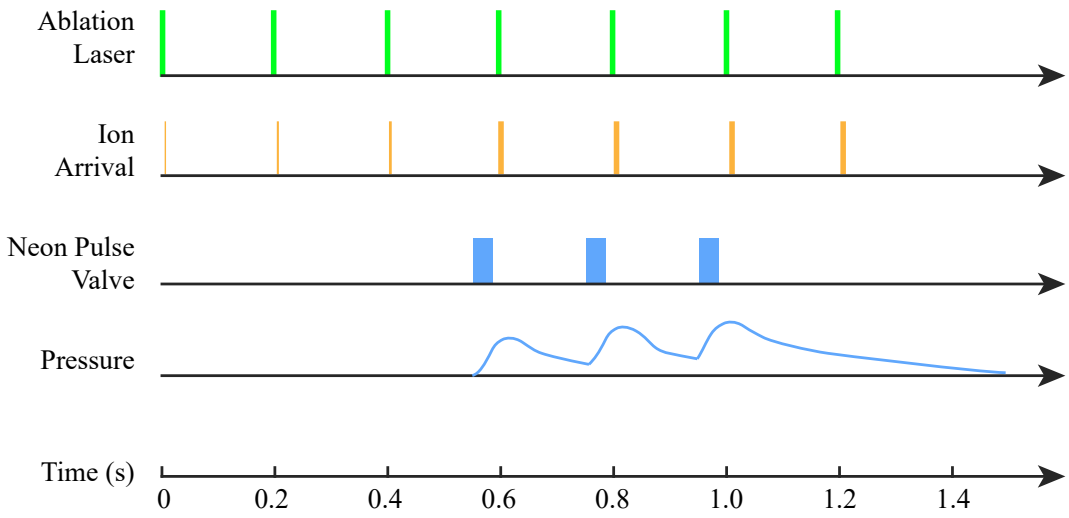

Figure 4.2: Schematic diagram of the $^{88}Sr^{+}$ loading process. The sequence is triggered by the Q-switch synchronizing signal of the first laser pulse. The laser's repetition rate is fixed at 5 Hz. The sequence triggers the pulse valve three times, producing three neon pulses shortly before the fourth, fifth, and sixth laser pulses. The sequence will load about one $^{88}Sr^{+}$ ion.

molecular ion is produced by electron impact ionization. Before loading, we usually verify mass spectra and the production of the molecular ions using the quadrupole deflector and the channel electron multiplier (CEM). The ion flow depends on the parent molecule's pressure, which the leak valve controls. It is typically adjusted so that the CEM detects a typical flow rate of 10^5 ions per second, which usually requires no more than 2×10^{-6} Torr of parent molecules. The molecular ion flow is less concentrated in the time domain but more uniform and long-lasting. An additional ring-shaped shutter electrode is used to gate the ion flow. The ion beam can go through the shutter electrode straightly if the electrode is grounded. However, if a high voltage is applied, the shutter electrode will reflect all the incoming ions. Typically, in a molecular ion loading sequence, the shutter is grounded for about 1 s and set to high voltage during the other time. A neon pulse for 80 ms is ejected to the trap and cools the ions while the shutter is grounded. Again,

this process typically loads zero or one molecular ion and is repeated until the correct number of ions are loaded.

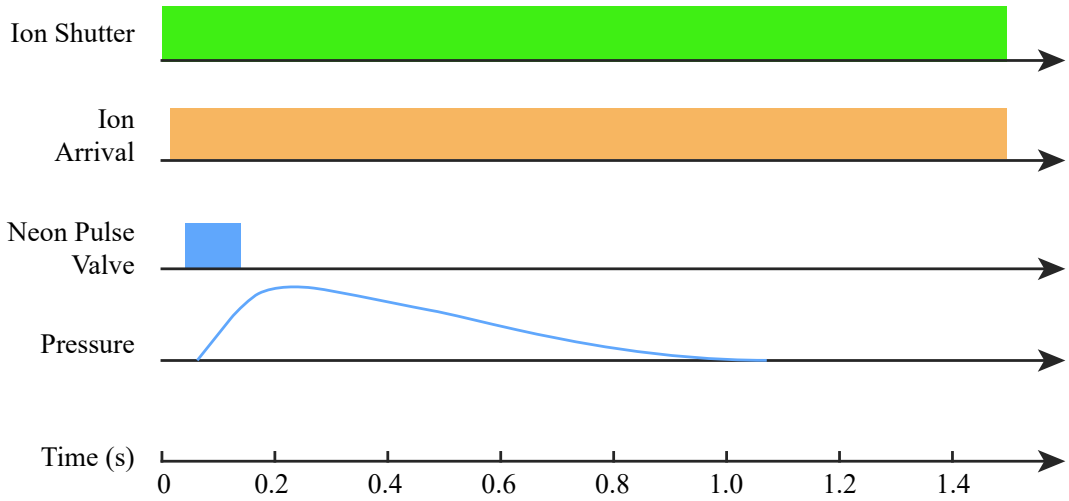

Figure 4.3: Schematic diagram of molecular ion loading process

Notably, molecular ions are much more fragile than atomic ions. The high-energy collisions during the initial cooling process may cause fragmentation and isomerization. If needed, the initial energy of the ions and the end cap voltages should be lowered to suppress the possibility of unwanted fragmentation and isomerization.

4.1.2 Doppler Cooling

The $^{88}Sr^{+}$ ions are buffer gas cooled to about 15 K and laser-cooled to milliKelvin temperatures. While a variety of advanced laser cooling techniques, such as sideband cooling and EIT cooling, are available, our experiments only require the most basic Doppler cooling. Our ion trap is run in the "weak-binding regime," where the spontaneous decay process takes place much faster than the secular oscillation in the trap potential. [66] In this regime, the cooling process can be treated the same way as the Doppler cooling of

free atoms. We typically red-detune the cooling 422 nm laser for 60 MHz and co-align it with the 1092 nm repump laser. The beam is split into axial and radial beams passing through the trap center in different directions. They slow down the $^{88}Sr^{+}$ ions when the ions move against their incident directions. The two beams provide Doppler cooling to both the axial and the radial modes of motion. In our experiments, the critical temperature is the crystallization temperature, where ions form Coulomb crystal and efficient sympathetic cooling is allowed. This temperature is way above the Doppler limit of $^{88}Sr^{+}$ of around 1 mK and is easy to reach.

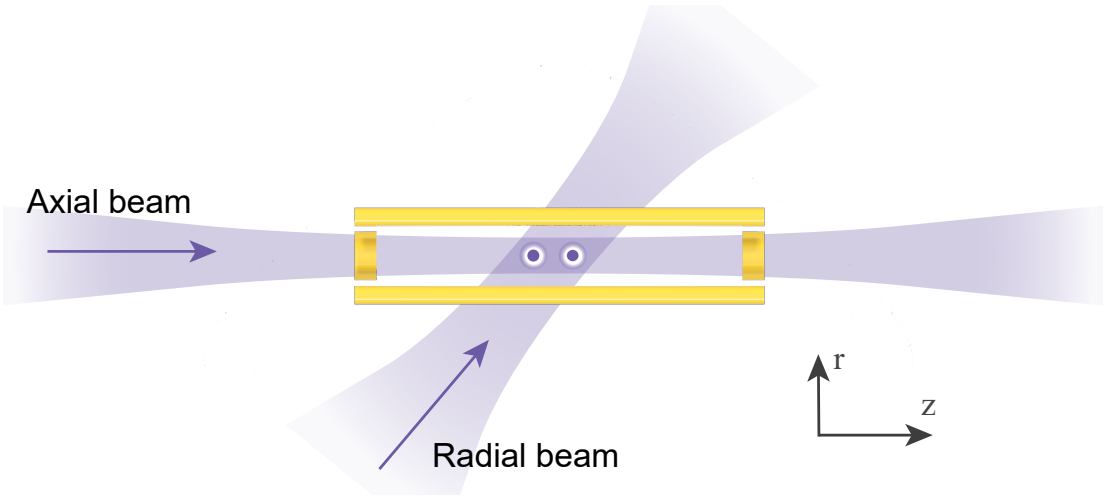

Figure 4.4: A top view of a schematic model of the laser beams. The axial beam is uniformly applied to all the ions on the trap axis but can only cool the axial motion. The radial beam cools the radial motion. The distance between ions is exaggerated.

The cooling laser not only Doppler cools the $^{88}Sr^{+}$ ions but also induces fluorescence containing the spatial and velocity information of the $^{88}Sr^{+}$ ions. The imaging system collects the spontaneous-emitted 422 nm photons. The CCD cameras resolve the spatial distribution, and the PMT detects the spontaneous emission rate relating to the velocity of the ion. In the "weak-binding regime," the electronic state of $^{88}Sr^{+}$ reaches equilibrium faster than the secular motion. And at each moment, we have the spontaneous emission

rate proportional to the average excited state population,

$$\frac{dN}{dt} = \Gamma\rho(5\mathrm{p}^2\mathrm{P}_{1/2}) \tag{4.1}$$

There is no accurate analytic model to predict the cooling dynamics of the particles having a Λ shape energy structure, like $^{88}Sr^{+}$.[67] But a rough estimation of the excited state population can be made by ignoring the D state and considering the ion as a two-level system.

$$\rho(5\mathrm{p}^2\mathrm{P}_{1/2}) = \frac{s/2}{1+s+(2\Delta_{eff}/\Gamma)^2}, \quad s \equiv \frac{2|\Omega_{Rabi}|^2}{\Gamma^2}, \tag{4.2}$$

where δ_{eff} is the effective angular frequency detuning of the 422 nm cooling laser counting the Doppler shift. Eq. 4.2 and 4.1 indicate a velocity-depended photon scattering rate, which is the key physics quantity measured in our experiments. Experimentally, we observe a typical count rate of 6 kHz at the PMT when the laser frequency is red-detuned by 60 MHz. It corresponds to a $\rho(5\mathrm{p}^2\mathrm{P}_{1/2})$ of about 0.02. The large red-detuning of the laser guarantees a negative δ_{eff} and a monotonic relationship between the velocity and the spontaneous emission rate, as long as the speed of the ion is lower than 20 m/s.

4.1.3 Modes of Motion and Sympathetic Cooling

The translational temperatures of the buffer gas loaded ions are around 15 Kelvin. At such a temperature, the ion assembly has a cloud shape and an axial spread of about 600 μm. The Coulomb interaction is strong enough to couple the translational motion of the ions with similar masses. Such a coupling allows the Doppler cooling effect to remove energy from the whole system via the $^{88}Sr^{+}$ ions. In other words, the laser-cooled $^{88}Sr^{+}$ ions sympathetically cool the other ions (the guest ions).[68] If all the guest ions are in

the favorable mass range and a good portion of the ion assembly is $^{88}Sr^{+}$, the whole ion assembly will be cooled together to milliKelvin temperatures and form an ion Coulomb crystal.

The total potential energy of the singly-charged ion system follows,

$$V = \sum_{i=1}^{N} \frac{1}{2} m_i \omega_{i,z}^2 z_i^2 + \sum_{i=1}^{N} \frac{1}{2} m_i \omega_{i,r}^2 r_i^2 + \frac{1}{2} \sum_{i=1}^{N} \sum_{j=1, j\neq i}^{N} \frac{e^2}{4\pi\epsilon_0 |\vec{x}_i - \vec{x}_j|} \tag{4.3}$$

The ion assembly crystallizes around the equilibrium position, where the potential energy V reaches the minimum. In the two-ion or three-ion crystal systems studied, we have $\omega_r \gg \omega_z$, and the ions are tightly confined on the trap axis, forming an ion chain. In this case, we can add a constraint that $r = 0$ and only consider the motion along the z direction (along the trap axis). And if the RF field along the trap axis can be ignored, $m_i \omega_{i,z}^2$ will be a constant for all the ions. Then we have,

$$V = \sum_{i=1}^{N} \frac{1}{2} u_0 z_i^2 + \frac{1}{2} \sum_{i=1}^{N} \sum_{j=1, j\neq i}^{N} \frac{e^2}{4\pi\epsilon_0 |z_i - z_j|} \tag{4.4}$$

The equilibrium positions of such potentials are independent of the ions' masses. However, the masses of the ions still show up in the kinetic energy. As a result, the collective motion of the assembly depends on the ion assembly's composition. Our experiment focuses on the two-species ion chains, consisting of $^{88}Sr^{+}$ ions and one guest ion. Figure 4.5 shows the structures and the images of those ion chains near their equilibrium positions. The guest ions have a negligible scattering cross section for 422 nm photons and are invisible on the cameras. However, the guest ion still occupies a site in the chain seen in figure 4.5 a). That site is temporarily dark but will be visible if it is occupied by $^{88}Sr^{+}$ after the ion flipping the positions. Hence, if the images have a shorter exposure time than the flipping rate, the image will likely distinguish the positions of the bright

$^{88}Sr^{+}$ and the guest on a dark site (see the lower images in figure 4.5 b and c). And if the exposure time is long enough, we will get an averaged image of the possible permutations in which all the occupied sites are bright. With these images, we can precisely count the number of the $^{88}Sr^{+}$ ions and the guest ions.

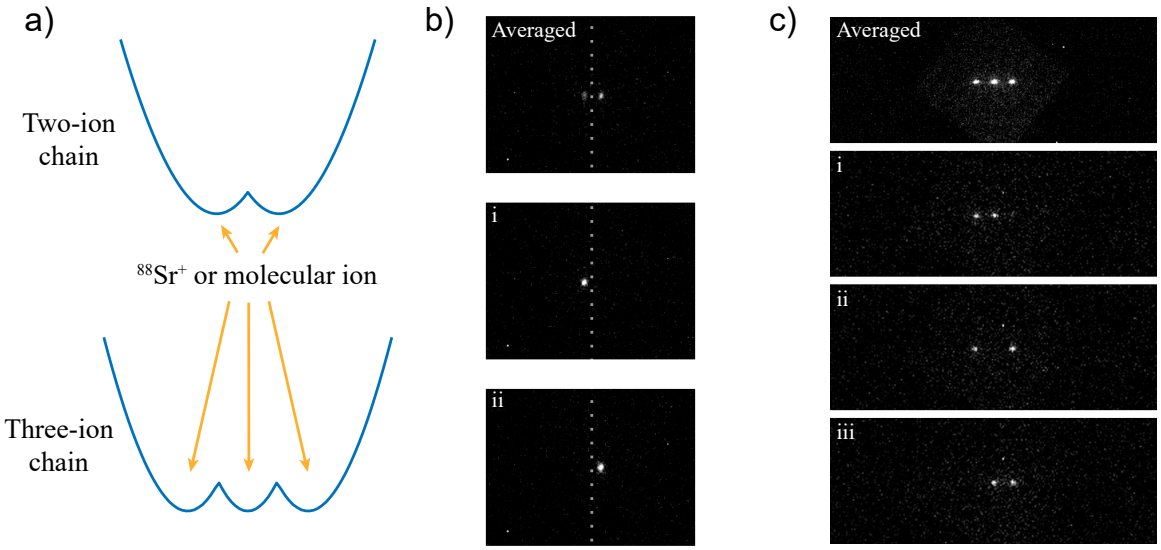

Figure 4.5: Two-ion and Three-ion Coulomb crystals. a) The minimum value of the potential energy V if the position of one ion is fixed. It is plotted as a function of the fixed ion's position. This function will reach a minimum if and only if the fixed ion's position coincides with one of the equilibrium positions. When the ion assembly reaches equilibrium, each of those minimum positions is occupied by one ion. b) Images of a two-ion crystal icluding one $^{88}Sr^{+}$ and one guest ion. The top image has a long exposure time showing all the ion sites. The rest images show all the possible permutations of the ions. c) Similar to b), the images of a three-ion crystal including two $^{88}Sr^{+}$ and one guest ion.

The equilibrium positions of equation 4.4 can be solved analytically when $N = 2, 3$.[10] Near the equilibrium positions, the collective motion of the ions can be studied using the small oscillations formalism. In the cases of two ion-species chains and $N = 2, 3$, the eigenfrequencies and eigenvectors of the collective oscillation have been reported.[10, 69] Assuming the trapping potential has been characterized by the motion of a single ion, we have the potential parameter u_0 as a function of the single ion's mass

and axial secular frequency. In our case, that single ion is $^{88}Sr^{+}$.

$$u_0 = m_{88}\omega_{z,88}^2 \tag{4.5}$$

Now we introduce the mass ratio between the guest ion and $^{88}Sr^{+}$ $\mu = m_{guest}/m_{88}$. Then the eigenfrequencies and eigenvectors of the normal modes can be written as functions of μ and $\omega_{z,88}$. For $N = 2$, the eigenfrequencies and eigenvectors are,

$$\omega_{\pm} = \omega_{z,88}\left(1 + \frac{1}{\mu} \pm \sqrt{1 + \frac{1}{\mu^2} - \frac{1}{\mu}}\right)^{1/2} \tag{4.6}$$

$$\vec{q}_{\pm} = N_{\pm}\left(\frac{1 - \mu \mp \sqrt{1 + \mu^2 - \mu}}{\sqrt{\mu}}, \frac{1}{\sqrt{\mu}}\right) \tag{4.7}$$

The first and second components of $\vec{q}$ refer to the motion of $^{88}Sr^{+}$ and the guest, respectively. ω_{-} is called the center of mass (COM) mode frequency, and the ω_{+} is the breathing (stretching) mode frequency. $N_{\pm}$ are the normalization factors.

For $N = 3$, if the guest ion is at the center, we will have,

$$\omega_1 = \omega_{z,88}\left[\frac{13}{10} + \frac{1}{10\mu}(21 - \sqrt{411 - 34\mu + 169\mu^2})\right]^{1/2} \tag{4.8}$$

$$\omega_2 = \sqrt{3}\omega_{z,88} \tag{4.9}$$

$$\omega_3 = \omega_{z,88}\left[\frac{13}{10} + \frac{1}{10\mu}(21 + \sqrt{411 - 34\mu + 169\mu^2})\right]^{1/2} \tag{4.10}$$

$$\vec{q}_1 = N_1\left(1, \frac{\sqrt{\mu}}{8}(13 - 5\frac{\omega_1^2}{\omega_{z,88}^2}), 1\right) \tag{4.11}$$

$$\vec{q}_2 = N_2\left(1, 0, -1\right) \tag{4.12}$$

$$\vec{q}_3 = N_3\left(1, \frac{\sqrt{\mu}}{8}(13 - 5\frac{\omega_3^2}{\omega_{z,88}^2}), 1\right) \tag{4.13}$$

The three components of $\vec{q}$ refer to the three ions. ω_1 is the center of mass (COM) mode frequency. ω_2 and ω_3 are the symmetric and asymmetric stretching mode frequencies. $N_i (i = 1, 2, 3)$ are the normalization factors.

It can be seen that at least one $^{88}Sr^+$ ion participates in those normal modes. Thus all those modes can be cooled via Doppler cooling of $^{88}Sr^+$. Notably, the COM mode frequency plays a vital role in our nondestructive mass spectrometry and the entire work introduced in this thesis.

The radial motions near the equilibrium position are more complicated but can still be cooled via the sympathetic cooling mechanism.

4.1.4 Field Compensation

The laser-cooled ions can be used as an indicator to implement the field compensation. Due to the existence of the stray field, the equilibrium position of the ion in an uncompensated trap is usually shifted off from the pseudopotential null, which leads to significant excess micromotion and induces several adverse effects on the trapping and spectroscopy experiments.[70] To minimize those effects, a nearly uniform static compensation field is applied to the trapping region to compensate for the stray field. In an ideal case, the pseudopotential null should coincide with the null of the static electric field. In such a condition, the ions' stable position is independent of the amplitude of the RF field, which can be verified by monitoring the ions.

In our experiment, the compensation field is applied via the compensation rod and a low-frequency rod electrode (see in figure 3.6). The two CCD cameras monitoring the ions from the side and the bottom provide 3D information on the ions' position. The ions tend to stay close to the RF null when they experience a strong RF field, while they are driven away from the null by the static field in a weaker RF field. We typically record the

position of the ion with a high RF voltage applied. And then, we lower the RF voltage and adjust the compensation voltages so that the ion returns to the recorded position. A near-perfect compensation can be achieved by repeating the previous two steps about five times. We estimate our ion's displacement from the pseudopotential null is within 8 μm, resulting in a maximum velocity of radial excess micromotion of about 10 m/s. The Doppler shift, spectral sideband, and heating rate induced by this micromotion are well below our detection limit. The compensation may be improved by monitoring the fluorescent modulation at the radio frequency.

4.2 Nondestructive Mass Spectrometry

The ability to non-destructively detect the mass of the guest ion (the ion other than $^{88}Sr^{+}$ in the ion crystal) is essential for our experiment. It enables the cryogenic ion vibrational predissociation (CIVP) method to measure the vibrational spectrum of a single molecule, where the vibration excitation is detected via the mass shift caused by the detachment of the tag. We achieve nondestructive mass spectrometry based on the precise determination of the secular frequencies of the two-species crystallized ion chain. Taking the two-ion crystals for instance, the center of mass (COM) mode frequency has a monotonic relationship with the $^{88}Sr^{+}$ axial secular frequency and the mass ratio $\mu = m_{guest}/m_{88}$ shown in equation 4.6. Once the COM frequency and the $^{88}Sr^{+}$ axial secular frequency are measured, the mass of the guest ion can be numerically calculated. In this section, I will introduce several methods we use to excite the secular motions and detect the resonance frequencies.

The key idea of this method is to read out the information via the co-trapped $^{88}Sr^{+}$ ion's fluorescence. As introduced in section 4.1.3, the ions' motions near the equilibrium positions are strongly coupled via the Coulomb interaction. When a normal mode of

the small oscillation is excited, at least one $^{88}Sr^{+}$ oscillates at that frequency. And subsequently, the spontaneous emission rate of this ion will be amplitude-modulated at the secular frequency of the normal mode due to the Doppler effect. The frequency and the amplitude of such modulation can be read out from the PMT signal (see in section 3.6).

Multiple methods have been developed to excite the secular motions and measure the secular frequency, including applying an electric field (tickle scans), optical sideband spectroscopy, ion crystal phase transition, and coherent population trapping (CPT).[71] In this work, we focus on the electric field tickle scan method with broadband chirp and single frequency signals.

4.2.1 Axial Tickle Scan

Measuring the axial COM mode frequency with chirped pulses is our primary method for performing nondestructive mass spectrometry. In traditional tickle scans, the ions are driven by single-frequency fields, and the measurement is taken at each frequency. Such a process is time-consuming and not suitable for our purpose. Instead of scanning the driving frequency slowly and observing the resonance peak, we adopt a novel method to excite secular motion via a short and broadband chirp signal and read out the resonance frequency via the Fourier transform of the fluorescence signal. It has been proved that a well-controlled broadband signal can coherently excite a narrow motion or transition. A similar technique has been adopted by K. Sheridan *et al.*, where they use a train of narrow square pulse to excite the motion.[16] The power spectrum of their square pulse signal has a sinc-shaped envelope and is not uniform. Hence, the length of the pulses needs to be adjusted for each resonance frequency to optimize the signal-to-noise ratio. Here we solve this problem by using broadband linear-frequency chirps, which have a

near-uniform power spectrum in the given frequency range.

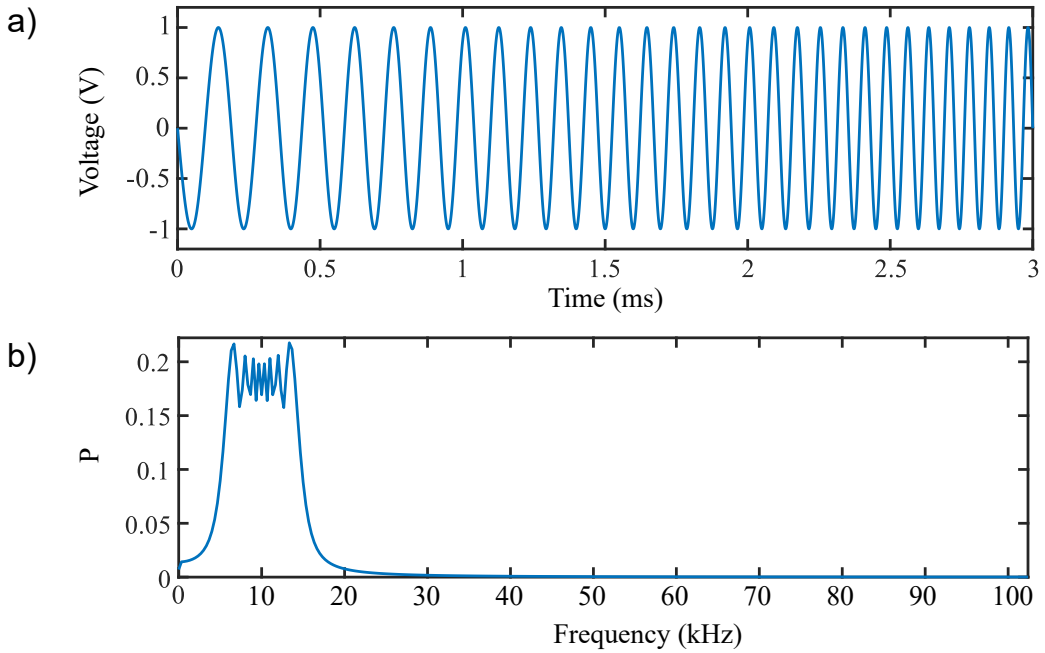

Figure 4.6: 3 ms linear-frequency chirp and its FFT amplitude spectrum. The initial and final frequencies of the chirp are 5 kHz and 15 kHz, respectively.

Figure 4.6 shows an example of linear-frequency chirped pulses. Such chirped signals can be generated by a programmed arbitrary waveform generator. These signals are widely used in the chirped-pulse Fourier transform microwave spectroscopy to coherently excite transitions in a frequency range indiscriminately.[72] They perfectly suit our purpose of exciting the collective ion motions at unknown frequencies.

To measure an ion chain's axial COM mode frequency, we generate a 3 ms long chirp pulse covering the resonance frequency with a programmed arbitrary waveform generator and couple it to the DC voltage applied to one of the end cap electrodes. The chirped pulse generates an alternating electric field along the trap axis. It drives the COM motion of the ion chain, which leads to a modulation in the $^{88}Sr^{+}$ fluorescence monitored by the PMT signal. We convert the pulsed PMT signals to 1.2 μs long pulses and record them with a spectrum card for about 7.5 ms after the start of a chirp pulse. We typically repeat

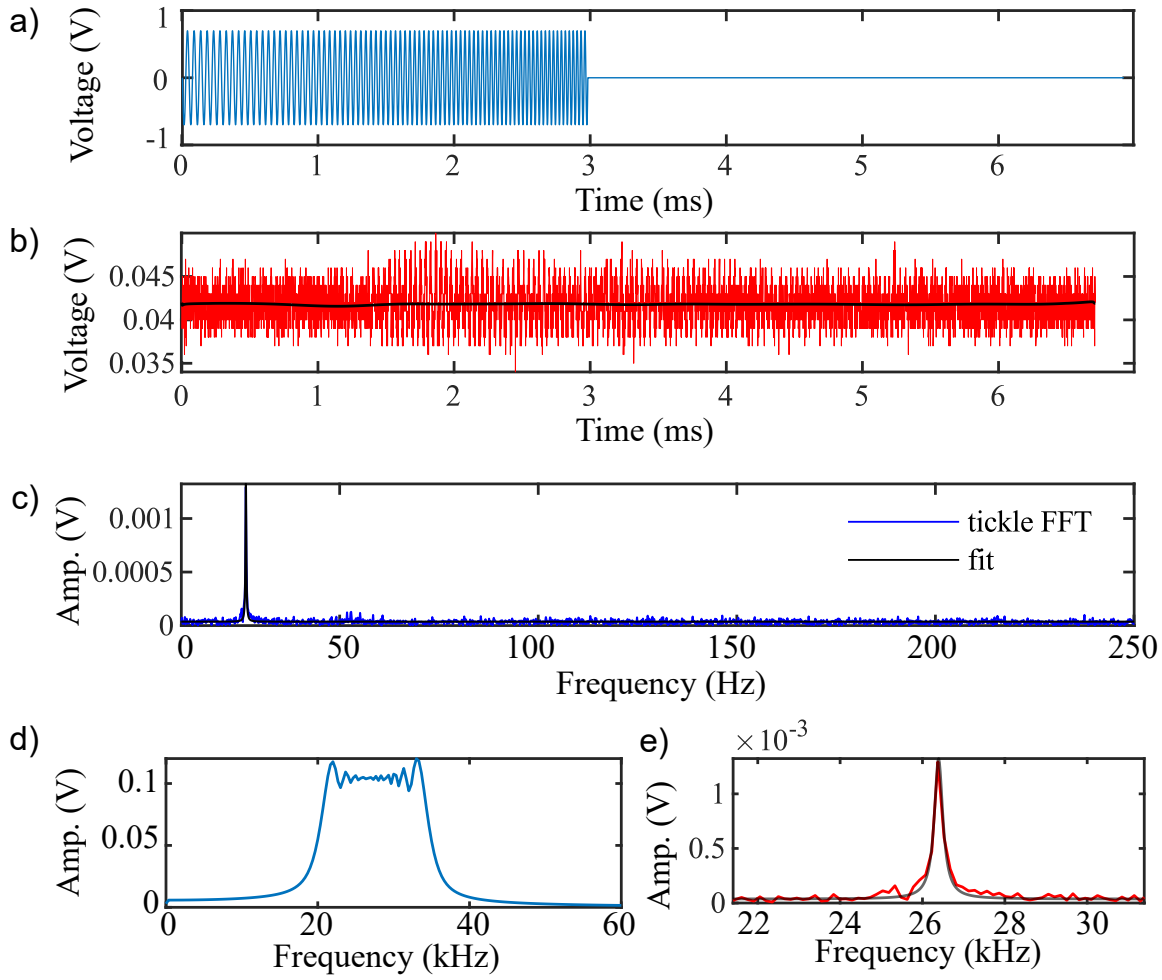

Figure 4.7: A typical result of the axial tickle scan. a) The chirped driving signal. b) The averaged PMT signal. It indicates the scattering rate of the 422 nm light by the $^{88}Sr^{+}$. The black curve shows the low-frequency component. c) The FFT output shows the FFT amplitude spectrum of the averaged PMT signal. The black curve shows the fitted Lorentzian peak. d) The FFT amplitude spectrum of the chirped driving signal. e) Zoomed-in FFT amplitude spectrum of the averaged PMT signal.

this sequence at 125 Hz (every 8 ms) 2000 times to obtain an averaged signal correlated to the beginning of the chirped pulse. Fast Fourier transform (FFT) converts the averaged signal into the single-sided amplitude spectrum. If a normal mode is excited coherently, a peak will show up in the FFT output at the resonance frequency. And usually, a 15 kHz wide chirp pulse centering the $^{88}Sr^{+}$'s axial secular frequency can robustly excite

the COM mode of the ion chains. We can fit the FFT output to a Lorentzian function and determine the resonance frequency with about 0.03 kHz accuracy. If we apply this method to a pure $^{88}Sr^{+}$ ion crystal or a single $^{88}Sr^{+}$, we can also obtain the $^{88}Sr^{+}$'s axial secular frequency. Figure 4.7 shows a typical result of our axial tickle scan, where a resonance frequency of 26.39kHz is observed. The ions' motions typically have a decay time of about 3 ms with the presence of laser cooling. Hence, the ions' motions in each period are independent and will only appear in the result if the chirped pulse coherently drives it. The maximum amplitude of oscillation during the axial tickle scan is about 30 μm, corresponding to a maximum speed of 6 m/s and a maximum Doppler shift of about 15 MHz.

In conclusion, we can measure the $^{88}Sr^{+}$'s axial secular frequency or the COM mode frequency with this method in about 30 seconds and consequently determine the guest ion's mass with one Dalton resolution.

4.2.2 Radial Tickle Scan

The chirp tickle scan method is also applied to measure the radial secular frequencies of $^{88}Sr^{+}$. The radial motions between ions in a crystallized ion chain are weakly coupled compared to the axial motions. Hence, the radial tickle scan method only works for pure $^{88}Sr^{+}$ ion chains. Even so, the radial tickle scan of $^{88}Sr^{+}$ still provides crucial information about the RF field and the trap's radial pseudopotential.

Ideally, the radial pseudopotential should be isotropic, and the two radial modes should be degenerate. Nonetheless, the two radial modes are usually found split due to the existence of asymmetric stray field and compensation field. We can adjust the splitting between the two radial modes by applying a static quadrupole field and changing the Matthieu parameter a effectively. This static field is generated by a DC voltage applied

to both low-frequency electrodes. Radial tickle scans are performed by applying the chirp signal near 200 kHz to one low-frequency electrode. The frequencies of $^{88}Sr^{+}$'s two radial modes are recorded and shown in figure 4.8.

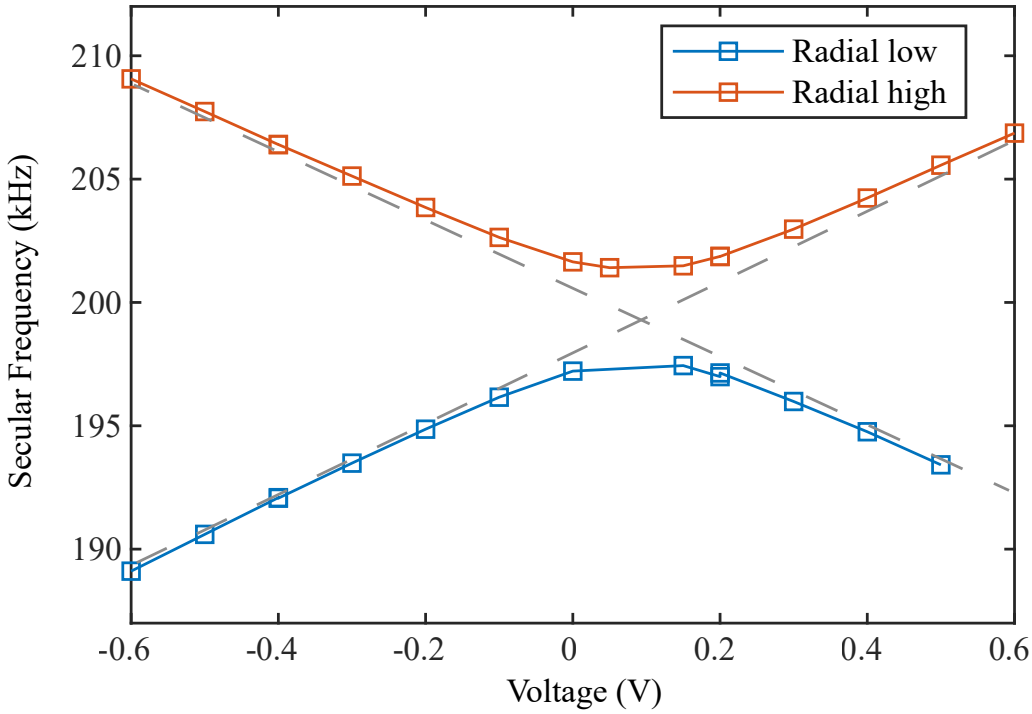

Figure 4.8: The two radial secular frequencies of $^{88}Sr^{+}$ versus the DC voltage on the two low-frequency electrodes.

The hyperbolic-shaped radial secular frequency curves can be well explained by the pseudopotential and the small oscillation model. It indicates the axes of the two normal modes are off-diagonal. In general, such a non-degeneracy won't cause problems in the experiment and actually help to achieve robust trapping and cooling. If the two radial modes degenerate, ions can steadily orbit around the trap axis, which is hard to cool.

4.2.3 Axial Constant Tickle and Lock-in Signal

Once the secular frequencies and the mass of the guest ion are determined, a constant tickle and lock-in method can be employed to monitor the mass of the guest ion. This

method can detect a significant mass shift (> 2 Dalton) of the guest ion in 1 s.

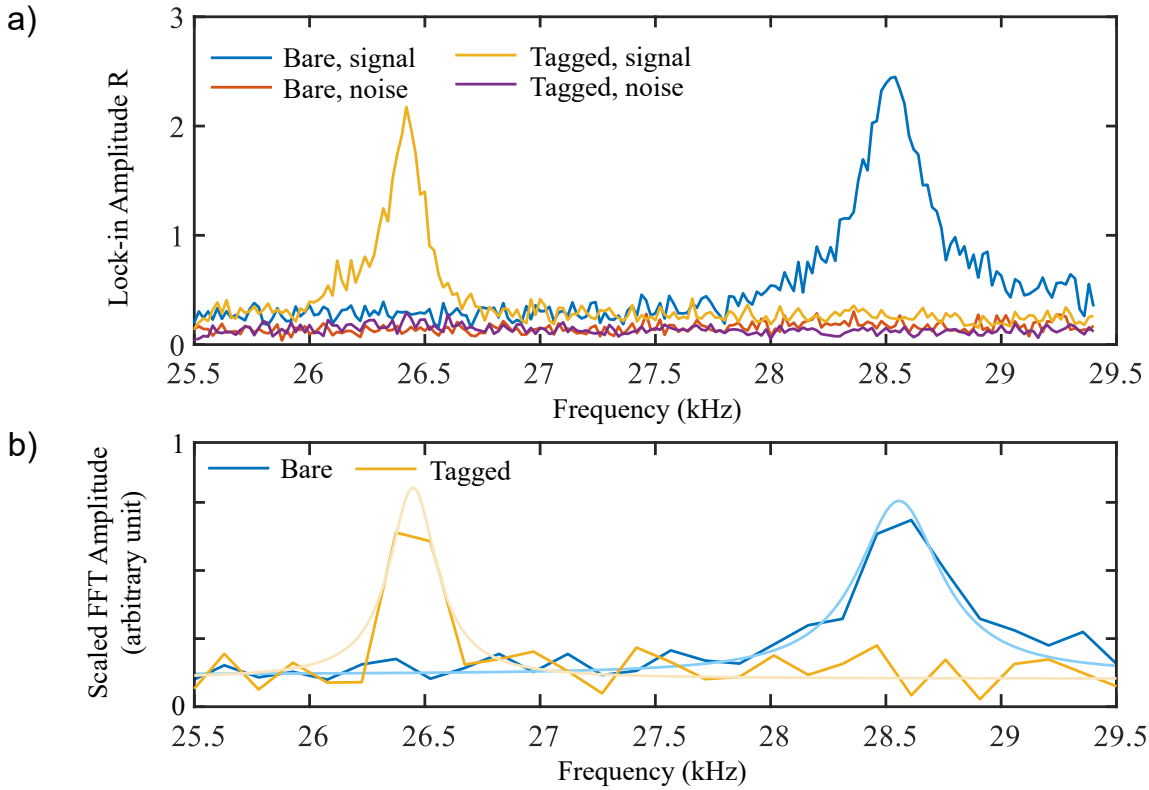

Figure 4.9: The lock-in signals and the chirped axial tickle scan results of a two-ion chain containing a bare tropylium ion and a two-ion chain including a tagged tropylium ion. a) The mean value (signal) and the standard deviation (noise) of lock-in signal amplitude versus the frequency. B) The amplitude spectra of the PMT signals obtained from the axial tickle scans. The semitransparent curves are the fitted curves.

To monitor a mass shift, an single-frequency AC drive voltage (the constant tickle, about 0.1 V) at the COM mode frequency is applied to an end cap electrode. The ion chain can be modeled as an underdamped oscillator, where the amplitude of the oscillation depends on the difference between the drive frequency and the resonance frequency. As long as the mass of the guest ion remains unchanged, the ion chain will be coherently driven by the electric field, resulting in an intensity-modulated fluorescence. The amplitude of the fluorescence modulation is rapidly extracted from the PMT signal by a lock-in amplifier every 0.5 s. The frequency dependence of the lock-in signal amplitude is shown

in figure 4.9. Two samples of two-ion chains are tested. One includes a bare tropylium ion (91 Dalton) as the guest, and the other contains a nitrogen-tagged tropylium ion (119 Dalton). The two peak positions of the lock-in signal amplitude agree well with the axial tickle scans' results, which verifies the oscillation is on resonance at the peak. The resonance peaks are about 10 times higher than the averaged noise and 5 times higher than the background. Hence, the resonance cases can be well-distinguished from the off-resonance cases based on the lock-in amplitude. The FWHM of the peak is about 0.3 kHz, corresponding to a mass shift of 4 Dalton. We typically set our threshold to $R = 1$ to monitor any event making the ion chain go off-resonance. Such an event usually indicates a mass shift of the guest ion. It could be caused by tagging, de-tagging, chemical reactions, and fragmentation. In our experiments, this technique is heavily employed to monitor the photon-induced de-tagging events.

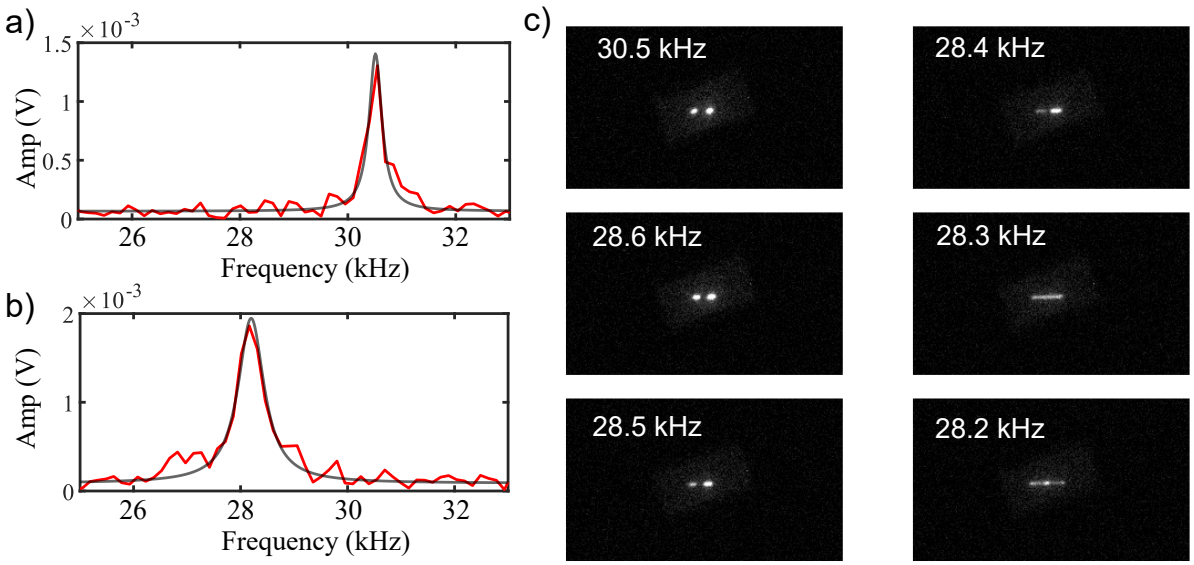

Figure 4.10: a)The axial tickle scan result of the bare guest ion. b)The axial tickle scan result of the tagged guest ion. c) The long-exposure images of the two-ion chain containing the tagged guest at different constant tickle frequencies.

The camera images assist in the detection of mass-shift events. When the constant tickle is applied, the oscillation can also be observed in the camera images. Figure

4.10 shows the photos of a two-ion chain at different constant tickle frequencies. The guest ion in the ion chain is tagged with a nitrogen molecule, which shifts the resonance frequency from the bare guest's 30.51 kHz to 28.20 kHz. When the constant tickle is at the bare guest's resonance frequency, the ion chain barely responds to the constant tickle. However, as the frequency gets closer to the true resonance frequency, the ions' image gets wider and wider. And the width finally peaks at the resonance frequency. Sometimes, the lock-in signal drops due to a high-energy collision, where the camera image can help to rapidly distinguish it from a mass shift event.

4.2.4 Radial Constant Tickle

Radial single-frequency constant tickle excites the on-resonance ion species radially. When a radial mode is excited, the ions are usually far from equilibrium geometry. The excited ions are no longer strongly coupled to the others during the oscillations. The resonance frequency of each ion is its own radial secular frequency in the RF field. For a guest ion with a known mass, the radial secular frequency can be calculated based on its mass and the $^{88}Sr^{+}$'s radial secular frequencies,

$$\omega_{r,m} = \frac{QV\alpha'}{\sqrt{2}m\Omega_{rf}} = \frac{m_{88}}{m}\omega_{r,88} \tag{4.14}$$

One main application of the radial constant tickle is selectively removing ions from the trap based on their masses. Unnecessary ions are sometimes loaded accidentally. A violent constant tickle with an amplitude of 1 V for 2 s can robustly shake out the ion at the target mass. However, it may affect ions within 5 Dalton from the target mass. A relatively mild constant tickle at 0.16 V can more selectively remove ions but is less robust. It is usually used if the trapped ions have similar masses.

Ideally, the driving frequency should change as the target ion gets to a high orbit due

to the anharmonic pseudopotential. (See in section 3.2.3.) However, the ion's trajectory can hardly be precisely controlled or predicted due to the random collisions with background gas and Coulomb interaction with other ions. It is found that a single-frequency constant tickle works better than other complicated signals designed based on the model of a single ion moving in the pseudopotential.

If the amplitude of the radial constant tickle is between 0.02 and 0.1 V, the ions at the target mass will be excited to a high orbit but stay in the trap. This method temporarily removes an ion species from the ion chain so the rest ion chain can be studied undisturbedly. For instance, the $^{88}Sr^{+}$'s axial secular frequency can be verified by driving the guest ion in a two-ion chain to high orbits. Such radial constant tickles are also useful for determining ions' mass when multiple guest ions are trapped. Moreover, the low-amplitude radial constant tickle can be used to induce high-energy collisions and controllably heat the internal degrees of freedom of a molecular ion.

4.3 Preparing the Complex

Preparing the molecular ion–tag van der Waals complex is another essential technique of our single-molecule CIVP spectroscopy. The complex is produced by tagging a bare molecular ion with N_2 using a 5:1 mixture gas pulse of He:N_2. The van der Waals bonds are sensitive to the internal vibrations of the molecular ion. Once a vibrational mode higher than the binding energy is excited, the complex will undergo an intramolecular vibrational energy redistribution (IVR) process and dissociate within 0.1 ns.[73] Detecting such dissociation enables CIVP spectroscopy. Taking a vibrational spectrum with a single molecular ion requires hundreds of repetitions of measurements before the ion is lost due to reactive collisions with the background gas. Hence, we have to find a time-efficient and robust tagging recipe.

The nitrogen molecule is a non-polar and chemically inert neutral particle. Such a particle has no permanent electric dipole moment. But in the electric field, the displacement of the charges can induce a temporary dipole moment. The induced dipole moment is proportional to the electric field intensity and the polarizability of the particle,

$$\vec{p} = \alpha \vec{E} \tag{4.15}$$

Here, if the particle is isotropic, polarizability α is a scalar. Otherwise, α should be a tensor. The potential of the particle in an electric field will be

$$V = -\vec{E} \cdot \vec{p} = -\vec{E} \cdot (\alpha \vec{E}) \tag{4.16}$$

The strong electric field near a charged ion can induce a dipole moment in the neutral non-polar particle, causing an attractive ion-induced dipole interaction. This interaction can bind the particle to the ion with a binding energy ranging between 50 and 1000 cm^{-1} when the induced attractive force reaches equilibrium with the repulsive interaction.[74] We call such a bounded particle a tag to the ion. The binding energy depends on the ion species, the tag particle's volume, and the number of electrons. In general, the binding energy tends to be larger if the tag particle is larger and contains more electrons. If the particle is not isotropic, the principal axis of it, along which the polarizability is the largest, will tend to align with the electric field direction.

Three-body collisions are needed to initially form the ion-tag complex in the gas phase. Figure 4.11 illustrates the tagging process. Due to the energy and momentum conservation law, the excess energy need to be dissipated before a free tag particle can be bounded to a bare ion. In two-body ion-neutral collisions, the interaction time scale is usually around picoseconds, which is too short for a spontaneous emission to take

place. A third body must participate in the interaction and take away the redundant energy. Once the ion is tagged, replacing or forming additional tags may no longer need three-body collisions.

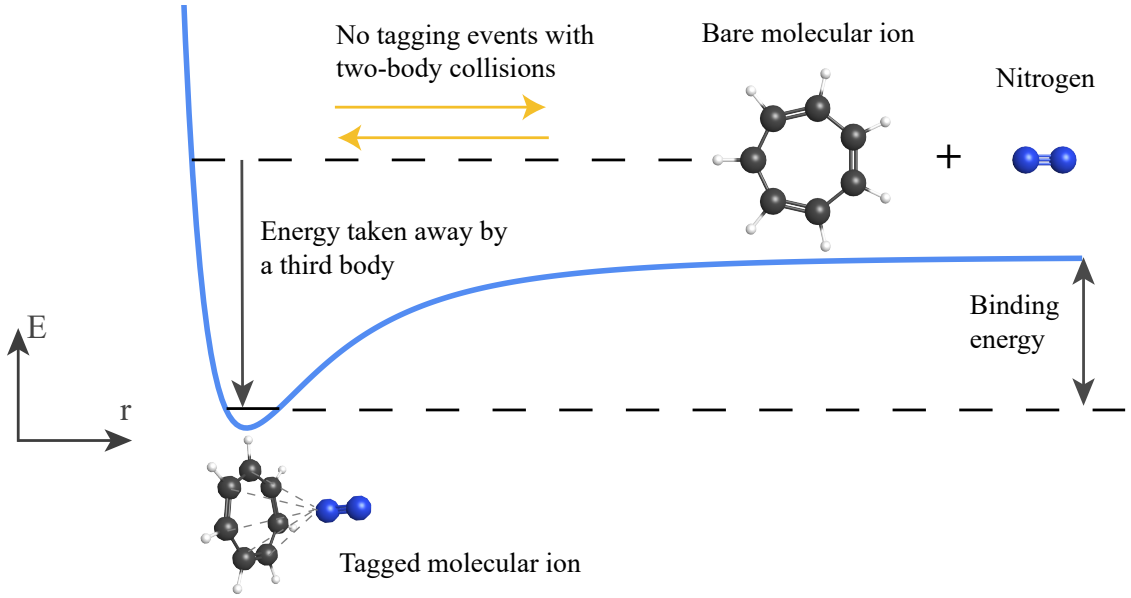

Figure 4.11: The tagging scheme.

An intensive gas pulse is ejected to the ion-trapping region via the buffer gas line to achieve a sufficient three-body collision rate. The primary constituent of the gas pulse is usually helium. We typically use a 5:1 mixture of He:N_2, where helium serves as the carrier gas and the collision partner. The pulse valve in the mixture gas line is driven by an IOTA ONE® driving system, which enables gas pulses as short as 500 μs with our system. We typically set the pulse duration between 2 ms and 4 ms. With a 3 ms gas pulse, we observe a peak pressure near the main chamber between 10^{-4} and 10^{-5} Torr. Helium can remain a high pressure in the cryogenic environment and induce sufficient collisions. The helium flow helps the nitrogen gas pass through the buffer gas tube around 14 K, cools the nitrogen gas, and prevents nitrogen from freezing to the cryogenic surface. Moreover, using helium as the third collision body helps to control the

tagging events during one gas pulse. The high collision rate between the ion and helium guarantees a high possibility of nitrogen-participated three-body collisions during a gas pulse with limited nitrogen pressure. In general, it is nearly impossible to achieve such a tag efficiency without helium at cryogenic temperatures. At the same time, the small proportion of nitrogen also limited the total number of collisions that N_2 participates in, which reduces the possibility of forming multiple tags (over-tagging) during one gas pulse. The nondestructive mass spectrometry method is employed to verify the number of tags and the tags' species.

In the traditional multi-ion CIVP experiments, ions are rapidly tagged, shuttled to the experimental region, and de-tagged within 0.1 s. They have employed numerous tagging species, including N_2, H_2, D_2, helium, neon, and Argon.[75, 76] Some of them can cause less disturbance to the ion and achieve less disturbed vibrational spectra than that with a nitrogen tag. However, the time scale of a single measurement in our experiment is much longer. The tagging procedure takes at least 10 seconds to pump the gas pulse out, and the measurement takes an additional one or a few minutes. We have tried using neon and hydrogen as the tag particles and experimentally observed those tags in our system. But none of them have a long enough lifetime for our measurement. Those tags have lower binding energies and are usually tripped off during collisions or substituted by background nitrogen within minutes. Figure 4.12 shows several de-tagging events of neon tags during axial tickle scans—the different masses before and after the de-tagging result in separated resonance peaks. The lifetime of neon tags is estimated to be around 20 s. On the contrary, the nitrogen tags can stay for a few hours at least. Hence, nitrogen is chosen to be our tagging partner.

Some tricks can be adopted to enhance the tagging rate. Nitrogen gas can hardly survive at the cryogenic temperature and sometimes can not involve in enough three-body collisions to tag the ion. In this case, we can first tag the ion with a H_2, then let

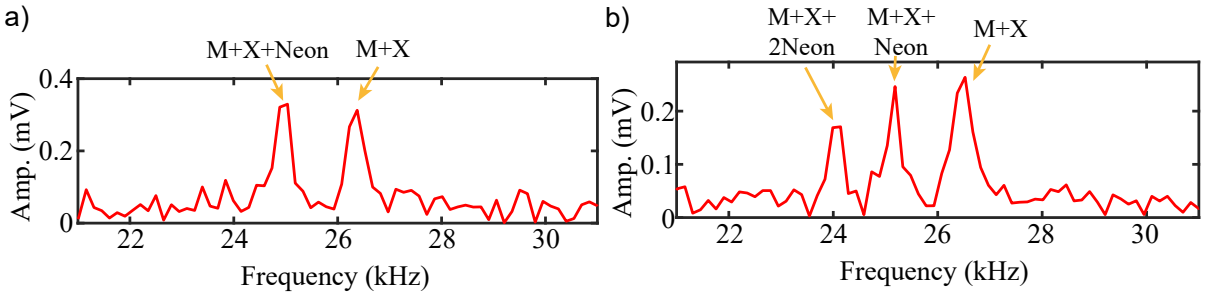

Figure 4.12: Axial tickle scan results where the dissociation events of neon tags are observed. M refers to the bare ion, and X refers to some unknown tags.

an N_2 substitute it during a two-body collision, which requires less nitrogen pressure and collision events. Even the background H_2 density may induce more tagging events than the N_2 in a mixture pulse. The small mass of H_2 results in a lower pumping efficiency via the mechanical pumps and a high average speed at low temperatures, which allows H_2 molecule to participate in more collisions with the ion. The polarizability of N_2 is more than two times larger than that of H_2.[77] The binding energies of the two tag species, which are proportional to the polarizabilities, have a similar relationship. As a result, a collision between one or two-H_2 tagged ion and a N_2 will likely generate a single N_2 tagged ion and free H_2 molecules. We find this procedure works robustly and is non-reversible. This pathway to single N_2 tagged ion increases the tagging efficiency and helps achieve better control of the number of tags. We also accidentally discovered that neon pulses can temporarily increase the hydrogen density in our system either by the H_2 impurity or the heating of the environment. So we typically fire a weak 7.5 ms neon pulse, where the pulse valve is driven by a homemade controller and is barely opened in 7.5 ms, two seconds before the He-N_2 mixture to enhance the H_2 tags-substitution pathway. We can achieve a successful tagging efficiency of about 40% for general molecular ions and even higher in some cases, like a 121-Dalton ion fragment of 1,3-Benzodioxole. The difference is related to the ion structure and is probably caused by the difference in the binding energies.

Chapter 5

Chapter 5 Single Molecule Vibrational Spectroscopy

This chapter introduces the single molecule vibrational (infrared) spectroscopy method and our experimental results. Employing the previously introduced experimental setups and techniques, we achieve a general spectroscopic method to analyze a single gas phase molecular ion. It allows us to study the purest possible molecular samples in the world, one single isomer at a time. We demonstrate this method by measuring the vibrational spectrum of a single tropylium ($C_7H_7^+$) molecular ion, the first recorded spectrum of a single gas phase polyatomic molecule to our knowledge. I will also introduce the studies toward the frequency resolution limit of this method and the rotational branch-resolved vibrational spectrum of a single tropylium ion. At last, I will demonstrate that this method is generalizable to a broad class of polyatomic molecules.

5.1 Method

This section introduces the experimental scheme of the single molecule vibrational spectroscopy and the data analysis method.

The first step of the experiment is preparing the two-ion crystal consisting of a $^{88}Sr^{+}$ and a guest molecular ion. The single $^{88}Sr^{+}$ ion is first loaded into the cryogenic linear Paul trap and Doppler-cooled to milliKelvin temperatures. A standard axial tickle scan with chirped pulses determines the axial secular frequency of the $^{88}Sr^{+}$. Then a single molecular ion is produced, mass-selected, and loaded into the ion trap. The co-trapped $^{88}Sr^{+}$ atomic ion sympathetically cools the molecule to milliKelvin translational temperatures. The formation of the two-ion crystal is confirmed with the camera images, and the mass of the molecular ion is verified by another axial tickle scan based on the formula 4.6.

Once the two-ion crystal is ready, we can start the single molecule vibrational spectrum measurements. Each measurement sequence gives one data point of the de-tagging time at a single infrared frequency. We typically keep repeating the measurement sequence at different frequencies until the ions are lost due to reactive collisions. The obtained data points are later analyzed to deduct the vibrational spectrum of the single molecule.

The measurement sequence includes two steps, tagging and de-tagging. The molecular ion is firstly tagged by a N_2 molecule with He-N_2 mixture gas pulses, forming the ion-tag complex.(Tagging details are discussed in section 4.3.) It is then de-tagged with mid-IR light from a commercial optical parametric oscillator, during which the total mid-IR light exposure time before the de-tagging event is counted. In this process, if the mid-IR light resonantly drives a vibrational transition of the molecular ion, the complex will absorb the mid-IR photon efficiently. Once the photon is absorbed, the energy in the excited

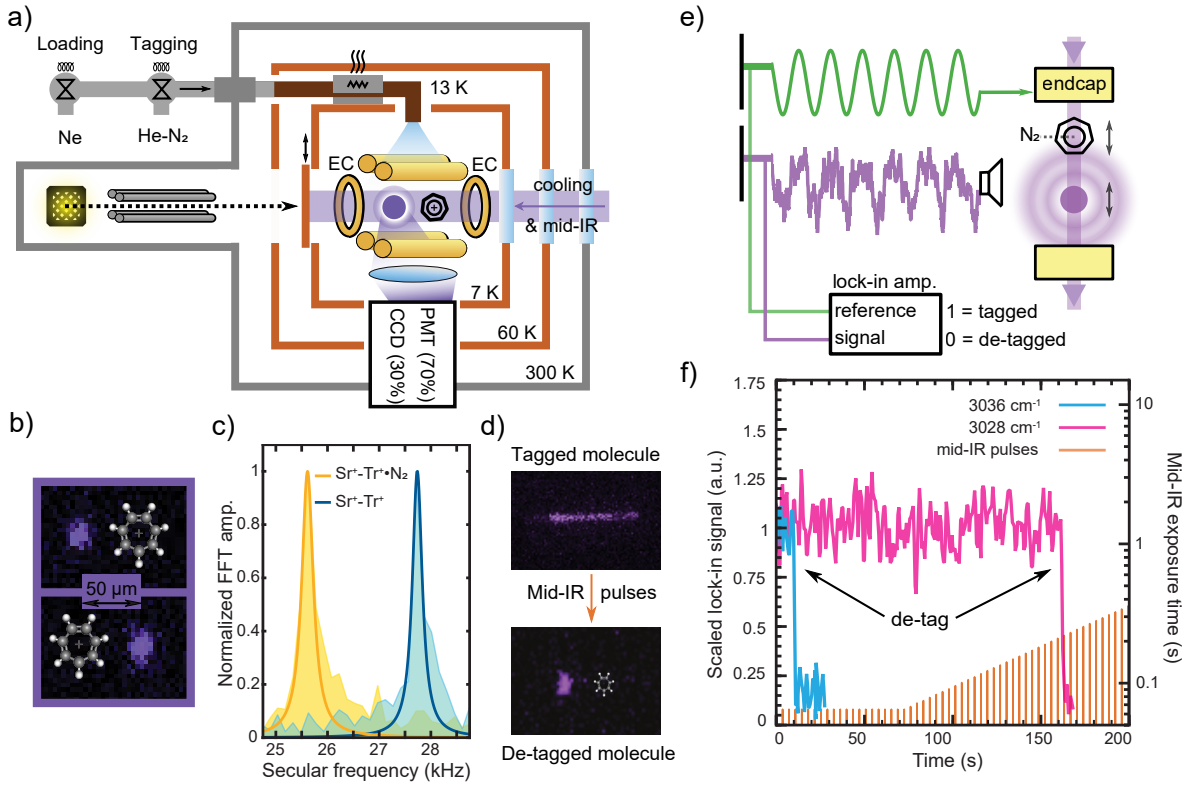

Figure 5.1: Experimental scheme and results. The molecular ion is represented by the tropylium ion(Tr^+). a) A schematic diagram of the experimental setup. b) Two images verifies the forming of $^{88}Sr^+$-Tr^+ crystal. c) Axial tickle scans verify the tagging status. The presence of the N_2 tags shifts the axial frequency by a few kHz. d) A de-tagging event observed with images of the two-ion crystal driven at the tagged frequency. e) The constant AC drive voltage, the PMT signal, and the lock-in signal. The drive voltage is on resonant with the $^{88}Sr^+$-Tr^+·N_2 COM mode. A lock-in amplifier compares the PMT signal (purple) with the AC drive, producing a near-unity voltage when the ion is tagged, and near-zero when not. f) The de-tagging events during the exposure sequence monitored by the lock-in amplitude. Fast (blue) and slow (pink) de-tagging events of Tr^+·N_2 at different frequencies are shown.

vibrational mode will be redistributed within a nanosecond and causes the dissociation of the complex. If the mid-IR frequency is off from all the IR-active vibrational transitions, the complex rarely absorbs a photon and will have a long lifetime. Hence, the total mid-IR light exposure time before the de-tagging is directly related to the vibrational transition strength of the molecular ion at the mid-IR frequency and is used to deduct the vibrational spectrum.

The lock-in signal is widely used in the tagging and de-tagging process. The mass of the bare and the N_2-tagged molecular ion is known. Thus, the status of the molecular ion can be rapidly determined based on the lock-in signal and the resonance frequency. Once the molecular ion is tagged with a single N_2, we drive the two-ion crystal's COM mode and monitor the presence of the tag via the lock-in signal amplitude. We typically wait for about 10 s before sending in the mid-IR light, allowing the vacuum to settle and the internal degrees of the molecular-ion tag complex to be cooled by the collision with the background gas. If the background collision rate is not high enough after the forming of the complex, we will eject a short neon buffer gas pulse to ensure the thermalization of the internal degrees to the inner shield temperature. The complex is now ready for vibration-induced dissociation (de-tagging).

As the de-tagging procedure starts, mid-IR light pulses are sent to the ions, co-aligned with the axial cooling laser. The quasi-continuous mid-IR light is gated via a mechanical shutter controlled by a computer, forming a sequence of light pulses. The pulses are separated by about 2.5 seconds, allowing the lock-in signal to respond to the possible de-tagging event. The resonant de-tagging causes the change of the resonance frequency, represented by a sudden drop in the lock-in amplitude. It can also be verified based on the images of the ions. Once a de-tagging event is observed, the mid-IR pulse, during which the complex de-tags, is determined based on the lock-in signal. The upper and lower limit of the total exposure time is then determined. The mid-IR light pulses will stop if no de-tagging event is observed in a total exposure of 90 seconds, which gives a baseline of the de-tagging rate and our vibrational spectra. In comparison, the highest de-tagging rate we observed is above 10 Hz. This wide dynamic range makes weak transitions with lifetimes of many seconds easily observable. Notably, in usual cases, the lifetime of the molecular ion-tag complex is several hours in the absence of mid-IR laser light. It indicates a near-zero background de-tagging rate on our experiment's timescale,

which guarantees the reliability of the measurement to the mid-IR-induced de-tagging rates and a low-noise background. It allows us to clearly distinguish the weak spectral features invisible to most other methods.

Each of the measurement sequences takes about a few minutes. The process is mainly controlled, monitored, recorded, and auto-analyzed via a Matlab GUI I built.

5.1.1 Theoretical Model of the De-tagging Time

In the de-tagging process, the tagged nitrogen constantly monitors the vibrational state of the molecular ion. Once a ro-vibrational transition is driven and a vibrational mode is excited, a de-tagging event occurs at the picosecond level. Such a process is non-reversible and causes quantum decoherence. The time required for a de-tagging event, T, can be modeled as a random variable following an exponential distribution in several simplified scenarios.

One scenario is that vibrational transitions of the molecular ion-tag complex are coherently driven by a continuous wave (CW) mid-IR light far below the saturation intensity. The period of the induced Rabi oscillation is much longer than the decoherence time scale. The quantum dynamic of this process is similar to the quantum jumps, where the distribution of the time required for a transition is exponential.[78, 79] The distribution is characterized by a time constant, which corresponds to the average de-tagging time in our case. This time constant is inversely proportional to the intensity of the mid-IR light and vibrational spectrum function.

Another scenario is that the vibrational transitions are driven by a stable pulsed mid-IR laser with a high repetition rate and low de-tagging possibility per pulse. For instance, our Firefly IR laser has a repetition rate of 150 kHz. The status of the molecular ion after a pulse is detected by the tag in picoseconds. The ion will either stay tagged at the

vibrational ground state or become de-tagged after a vibrational transition. At a given mid-IR laser frequency, ω_L, the probability that a tagged molecule de-tags during a laser pulse is a constant. As a result, the probability that the de-tagging event happens right after a sequence of pulses is exponentially decreasing in the number of pulses. Since the total exposure time before de-tagging T is proportional to the total number of exposure pulses, T is an exponentially distributed random variable.

In both scenarios, the complex is assumed to be at a single rotational state or have a stable rotational distribution, which may not be proper experimentally. We rely on buffer gas cooling to keep the rotational degrees at the inner radiation shield temperatures. The rotational quantum number J can reach above 20 depending on the rotational constant of the complex. The rotational quantum number J is changing due to collisions. In principle, the allowed ro-vibrational transitions and their frequencies depend on the inial rotational state of the molecule (the vibrational mode is frozen at the cryogenic temperatures). We typically assume the constantly changing rotational state has a stable averaged effect, allowing us to interpret our spectra similarly to the spectra of a thermalized ensemble. But it should be carefully evaluated according to the specific circumstances and verified experimentally. It is less of a problem when the laser is broader than the vibrational band. In this case, the transitions from different initial states are all driven by the laser, which is typically true when the 6 cm^{-1} wide Firefly laser is used.

In general, we assume the observed total exposure time before the de-tagging event T follows an exponential distribution. The probability density function of the distribution is characterized by the wavelength-dependent exponential time constant $\tau(\omega_L)$, which can be expressed as,

$$p(T|\tau(\omega_L)) = \frac{1}{\tau(\omega_L)} e^{\frac{-T}{\tau(\omega_L)}} \tag{5.1}$$

Our measurement results are random samplings of this distribution. And the time

constant $\tau(\omega_L)$, which is inversely proportional to the spectrum function, can be estimated via the maximum *a posteriori* estimation or the maximum likelihood estimation. (See in subsection 5.1.3) At last, we obtain the vibrational spectrum of the molecule represented by $\frac{1}{\tau(\omega_L)}$.

5.1.2 Exposure Sequence Designs

Upon exposure to mid-IR light, de-tagging occurs on a timescale faster than the detection time for our mass measurement methods. In order to extract a meaningful rate, the mid-IR laser is gated via a mechanical shutter into a sequence of exposures. The intervals between exposures allow the PMT to respond to the possible signal drop caused by a de-tagging event. When a de-tagging event is observed, the start time, T_s is defined as the total exposure time before the final de-tagging pulse. The final time, T_f, is taken as the total exposure time counting the final pulse, with the de-tagging event occurring sometime between these two times. And the time resolution is set by the final pulse's duration. Given the probability distribution 5.1, the probability of observing a de-tagging event between T_s and T_f is

$$P(T_s, T_f|\tau(\omega_L)) = e^{-\frac{T_s}{\tau(\omega_L)}} - e^{-\frac{T_f}{\tau(\omega_L)}} \tag{5.2}$$

Suppose that we want to achieve a higher time resolution. Each exposure pulse needs to be shorter. As a result, the possibility of a de-tagging event during an exposure pulse will be smaller. And it will take a much longer experimental time to reach the same total exposure time due to the limitation of the relatively long mass detection time. To balance the time efficiency and the performance of the de-tagging time measurement, a special exposure sequence is designed.

Our mechanical shutter can produce exposure pulses ranging from 65 ms to infinity.

And we can have at most about 100 exposure pulses in a reasonable experimental time. A straightforward sequence design is to set all the pulses to an equal length. However, none of these sequences can work robustly for a broad range of time constant τ. When measuring a vibrational spectrum, $\tau(\omega_L)$ varies dramatically at different frequencies and is unknown in previous. If $\tau(\omega_L)$ is much smaller than the single pulse duration, most de-tagging events will occur during the first pulse. If $\tau(\omega_L)$ is much longer than the single pulse duration, we will likely observe no de-tagging events in 100 pulses. In both cases, limited information can be obtained within a few measurements. Two examples, where the pulse duration is set to 65 ms and 650 ms, respectively, are shown in figure 5.2. Taking measurement with either of them only has enough sensitivity to the time constant τ in a narrow range.

This problem is solved by keeping a constant step of the total exposure time in a logarithmic scale rather than in a linear scale. As discussed above, the de-tagging probability in a constant time interval strongly depends on the time constant. The shape of the probability density also varies a lot, which makes it hard to random sample and extract the time constant from the data. However, viewing in logarithmic scale, the probability density of the random variable $\ln T$ follows,

$$p'(\ln T|\tau) = p(T|\tau)\frac{\mathrm{d}T}{\mathrm{d}\ln T} = e^{\ln T - \ln \tau} e^{-e^{\ln T - \ln \tau}} \tag{5.3}$$

The shape of this probability density function is independent of the time constant τ. And a peak always shows up at the $\ln T = \ln \tau$. A comparison of the two types of distributions is shown in figure 5.3. If we randomly sample the distribution of $\ln T$ with a constant step comparable to the peak width, we can easily cover the major part of the distribution for τ in a large range. The de-tagging probability during each pulse will also be more equally distributed in most cases. In other words, all the pulses and detection times are

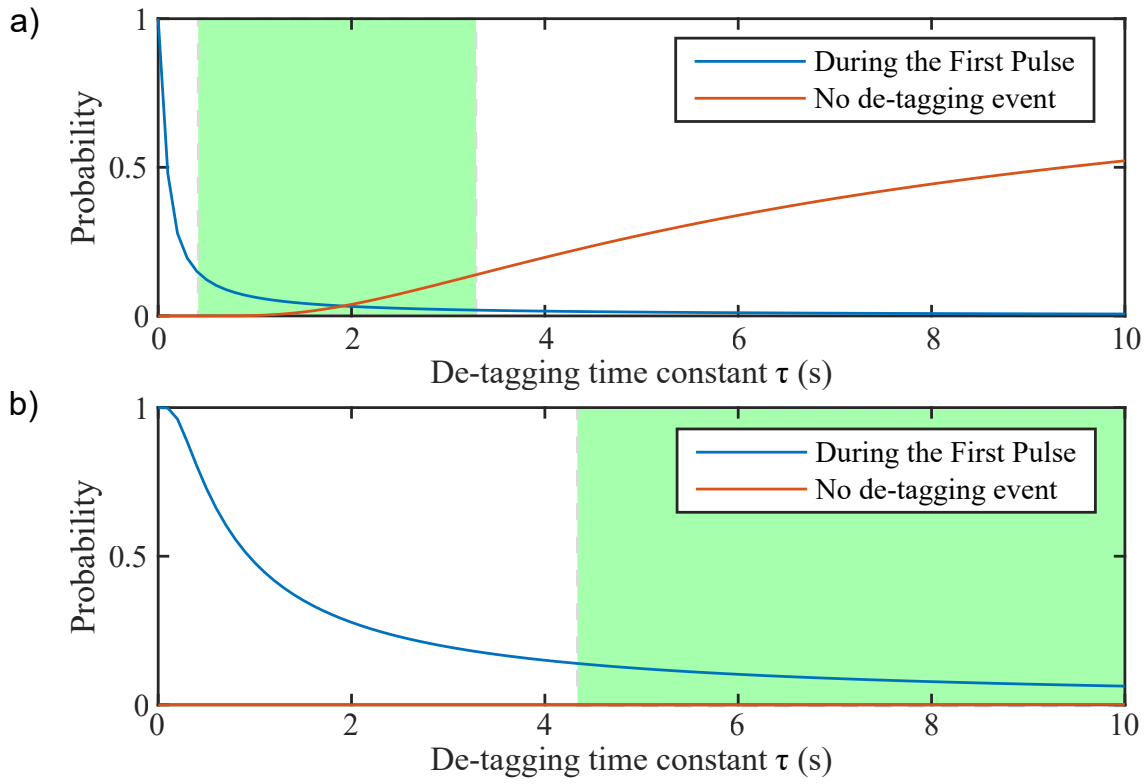

Figure 5.2: The probability of de-tagging during the first pulse and no de-tagging in 100 pulses. The green color marks the time constant range where the exposure sequence can provide enough sensitivity to resolve the de-tagging time constant. a) Single pulse duration = 0.065 s. b) Single pulse duration = 0.65 s.

more efficiently used. We can realize such kind of sampling by keeping the pulse duration proportional to the total exposure time, which leads to an exponential growth of the total exposure time as a function of the number of pulses. It effectively keeps a constant step $\Delta \ln T$. We typically set this step to $\ln(1.05)$.

There is another way to understand such a design. At each given frequency ω_L, there is a unknown but fixed de-tagging time constant $\tau(\omega_L)$. If no de-taggging is observed in n pulses, we already get some information about $\tau(\omega_L)$ related to the total exposure time. As the total exposure time increase, it indicates the possibility for de-tagging in each pulse is small. And it is fair to increase to the pulse duration based on the total duration before that pulse.

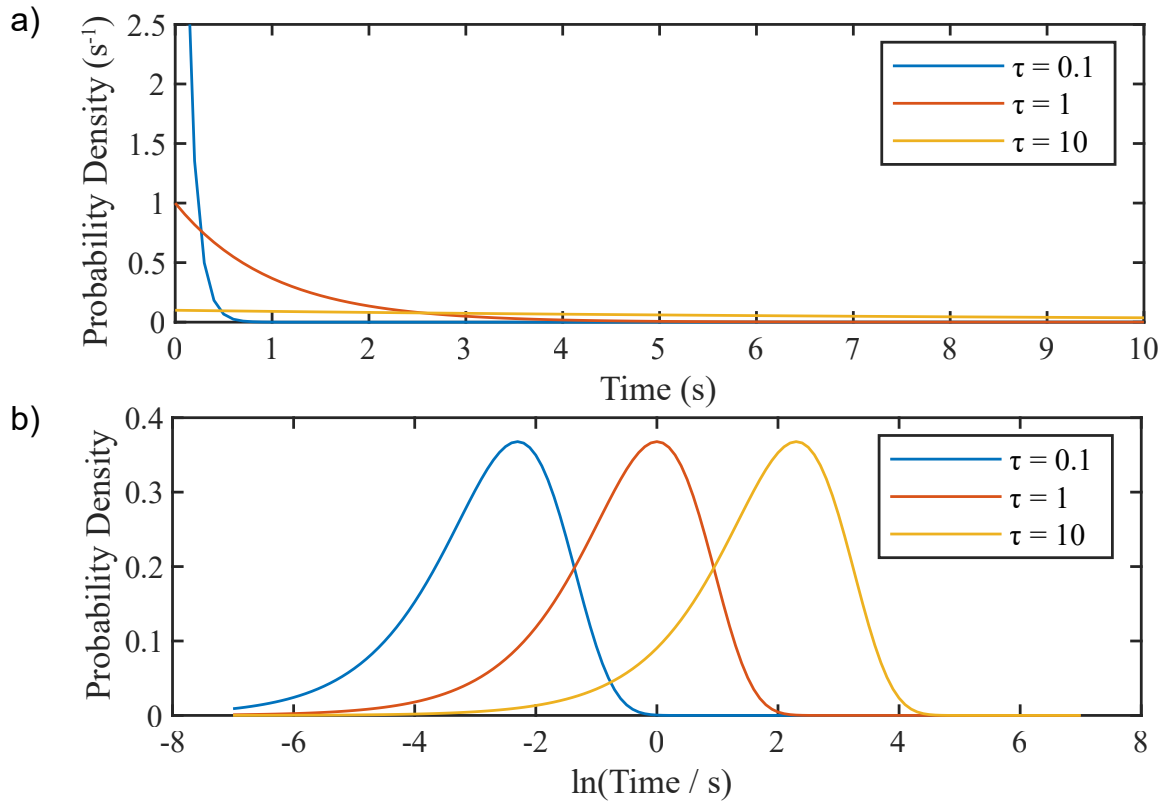

Figure 5.3: The probability density functions when $\tau = 0.1, 1, 10$. a) The probability density functions of T. b) The probability density functions of $\ln T$.

We typically set the first 20 pulses to 65 ms, the minimum duration our mechanical shutter can produce. The following pulses' lengths are set to 1/20 of the sum of the previous pulse length until it goes above 1.5 s. The last 40 pulses are fixed to the maximum pulse duration of around 1.5 s. The whole pulse sequence is illustrated in figure 5.4. This pulse sequence provides the best possible resolution of 65 ms for fast de-tagging events and a stable relative resolution below 5% for slow de-tagging events. And it allows us to reach the maximum exposure time of 90 s in about 300 seconds.

5.1.3 Data Analysis Method

We typically take at least three data points at each frequency and use a maximum likelihood estimation method to determine the time constant and the spectral strength.

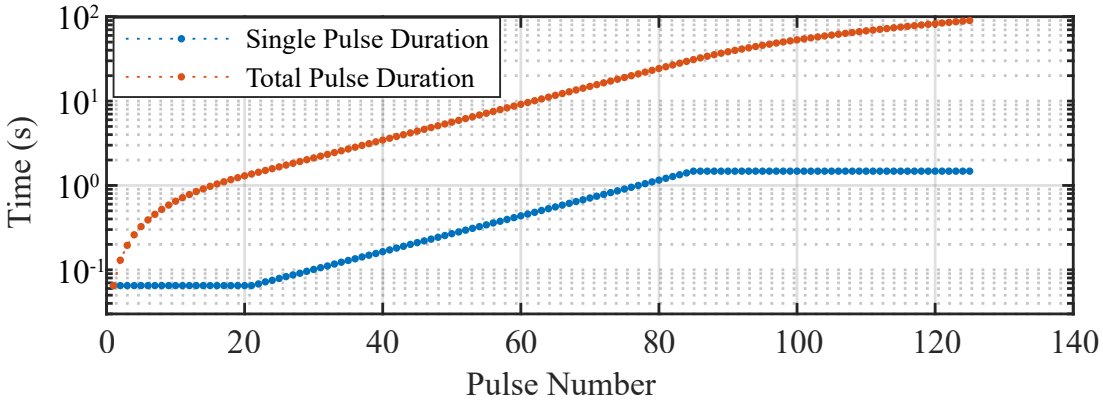

Figure 5.4: The exposure sequence. The single pulse duration and the total exposure time after the pulse are shown as functions of the pulse number.

The details of this method are discussed in this subsection.

Each de-tagging measurement gives two numbers, the lower limit of the exposure time before the de-tagging T_s and the upper limit T_f. The de-tagging event occurs sometime between these two times. The probability of observing a de-tagging event between T_s and T_f follows 5.2. For N measurements per point, this becomes,

$$P(T_i|\tau(\omega_L)) = \prod_{i=1}^{N} \left[e^{-\frac{T_{s,i}}{\tau(\omega_L)}} - e^{-\frac{T_{f,i}}{\tau(\omega_L)}} \right] \tag{5.4}$$

Assuming that the prior probability of $\ln(\tau(\omega_L))$ is uniformly distributed, the maximum *a posteriori* estimation or the maximum likelihood estimation of the distribution parameter $\tau(\omega_L)$ is achieved by maximizing the likelihood function $L_N(\tau(\omega_L)|T_i) = P(T_i|\tau(\omega_L))$ with respect to $\tau(\omega_L)$. We maximize this function numerically to determine this most likely value for $\tau(\omega_L)$. We also determine a 95% confidence level numerically based on the distribution of the likelihood functions. The density of the confidence level is proportional to the posterior probability density, and we have,

$$CL(CI_{min} < \tau < CI_{max}) \equiv \frac{\int_{\tau=CI_{min}}^{\tau=CI_{max}} L_N(\tau|T_i)\, \mathrm{d}\ln(\tau)}{\int_{\tau=0}^{\tau=+\infty} L_N(\tau|T_i)\, \mathrm{d}\ln(\tau)} \tag{5.5}$$

We choose the interval where the likelihood function $L_N(\tau(\omega_L)|T_i) > e^{-2} \cdot L_{N,max}$ as our confidence interval, and verify that this corresponds to a confidence level of $\gtrsim 95\%$. This gives the smallest possible 95% confidence interval respective to $\ln(\tau(\omega_L))$.

From the point of view of random sampling, our method of data analysis can be well justified when ignoring the slight broadening and distortion of the likelihood function due to the uncertainty caused by the finite exposure time from our shuttered laser source. Assuming the observations T_i constitute N random samples subjected to an exponential distribution with the time constant τ_0, and $dT_i \equiv T_{f,i} - T_{s,i} \ll \tau_0$ for all i, we have,

$$L_N(\tau|T_i) = \prod_{i=1}^{N} \left[\frac{dT_i}{\tau} e^{-\frac{T_i}{\tau}} \right] \tag{5.6}$$

The likelihood function reaches the maximum when $\tau = \frac{\sum_{i=1}^{N} T_i}{N}$, which gives an unbiased estimator of τ_0. (For exponential distribution, the expected value of T always equals τ.) Notably, the likelihood function L_N can be normalized by a factor $(\frac{\sum_{i=1}^{N} T_i}{N})^N \cdot \frac{1}{\prod_{i=1}^{N} dT_i}$ to give a function only of the number of samples N and the relative magnitude of τ and $\frac{\sum_{i=1}^{N} T_i}{N}$. This indicates that for a given N, the likelihood function L_N is always proportional to a fixed function $\ln\left(\frac{N\tau}{\sum_{i=1}^{N} T_i}\right)$. This is similar to the cases of using random sampling to determine the expected value of a normally distributed random variable with fixed standard deviation, but only when viewed in a log scale rather than in a linear scale. For any $v > u > 0$, if we choose the confidence interval to be $CI = (u \cdot \frac{\sum T_i}{N}, v \cdot \frac{\sum T_i}{N})$, the confidence level will be a constant for any set of T_i and equal to,

$$CL(u \cdot \frac{\sum T_i}{N} < \tau < v \cdot \frac{\sum T_i}{N}) \equiv \frac{\int_{\tau=CI_{min}}^{\tau=CI_{max}} L_N(\tau|T_i)\, \mathrm{d}\ln(\tau)}{\int_{\tau=0}^{\tau=+\infty} L_N(\tau|T_i)\, \mathrm{d}\ln(\tau)} = P(\frac{\tau'}{v} < \frac{\sum T_i'}{N} < \frac{\tau'}{u}|\tau') \tag{5.7}$$

The right-hand side of eq. 5.7 is the probability that the arithmetic mean of N random samples from an exponential distribution with the time constant τ' falls within

the interval $(\frac{\tau'}{v}, \frac{\tau'}{u})$. It is a constant for any $\tau' > 0$. If we consider a special case where $\tau' = \tau_0$, the right-hand side of eq. 5.7 is also the probability that the true time constant τ_0 is included in the confidence interval determined based on the N samples. Hence, the confidence level is correctly calculated by our method in terms of random sampling. This property is directly related to the point of view in a log scale. It further justifies our exponentially growing exposure sequence design and the uniform prior probability assumption of $\ln T$. In conclusion, our method reasonably estimates the time constant, confidence interval, and confidence level.

5.2 First Single Molecule Spectrum with Tropylium

In this section, I will introduce our first experimental result of the single molecule vibrational spectroscopy method, which to our knowledge, is the first recorded spectrum of a single gas phase polyatomic molecule. The tropylium ion ($C_7H_7^+$) is chosen to be the first molecular ion species to test our single molecule experiment method. It is a remarkably stable aromatic molecule. It has a seven-membered ring with six π-electrons. Its vibrational spectrum has been studied with the traditional action spectroscopy method.[18, 80, 81] Both the experimental data and the computational predictions are provided in those studies. They are used as a reference to initially test our method and verify the spectral results. Here, we measure the vibrational spectrum of single and for-sure pure tropylium ions between 2944 and 3150 cm^{-1}, demonstrating the high sensitivity of our method and the advantages of single molecule spectroscopy.

There are two prominent isomers of $C_7H_7^+$, tropylium (Tr^+) and benzylium (Bz^+), as shown in figure 5.5. Both of them can be produced by electric discharge and supersonic expansion from several precursors, such as toluene and cycloheptatriene. The structure of tropylium has been well-known for nearly a century since Hückel predicted its extraor-

dinary stability [82], and was proved experimentally as Doering and Knox synthesized its bromide salt [83]. This unique aromatic cation is believed to contribute to the $m = 91$ Da component of alkylbenzene mass spectra[84, 85]. Despite the longstanding interest in the two isomers and their landmark positions in the mass spectra of alkylbenzenes, a robust method to separate them in the gas phase for spectral studies has been absent for decades. The isomer-specific studies of their energy structures and gas-phase infrared spectra are only achieved recently.[18, 80] This is an excellent example of the isomer-induced challenging for ion mass spectrometry-based experiments, where the co-existing of isomers can hardly be separated. The recent progress relies on the varying producing ratio Tr^+/Bz^+ depending on the precursor. It allows the disentangling of the two isomers' spectra by varying the precursor. Such a disentangling method can resolve the strong spectral features of each isomer but is blind to some weak transitions.

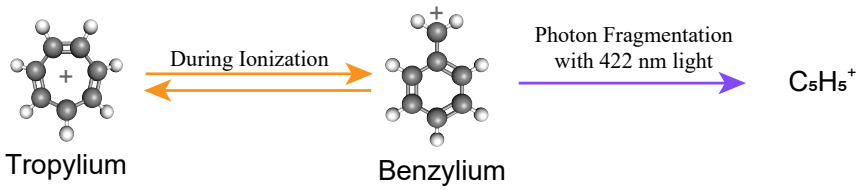

Figure 5.5: The structures of the tropylium ion and the benzylium ion represented by a ball-and-stick model. The fragmentation of benzylium is induced by the 422 nm light.[86]

We generate the tropylium ions via electron impact ionization of toluene. The benzylium ions produced together with the tropylium ions are photo-fragmented by the 422 nm light, when they are loaded into the trap.[86] We observe their fragment around 65 Dalton and typically remove them from the trap with radial constant tickles. Tropylium is therefore the only stably-trapped mass 91 Dalton isomer in our system, comfirmed by the absence of the known benzylium transitions at 2997 and 3116 cm^{-1}. [18]

The vibrational spectra of single tropylium molecules are shown in figure 5.6. The

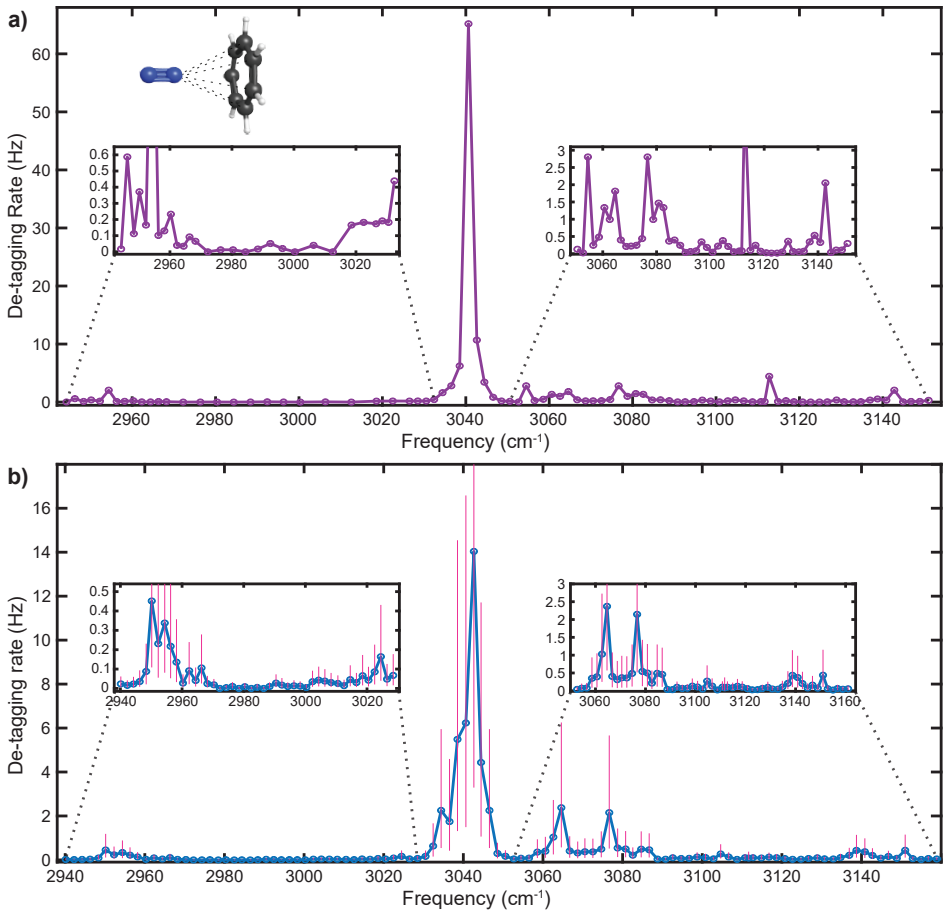

Figure 5.6: Single molecule spectra of tropylium. a) The infrared spectrum of a single Tr^+ molecule in the C-H stretching region. The strong transition at 3040 cm^{-1} is consistent with previous reports for N_2-tagged Tr^+,[18] which assign this transition as an asymmetric C–H stretch. Weak transitions, invisible to most other action techniques, are shown in the insets. We broadly attribute these features to combination bands. b) A composite of eight single molecule measurements. Three de-tagging measurements were made every 2 cm^{-1}. Maximum likelihood estimates of the de-tagging time constant are calculated at each point as described in section 5.1, with vertical bars indicating 95% confidence intervals for these values. The primary peak shifts slightly to 3042 cm^{-1} with these additional measurements. The confidence interval on the primary peak extends to 39 Hz. A total of eight Tr^+ molecules were used to measure all plotted points, as molecules were periodically lost due to reactive collisions with background gas.

spectra are taken with the pulsed mid-IR OPO laser (M Squared Lasers, Firefly IR) with 6 cm^{-1} linewidth. The vibrational spectrum measured with a single tropylium molecule in the C–H stretching region is shown in figure 5.6a). This single molecule data is consistent

with a composite spectrum taken from eight individual Tr^+ ions, shown in figure 5.6b). At least three de-tagging observations at every frequency step are used to estimate the de-tagging time constant based on the maximum likelihood method. (See in subsection 5.1.3.) The de-tagging rates reported in figure 5.6 are the inverse of these calculated time constants. The vertical bars in figure 5.6b) are 95% confidence intervals derived from the posterior probability density functions of the de-tagging time constant. Eight total molecular ions were used to obtain enough data points for this averaged spectrum, as the molecules were occasionally lost from the trap. For each new molecular ion loaded, we always verify the presence of the strong transition near 3042 cm^{-1} in order to confirm that it was a Tr^+ ion.

The dominant features in the spectra at 3042 cm^{-1} are consistent with previous tagging experiments,[18] which assigned this transition as the lone IR-active, asymmetric C–H stretching mode of Tr^+. A single transition at 3074 cm^{-1} was also reported, but the enhanced resolution of our method compared to conventional tagging spectroscopy allows us to resolve a previously unseen splitting of this peak into two features at 3065 and 3077 cm^{-1}. Multiple studies of Tr^+ have observed this band,[87] but it has yet to be assigned. In addition to these primary peaks, we observe weak transitions at 2952 and 3140 cm^{-1}. These peaks lay below the noise floor of other action spectroscopy methods and have therefore not been reported previously. They might be weak combination or overtone transitions.

The linewidths observed for transitions in 5.6 are limited both by the spectral profile of our OPO light source, as well as the natural timescale for the de-tagging process. While this timescale is different for each molecule, it is predicted to range anywhere from 0.1-100 ps,[73] giving a natural frequency resolution limit on the order of 10 GHz - 10 THz (0.3 - 300 cm^{-1}). Our observed noise level is dominated by sampling error, which is proportional to the de-tagging rate and is reduced by repeated measurements. We find

that three repetitions at each wavelength sampled are sufficient to reduce our sampling error to identify repeatable spectral features. Since the tagged lifetime for $Tr^+ \cdot N_2$ is several hours in the absence of mid-IR light, and >90 seconds off resonance, we are able to measure de-tagging events up to 90 seconds with a near-zero background. This high fidelity detection of weak features presents an ideal test for state-of-the-art theories of anharmonic contributions to spectra.

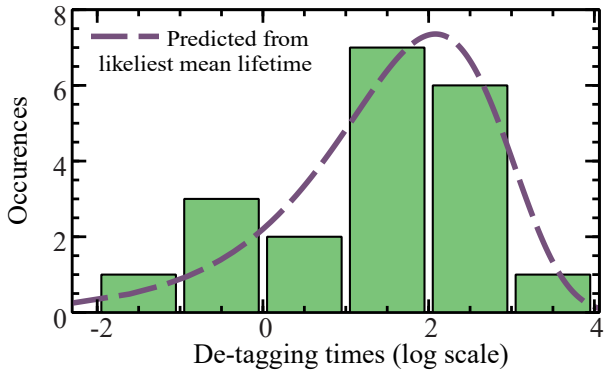

Figure 5.7: Single mid-IR frequency de-tagging histogram. A sample histogram of 20 lifetime measurements on the weak spectral feature at 2950 cm^{-1} shows consistency with the model of the exponential distribution.

Two wavelengths were chosen to test our assumption of the exponential distribution of the de-tagging time, with a sample histogram at 2950 cm^{-1} shown in figure 5.7. For this test, we measured 20 de-tagging times for Tr^+ irradiated with single frequency laser light at 2950 cm^{-1}. We observe a uniform distribution consistent with the exponential model described by equation 5.3. Additionally, we see no evidence of bimodality in this distribution, which might arise if the N_2 attaches to Tr^+ at different sites during successive measurements. Such effects from multiple tagging sites could be readily observed in other systems, however, by measuring the de-tagging time distribution for observed transitions at a single laser frequency.

The enriched features of the single molecule vibrational spectrum enable the identification of a single molecular ion. Although our method measures the absorption spectrum

of the molecular ion-tag Van der Waals complex, such as $Tr^+ \cdot N_2$, this spectrum is a very close analog to that of the bare molecular ion. The presence of a tag slightly perturbs selection rules and transition frequencies, but the typical line shifts are on the order of a few cm^{-1}.[75] As a result, the observed spectrum features and the strong absorption frequencies are directly related to the molecular ion structure. They can be used as the fingerprints of the molecules for identification. This identification method will be more powerful if we extend our spectral range to the fingerprint frequency region, which provides information about the presence or absence of specific functional groups.

5.3 Partially Resolved Rovibrational Spectrum of Tropylium

In the last section, we discussed the single molecule vibrational spectrum of the tropylium ion. It demonstrates the ability of our method to study and characterize a single molecule. Nevertheless, the frequency resolution of the spectra was found to be comparable to the laser linewidth, which indicates a potential improvement of the resolution by switching to a narrow-linewidth mid-IR laser. To find out the resolution limit of our method, we rented a 2 MHz-linewidth (0.00006 cm^{-1}) CW mid-IR laser (TOPO from TOPTICA) and retook the tropylium vibrational spectrum. In this section, I will introduce the obtained high-resolution vibrational spectra of single tropylium ions, in which the P-, Q-, and R-branches of the vibrational band near 3040 cm^{-1} are resolved. We achieve a sub-wavenumber frequency resolution, approaching the theoretical limit of our method by the natural timescale for the de-tagging process.

The high-resolution vibrational spectrum of single tropylium ion between 3030 cm^{-1} and 3080 cm^{-1} is shown in figure 5.8. The spectrum is taken with the same single

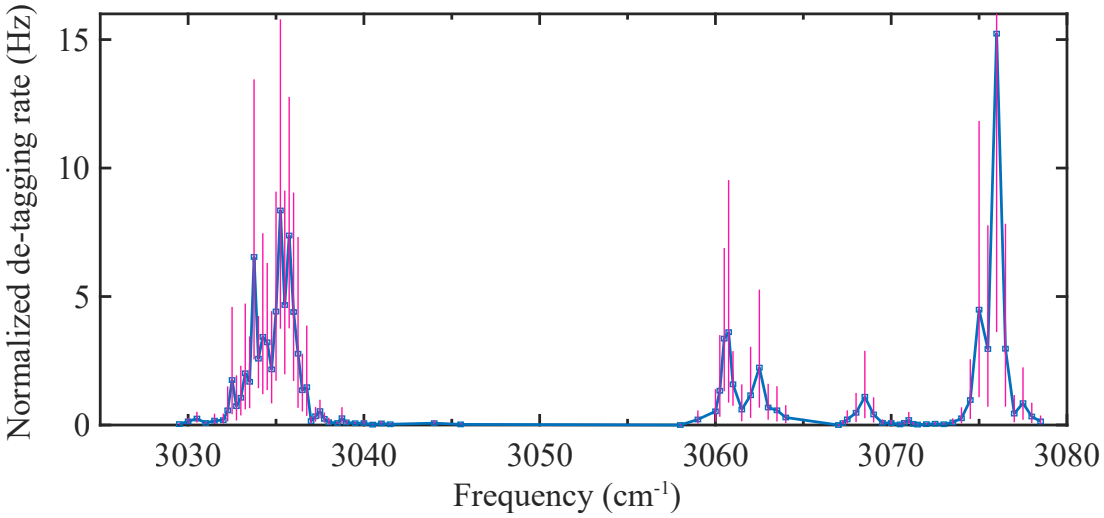

Figure 5.8: Single molecule infrared spectrum of tropylium. The de-tagging rate is normalized by the laser power. Vertical bars indicate the 95% confidence intervals. The confidence interval on the 3076 cm^{-1} peak extends to 42 Hz.

molecule method as previously introduced. We focused on the strong transitions in this spectrum due to our limited time to access the laser. The asymmetric C–H streching band around 3035.5 cm^{-1} was measured with 0.25 cm^{-1} steps. The previous unresolved single peak in figure 5.6 now splits into one main peak at the center and several weak features at the sides. The width of the whole structure is about 3 cm^{-1}, and the width of the peak at the center is 1 cm^{-1}, showing a better frequency resolution than the spectra taken with the Firefly laser. The width of this structure is very close to the span of the simulated C–H stretching ro-vibrational transitions at 8 Kelvin. In later discussions, we will prove the split peaks are contributed by the P, Q, and R branches of the C–H stretching band, respectively. The center frequency of this band shifts for about 6 cm^{-1} compared with figure 5.6. It is likely due to the internal calibration error and the about 10 cm^{-1} linewidth of the Firefly laser. The frequency of the TOPO laser is monitored by a HighFinesse wavemeter (WS-6) with up to 0.001 cm^{-1} resolution, which is much more accurate than the internal calibration of the Firefly laser. Hence, the peak frequency in

the high-resolution vibrational spectrum is much more reliable. The spectral features between 3060 cm^{-1} and 3080 cm^{-1} are also clearly resolved to be four distinct peaks. The abnormal long flat shoulder between the 3065 cm^{-1} and 3077 cm^{-1} peaks in figure 5.6 is now proven to be a weak transition broadened by the laser.

Although the TOPO laser has an excellent frequency resolution, we could not lock its frequency and power in our limited renting time. The frequency drifts at each frequency step are controlled within 0.003 cm^{-1}, and no evidence shows the spectral is sensitive to the laser frequency at such a scale. A power meter monitored the laser power from a back-reflected beam at a neutral density filter in the beam path. The de-tagging time data of each measurement is scaled by the laser power to compensate for the power drifts over time. The scaled data is then analyzed with the maximum likelihood method introduced in section 5.1.3 and gives the normalized de-tagging rate, representing the averaged absorption probability to the mid-IR photons.

As the frequency resolution of the spectrum becomes comparable to the rotational constants of the molecular ion at 0.1 cm^{-1} level, the de-tagging rates become dependent on the rotational state of the molecular ion-tag complex. The internal degrees of the complex is buffer gas cooled to about 8 Kelvin. And the rotational quantum number J of the highest thermally populated rotational state is qualitatively determined by $\sqrt{\frac{k_B T}{B}}$, where B is the rotational constant of the complex. The enriched rotational levels of the complex lead to a tremendous amount of ro-vibrational transitions in a single vibrational band. For a certain vibrational band $\nu_i \rightarrow \nu_i'$, the ro-vibrational transitions $|\nu, J\rangle \rightarrow |\nu', J'\rangle$ can be divided into three categories, the P-, Q- and R-branch transitions, where $\Delta J = -1, 0, 1$, respectively. (See in figure 5.9 a.) From one initial state $|\nu, J\rangle$, the splittings between the three types of transitions depend on the energy difference between the rotational modes of the final state. These splittings are typically at the level of $2BJ$, ignoring the effect of the other rotational quantum numbers. As J increases, the frequen-

cies of the P-branch transitions decrease, and that of the R-branch transitions increase. In our spectra, those ro-vibrational transitions are broadened by the rapid intramolecular vibrational energy redistribution (IVR) process[88], which causes the de-tagging of the complex. The transitions contribute to the ro-vibrational spectrum when the complex is at the correct initial rotational state. When measuring the spectrum of a thermalized complex ensemble, the transition intensity is scaled by the thermal population of the initial states. The experimental spectra are interpreted as an averaged effect of all the populated states. In the single-molecule cases, the validity of this interpretation remains unknown.

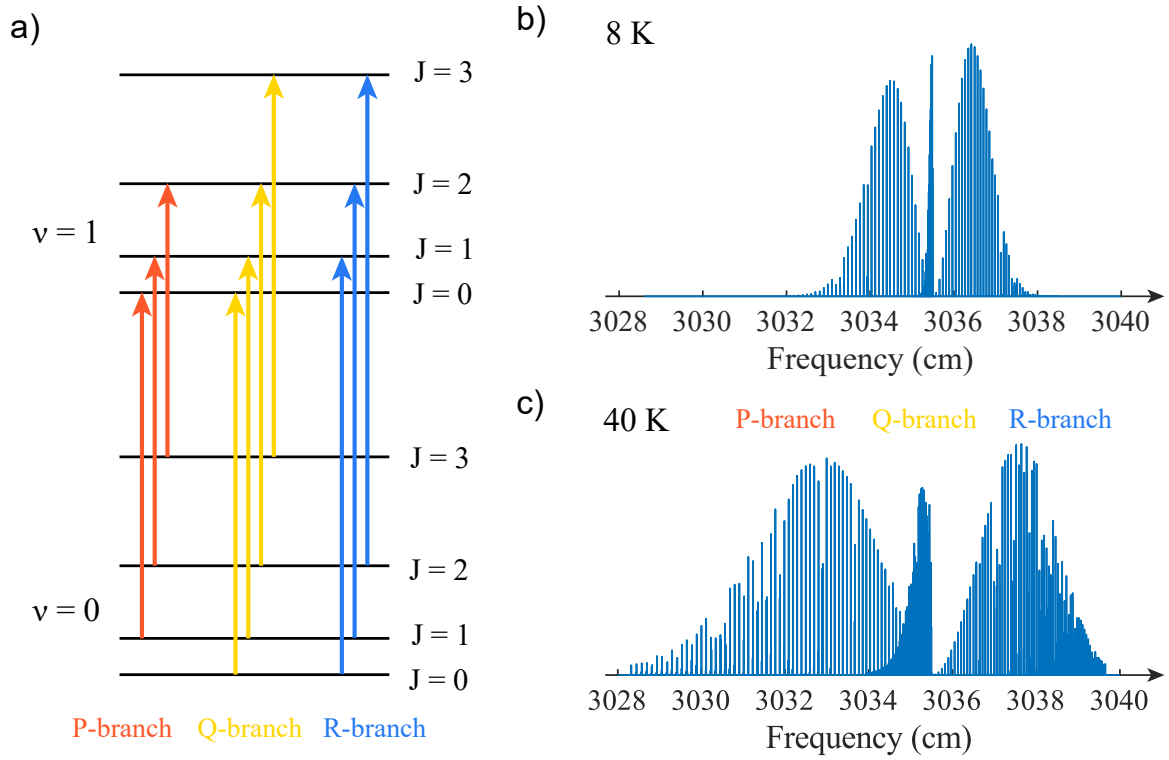

Figure 5.9: a) The P-, Q- and R-branches. b) Simulated ro-vibrational spectra of the "face-tagged" $Tr^+ \cdot N_2$ complex (see in figure 5.6 a) at 8 K. c) Simulated ro-vibrational spectra of the "face-tagged" $Tr^+ \cdot N_2$ complex at 40 K.

At the sub-wavenumber level, the high-resolution spectrum of tropylium shows no

strongly frequency-dependent features. It indicates that the IVR-induced broadening is large enough to smooth the spectrum. The broadening of the C–H stretching mode transitions is estimated to be at least 0.1 cm^{-1} (3 GHz) and at most 1 cm^{-1} (30 GHz). We assume our about 200 Hz background collision rate is high enough so that the spectral lines of all the possibly populated initial states are effectively detected. Figure 5.9 b and c show the simulated unbroadened ro-vibrational spectra of the "face-tagged" $Tr^{+}{\cdot}N_2$ complex at 8 K and 40 K, respectively. The width of the simulated 8 K spectrum is similar to the observed feature around 3035.5 cm^{-1}. We believe the distinct peaks in this observed feature are indeed the three rotational branches of the C–H vibrational transition. We verified this hypothesis with a novel hot single molecule vibrational spectroscopy method demonstrated in the following subsection.

5.3.1 Vibrational Spectra of Hot Single Molecules

To check whether the rotational branches are resolved, we designed a method to take single molecule vibrational spectra with rotationally hot tagged complex. The heating to the rotational degrees is achieved by increasing the collisional energy with the background gas. With this method, we obtained the C–H stretching mode spectrum of tropylium at about 40 K (the hot molecule spectrum), where the P-, Q- and R-branches are clearly resolved. The central peak position of the hot molecule spectrum is consistent with the 8 K cold molecule spectrum, and the width of the spectral feature agrees with the simulation's prediction (see in figure 5.9).

Radial constant tickle (see in section 4.2.4) is used to heat the rotational degrees of the molecular ion-tag complex. When the molecular ion is at rest at the trap center, its rotation is cooled during the collisions with the buffer gas. Such collisions induce a rotational state transfer that couples the translational and rotational energy. The rota-

tional quantum number J can only get higher if the collisions have relative translational energy greater than the amount of energy going into rotation.[89] It is hard to change the buffer gas temperature without affecting the vacuum. So we choose to increase the translational energy of the molecular ion to induce high-energy collisions for heating the rotation. As introduced in section 4.2.4, we can coherently drive the radial motion of the ions at a certain mass with an AC voltage at their radial secular frequency. It will decouple the driven ions, with the rest ions staying at the trap center. If the driving voltage is controlled below 0.16 V, the driven ions can remain in the ion trap, rapidly oscillating at their radial secular frequency. The energy input by the driving voltage is either dissipated during collisions or canceled by itself due to the anharmonicity of the trapping potential. Either way, the ions will reach a quasi-stable status where the averaged speed of the translational motion is controlled by the driving amplitude. When the speed of an ion is much higher than the background gas, its speed will dominate the collisional energy.

The driving voltages from 0.01 V to 0.1 V have been tested in increments of 0.01 V for 1 minute each with the $Tr^+ \cdot N_2$ complex. The driving frequency is the radial secular frequency of the complex. The N_2 tag survived all but the 0.1 V constant tickle. When the complex is tickled at 0.1 V, the N_2 tag is removed from the tropylium ion in a few seconds, characterized by the return of the bare tropylium ion. We believe such a de-tagging event is due to the collisions that are more energetic than the binding energy of the tag (about 800 K). To avoid such collision-induced de-tagging, we typically set the driving voltage to 0.05 V, where the lifetime of the tag is measured to be more than 15 minutes in the absence of the mid-IR light. With this 0.05 V radial constant tickle, we can heat the internal degrees of the complex without affecting the tag.

An adjusted lock-in detection method is applied to detect the de-tagging event of the "hot" complex. The constant radial tickle introduced above is applied to keep the

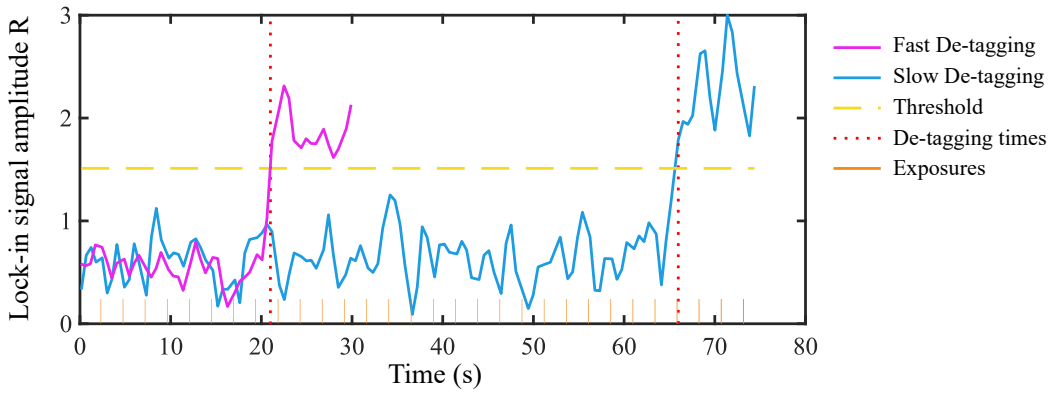

Figure 5.10: Two Samples of the lock-in signal showing a fast and a slow de-tagging event.

complex hot. When the molecular ion is tagged, it is coherently driven by the radial tickle. A single $^{88}Sr^{+}$ ion is left at the trap center. If the complex de-tags, the bare tropylium will return. And a two-ion chain containing a $^{88}Sr^{+}$ and a bare tropylium will form at the trap center. This crystal has an axial COM mode frequency about 0.25 kHz lower than the $^{88}Sr^{+}$'s axial secular frequency. The axial lock-in signal can detect this frequency shift, based on which we can monitor the presence and absence of the tag. We typically set the axial driving signal to the two-ion crystal's COM mode frequency and monitor the lock-in amplitude. The lock-in signal will show off-resonance before the de-tagging event and become on-resonance after the de-tagging. Hence the de-tagging event is observed as the discontinuous rise of the lock-in amplitude. Combining this adjusted lock-in detection method with the mid-IR exposure sequence, we can measure the laser-induced de-tagging rate of the hot complex.

The single molecule vibrational spectra of a rotationally hot $Tr^{+}{\cdot}N_2$ complex is taken and shown in figure 5.11. At least three data points are used to estimate the de-tagging rate at each frequency. The hot molecule spectrum's C–H stretching band has three distinct peaks. Each peak is about 1 cm^{-1} wide with broad wings on the sides. These peaks are further separated than the cold molecule spectrum. Moreover, the spectral intensities

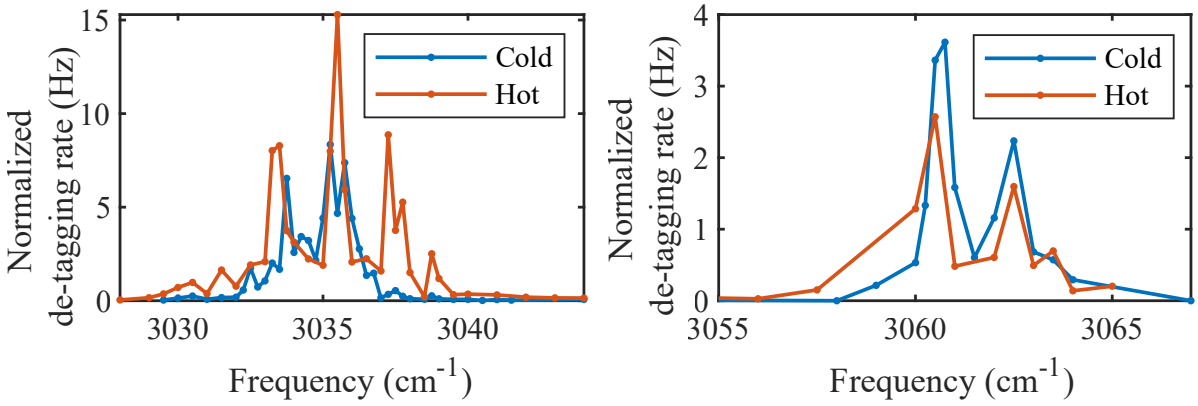

Figure 5.11: Single molecule vibrational spectra of tropylium with (hot) and without (cold) radial constant tickle. a) The spectra between 3028 and 3044 cm^{-1} show the C–H stretching band with the center peak at 3035.5 cm^{-1}. b) The spectra between 3055 and 3067 cm^{-1}.

are higher than the cold molecule spectrum at frequencies far from the center. All these features agree with the behavior of the P-, Q- and R-branches at high temperatures. We fit the hot molecule spectrum with the simulations and find it best fit with the simulated spectrum at 40 K (see in figure 5.9 c). Given these facts, we conclude that our radial constant tickle successfully heats the rotational modes of the complex to about, if not above, 40 K, and the three peaks in the hot spectra show the P-, Q-, and R-branches of the C–H stretching band. The pure vibrational transition is determined to be at 3035.5 cm^{-1}.

In figure 5.11 b, the peak of the hot molecule spectrum at 3060.5 cm^{-1} is also broadened at the low-frequency side. But we don't have a clear interpretation of the whole feature due to the limited data taken.

Two histograms are taken at 3031 cm^{-1} to confirm the de-tagging rate difference between the hot and cold molecule spectra. Thirteen data points are included in each histogram. Figure 5.12 shows that both histograms agree with the exponential distribution assumption. The two de-tagging time constants are well-distinguished from each other. We attribute this solid difference to the higher thermal occupation rate of the

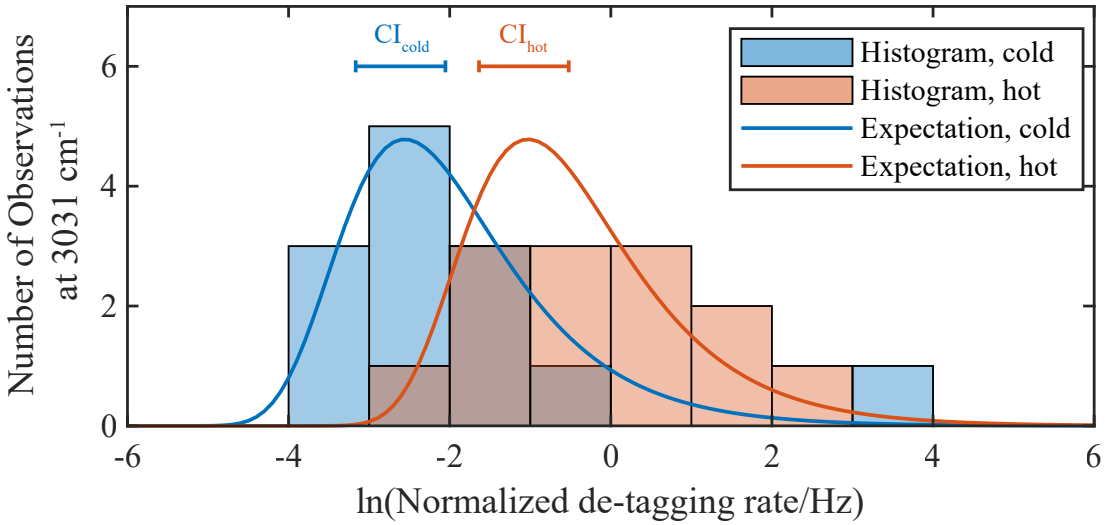

Figure 5.12: Single mid-IR frequency de-tagging rate histograms of the cold and hot molecules. Both sample histograms of 13 normalized de-tagging rate measurements at 3031 cm^{-1} are consistent with the exponential distribution model. The two curves show the expected distribution characterized by the estimated de-tagging time constants. The bars on the top give the 95% confidence intervals (CI) of the de-tagging time constant. The CI of the hot is well-distinguished from the cold.

rotational states with J of about 50 in the hot molecule experiment. The rotational energy of these states is about 100 cm^{-1} (150 K), so they are barely occupied at 8K. The P-branch ro-vibrational transitions from those states are around 3031 cm^{-1}, contributing significantly to the local de-tagging rate.

In conclusion, we resolve the P-, Q-, and R-branches and observe the broad wings in the single molecule vibrational spectra of rotationally hot $Tr^{+}{\cdot}N_2$ complex. It demonstrates the validity of the collisional heating method and the sub-wavenumber branch-resolved resolution of our single molecule spectroscopy method.

5.3.2 Summary of Tropylium Spectra

Figure 5.13 compares the two spectra taken with the TOPO laser with our broadband spectrum and the traditional action spectroscopy data measured by J. Philipp Wagner *et.*

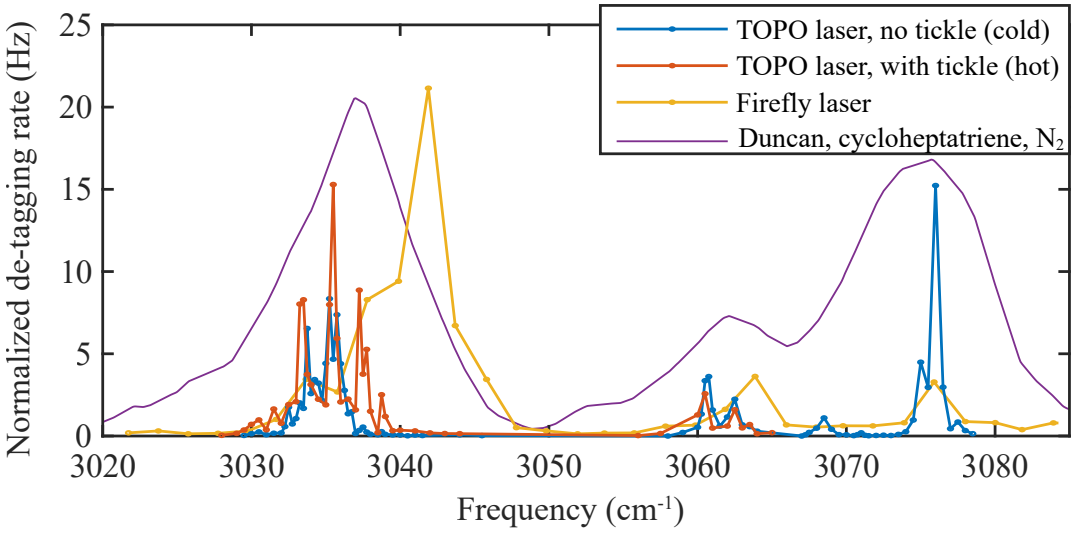

Figure 5.13: Four mid-IR vibrational spectra of tropylium in the C–H stretching region taken with different methods. The blue curve shows the single molecular spectrum taken with the TOPO laser, and the orange one shows the spectrum when the radial constant tickle heats the molecular ion-tag complex. The yellow curve is the single molecular spectrum taken with the Firefly laser. At last, the purple curve is the infrared photodissociation spectrum obtained with a cycloheptatriene precursor and nitrogen tagging provided by Prof. Michael A. Duncan. Reprint(adapted) with permission from [18]. Copyright 2018 American Chemical Society. Their spectra include the transitions of both the tropylium and benzylium isomers. But the spectrum is mainly assigned to the tropylium transitions in this frequency range and with a cycloheptatriene precursor.

al. in Prof. Michael A. Duncan's group.[18]. All the spectra agree with each other within the spectral resolution limit, showing our spectra correctly characterized the tropylium ion. In addition, our single molecule vibrational spectroscopy method achieves an order of magnitude better resolutions and can reliably detect weak spectral features. The features enable the single molecular ion identification and provide valuable information on polyatomic molecular ions for chemical dynamics studies, computational assignment of the spectra, and testing high-level chemical theories.

5.4 Other Molecular Ions

As the performance of the single molecule vibrational spectroscopy was well studied in the last two sections, we move forward to test the generality of our method by measuring the spectra of more molecular ion species. In this section, I present the vibrational spectra for the single cationic fragments of both indole (C_8H_7N) and 1,3-benzodioxole ($C_6H_4O_2CH_2$) in the C–H stretching region.

The first molecular ion sample is a 90 Da photofragment of indole, referred to as ion **i** in this section. Indole is a prototypical heterocyclic aromatic molecule. The same bicyclic structure is found in the side chain of the amino acid tryptophan and is involved in the synthesis of tryptophan. Therefore, the indole molecule has a biological relevance and is of interest in the studies of searching for the start of life in the interstellar medium.[90] When we ionize the parent indole molecule, we aim at the 117 Da indole radical cation peak, where the neutral molecule loses one electron. This cation ion has a broad electronic band near 335 nm[91], and we find it fragments in the presence of our 422 nm with an estimated lifetime of several minutes. In this experiment, we obtained a 90 Da ion fragment (ion **i**) after the photo-fragmentation, during which the indole radical cation lost a mass of 27 Da (most likely to be HCN). We achieved the measurements of the whole single molecule vibrational spectrum with that one ion.

The second sample is the dehydrogenated fragment of 1,3-benzodioxole (referred to as ion **ii**). 1,3-Benzodioxole is also a heterocyclic organic molecule with a mass of 122 Da. They tend to lose one hydrogen during ion loading, generating the 121 Da ion fragment in our ion trap. The structure of the ion is determined based on the computational method, shown in figure 5.14 b.

The single molecule vibrational spectra of the ion **i** and **ii** are measured and shown in figure 5.14. We used the Firefly laser, and the spectra were recorded in 4 cm^{-1} intervals.

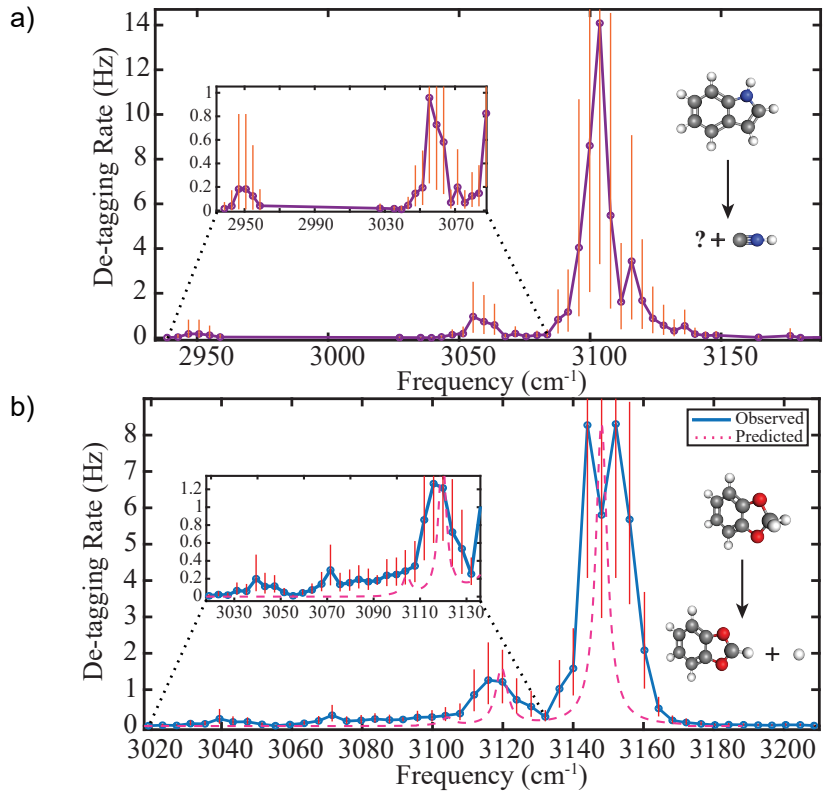

Figure 5.14: Single molecule vibrational spectra. The vertical bars are the 95% confidence intervals. a) 90 Da ion **i**. No standard data points are taken between 2960 and 3030 cm^{-1}, but a fast scan shows the lifetime is below 0.1 Hz in this region. b) 121 Da ion **ii**. The dashed line shows the prediction of a simulation calculated at the B3LYP/aug-cc-pVTZ level of theory.

Our spectra catch both strong landmarking transitions as well as weak features. Each of these spectra is measured with only one molecular ion; therefore, each is only contributed by one ion species. These spectra of pure single molecular ions are well distinguishable, even just measured in this commonly occupied C–H stretching frequency region. The barely overlapped spectral features guarantee a robust way to distinguish the ion species. These results illustrate the robustness and the generality of our single molecule vibrational spectroscopy. And they also demonstrate our experiments as a promising analytical tool to characterize the molecular cation and to study ion-neutral reactions and photofragmentation processes.

5.4.1 Failures and Limitations

Although our method is, in principle, generalizable to other molecular ions, we have been confronted with several failures due to experimental limitations. In this section, I will introduce the typical failures and our restriction to the analyte molecular ion.

One of the most basic requirements for the analyte molecular ion is that it needs to be cation and in the mass range from 55 Da to 150 Da (if it is singly charged). This requirement is imposed by the trapping and sympathetic cooling conditions. To achieve robust trapping and sympathetic cooling, the ion should have a comparable mass-to-charge ratio to the $^{88}Sr^+$ ion. A broader mass range can be covered by using a different laser-cooled atomic ion species, including Be^+, Mg^+, Ca^+, Ra^+, and Yb^+. With these ions, the molecular mass range can be extended to 3 - 500 Da. We haven't tested any multiply charged molecular ion, which in principle can work but need further studies.

Another requirement is that the molecular ion should not have a strong transition near 422 nm or 1092 nm (the $^{88}Sr^+$ cooling and the re-pump laser frequencies). For example, the N-methylpyrrole cation at mass 81 Da can absorb the 1092 nm laser. As a result, its N_2 tagged complex automatically de-tags in 10 seconds without being exposed to mid-IR light, which is too short for our measurement. If an electronic transition is driven, the molecular ion can also photo-fragment like benzylium and indole cation. In these cases, switching $^{88}Sr^+$ to a different laser-cooled atomic ion species that requires lasers at different frequencies may be helpful.

The last requirement is imposed by the current ion generation and loading process. The current electron impact ionization method is easy to operate but requires a parent molecule with a vapor pressure above 1 mTorr. If such a parent molecule is not available, a different ionization method should be applied if such a parent molecule is unavailable. Thankfully, a variety of well-developed ionization methods are available, such as electro-

spray ionization[92] and matrix-assisted laser desorption/ionization (MALDI)[93]. Some molecular ions also tend to fragment in high-energy collisions with buffer gas during loading, where a collision with neon can potentially release about a quarter of the total kinetic energy of the molecular ion. Such a process is observed by the ions loaded to the trap at a different mass than the quadrupole mass filter's targeted mass. To solve this problem, the system needs to be calibrated for a lower ion speed. Another possible solution is to adopt voltage-gated loading, where the ions are initially slowed down by the electric field instead of the buffer ion. In general, all these kinds of issues in the ion loading procedures can be solved by adjusting the ion generation system, which does not affect the single molecule vibrational spectroscopy method.

Chapter 6

Chapter 6 Summary and Outlook

6.1 Summary

In this work, we built an experimental platform for studying and identifying a broad class of single molecular ions. We combined the idea of the traditional mass spectrometry-based gas-phase action spectroscopy (mainly cryogenic ion vibrational predissociation (CIVP) spectroscopy) with the techniques developed for laser-cooled ion crystals. We successfully achieved the first gas-phase single polyatomic molecule vibrational spectroscopy with the analyte molecular ion co-trapped with a $^{88}Sr^{+}$ in a cryogenic ion trap.

We built the ion generation system based on a quadrupole mass filter. In the relatively separated Extrel chamber, we can produce, mass-select, transport, and detect the ions. Both $^{88}Sr^{+}$ and the molecular ions can be generated in the Extrel chamber via laser ablation and electron impact ionization, respectively. Within the ion generation system, we can perform simple mass spectrometry and verify the ion production independently.

Our main chamber provides the ions with a well-controlled and isolated experimental environment. A cryogenic ion trap setup was designed and built in the main chamber to confine the ions. The generated ions can be loaded into the trap with buffer gas pulses.

With buffer gas cooling, laser cooling and sympathetic cooling techniques, we prepare ion crystals containing $^{88}Sr^+$ at milliKelvin temperatures.

We achieved efficient information readout via the $^{88}Sr^+$ fluorescence with the help of our laser system and imaging system. We can observe the ion crystal's structure and motion in the trap. We designed the experimental procedures to prepare the polyatomic molecular ion-$^{88}Sr^+$ two-ion crystals. With this type of crystal trapped in the well-controlled potential, non-destructive mass spectrometry is achieved based on the measurements of its secular motion frequency. We also designed a pulse sequence to tag the molecular ion with a N_2, where the weak ion-tag bond can be destroyed by vibrational excitation. Leveraging these two techniques, we performed the previously destructive mass spectrometry-based CIVP spectroscopy with a single molecule in the ion trap non-destructively, which gives the single molecule vibrational spectra.

We demonstrated the single molecule vibrational spectroscopy method with the measurements of the infrared spectra with a single tropylium and two other ion fragments in the C–H stretching region. Among them, the spectrum of the single tropylium molecule is the first recorded spectrum of a single gas-phase polyatomic molecule. To determine the ultimate frequency resolution of our method, we employed a narrow linewidth mid-IR laser and obtained rotational branches-resolved single molecule vibrational spectra of rotationally hot and rotationally cold tropylium molecules, respectively. We found the frequency resolution to be at the sub-wavenumber level. Our spectra feature a high resolution and sensitivity compared to traditional CIVP spectra. The spectra clearly show both strong and weak spectral features, providing enough information to distinguish, if not identify, single ion species. More importantly, the studied single molecules are the tiniest and purest possible analyte molecular samples, greatly simplifying the analytical problems. Hence, our nondestructive single molecule vibrational spectroscopy can serve as a general and flexible analytical tool to assist ongoing research in multiple fields.

Our experimental setup is relatively concise and easy to build. Unlike traditional action spectroscopy, no dedicated instrument is needed to perform individual steps of our experiment. Instead, most of the experiment steps are all done in one cryogenic ion trap. Such a design is compatible with many experimental setups, including those for quantum logic spectroscopy. It delivers a new opportunity to realize complicated multi-step experiments for studying single molecular ions and their chemical dynamics, where our method can be used as a single step to measure the ion mass or identify the ion species.

6.2 Outlook

So far, our single molecule vibrational spectroscopy has been initial tested as a prototypical framework. As the primary goal of demonstrating the feasibility of our method is achieved, we can move on to make use of our method to solve real research questions.

One straightforward application of our experiment is to help assign the vibrational spectra. The isomer selectivity, improved frequency resolution, and high sensitivity of our spectra make them excellent references for theoretical models and quantum chemical calculations. The vibrational bands can potentially be assigned to certain vibrational modes of a molecular structure. Based on the assignment, the structure of the molecular ion can be verified. The calculation accuracy can also be determined to benchmark the models and theories.[94] The great sensitivity of our spectra enables the detection of weak combination or overtone transitions. Their frequencies provide valuable information about the anharmonic effects for testing the anharmonic calculations.

Another direction is simply to take more spectra of more molecular ions. Our method takes data slower compared to traditional tagging spectroscopy. It is not likely to replace the traditional methods but helps to deconvolve the spectra of different isomers and

to improve the frequency resolution and spectral contrast. A spectral library can be potentially built where the spectra of each isomer are identified. Several extensions can be considered to access the spectra of more molecular ion species. Other ionization methods and additional laser-cooled atomic ion options can extend single molecule vibrational spectroscopy to a broader class of polyatomic molecules in the mass range of 3 - 500 Da. This library will be a great tool for chemical analysis. For instance, this library can help to determine the isomer ratio of ion ensembles used in traditional action spectroscopy experiments. The frequency range of our spectra can also be extended. The lower frequency limit depends on the tag's binding energy, which is typically below 1000 cm^{-1}. The upper limit of the spectra is set by the photo-fragmentation or photoisomerization frequency[95], at which the high-energy photons can destroy the molecular ion structure.

In addition, our experiment setup has great potential in studying photo-fragmentation processes and ion-neutral reaction pathways. The molecular ion is robustly confined in our ion trap as long as its mass remains in the stable mass region of the rf trap. Our single molecule vibrational spectroscopy can non-destructively determine the ion structure after each reaction or fragmentation step, which no other experimental technique can do. This method is compelling when a long reaction/fragmentation pathway is studied. Repeating experiments will also determine the branching ratio of the reaction/fragmentation products.

Our single molecule vibrational spectroscopy may have a great impact on the astrochemical studies of interstellar medium. First of all, the single molecule sensitivity allows the identification of rare organic samples captured from outer space.[96] Secondly, our ion trap setup is a great platform to simulate the space environment. We can study the astrochemical dynamics, including photo- and collision-induced transitions, fragmentation and isomerization processes. There are ongoing experiments in our lab cooperating with the simulation works to study the indole's dissociation dynamic, which could be of

interest in astrochemistry.[97] These experiments not only help to understand the chemical dynamics in the interstellar bands but also provide spectral information of potential molecule candidates to look for in the absorption spectrum of the interstellar medium.[98]

Moreover, since our experimental method and setup are compatible with quantum logic spectroscopy (QLS), our method can be employed as a complementary technique to search polyatomic ion candidates for QLS.

At last, our experiment provides a solid foundation for pursuing unperturbed and rotationally resolved single molecule vibrational spectroscopy. The established laser-induced inhibition of complex growth (LIICG) spectroscopy[99, 100] and "leak-out" spectroscopy[101] methods are both compatible with our single-molecule technique. They enable the detection of the bare molecular ion spectra, which are not perturbed by the tag and are narrow enough to be rotationally resolved. Besides the high precision of this spectroscopy, the recorded rotationally resolved vibrational spectra in principle enable the rotational cooling and pure quantum state preparation of the molecular ion.[102, 103] This can be a significant step to the full quantum control of the polyatomic molecular ion.

Appendix A

Method of Images

Numerical methods are widely used to solve Laplace's equation with a given boundary condition, which describes the electric potential in space containing no charge. They work robustly for all regular and irregular boundaries. However, the results of numerical simulations are generally inaccurate when focussing on the small features. Hence, I adopt the method of images to qualitatively characterize the radial electric field for studying the averaged motion and pseudo-potential in our radio frequency trap.

To simplify the problem, I only consider four infinitely long radial electrodes. I assume the trap geometry and the quadrupole radio frequency field are perfectly symmetric. The quadrupole field is approximated by the electric field generated by four line charges (see the red points in figure A.1). The positions of the charges are fixed to the diagonals, and the distance to the center is determined by the condition that the electric potential is the same at three reference points on the electrode surface separated by $\pi/2$ (see the yellow points in figure A.1).

Notably, the electric potential fall to zero at infinity. It indicates the voltages applied to all four electrodes should oscillate around the ground. However, in the real case, we only apply the RF voltages to two of the electrodes. As a result, the actual RF field

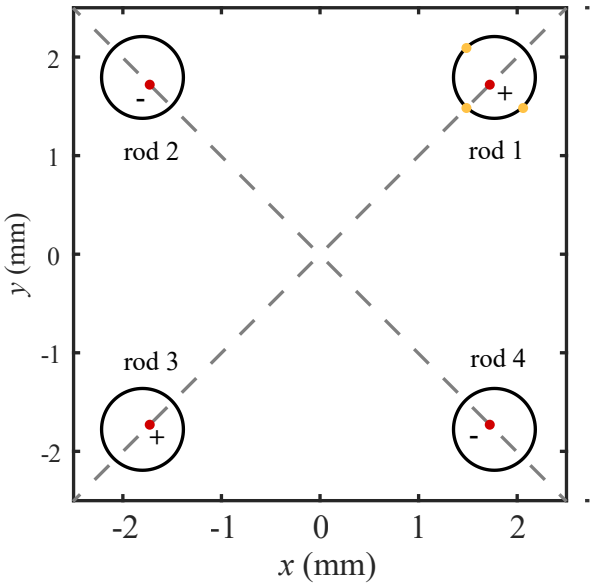

Figure A.1: The geometry of the electrodes, the imagined line charges, and reference points.

would slightly diverge from the prediction due to the effects of the grounded surfaces far from the ion trap, such as the inner radiation shield.

A similar method is used to simulate the electric field when biased voltages are applied to the diagonally opposite electrodes. Such an electric field could drive the radial motion of the ions and is used in radial tickles. The approximate solution of the electric field is generated by 6 line charges shown in figure A.2.

The two line charges inside the two biased electrodes generate the primary component of the electric field (see the red points in figure A.2). The equipotential surface of their electric field can perfectly match the surface of the two electrodes. Weak dipoles will be induced on the other two electrodes, and each of them is simulated with a pair of line charges. The charge density and the position of the line charges are determined by the conditions that the electric field intensity equals zero at point A and point B (see the yellow points in figure A.2), especially along the tangential direction (see the blue lines).

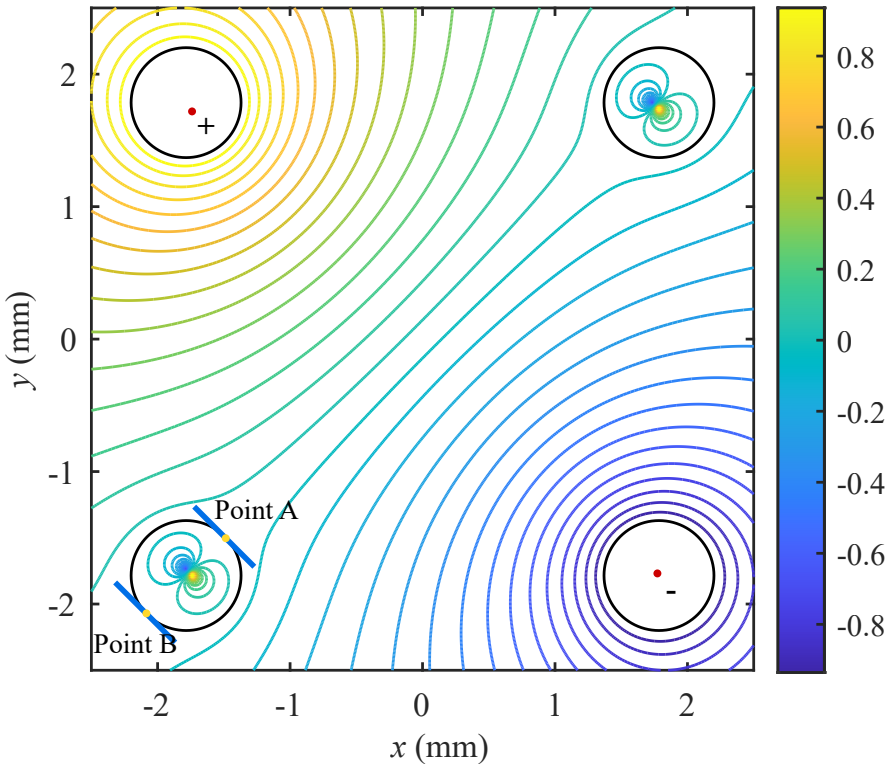

Figure A.2: The equipotential maps of the simulated diagonally biased electric field.

Appendix B

Other Mass Filters for Ion Loading

Before adopting the commercial Extrel system (see in section 3.3) as the central part of the ion generation system, we tested several methods to mass-select and detect the production of the ions. The residual gas analyzer (RGA) from Stanford Research System has a very similar structure to the Extrel system but does not contain a quadrupole deflector. Figure B.1 a shows the experimental setup to test the laser ablation loading scheme of metal ions. The result of ablating Al-Sr alloy is shown in figure B.2. Three distinct peaks at 27, 44, and 88 Daltons show the production of $^{27}Al^{+}$, $^{88}Sr^{2+}$, and $^{88}Sr^{+}$. The full width at one-tenth of the maximum is about 2 Dalton.

Time of flight (TOF) mass spectrometry is also tested for ablation loading. Due to the wide initial energy distribution in ablation ionization, TOF mass spectrometry setups without an energy selector could barely resolve the mass of the ions. I inserted a homemade electrostatic energy analyzer (bender) into the ion trajectory as shown in figure B.1 b and found the time of flight peaks corresponding to ions at different masses become resolvable as expected. Figure B.3 shows the result of ablating the aluminum target and Al-Sr alloy target, where the time of flight is converted to the mass-to-charge ratio based on the $^{27}Al^{+}$ peak. The targeting kinetic energy is 25 eV, and the electric

field accelerator (between the target and the electrode) provides 13.5 eV of the total energy. The relative mass resolution of the setup is about 10 %, which corresponds to the bender's relative energy resolution of 20 %. By changing the acceleration voltage, we can determine the population of the produced ions with certain initial energy based on the peak height. This method can be used to study the initial energy distribution and optimize the ablation parameters.

In conclusion, the quadrupole mass filter (QMF) shows a better mass resolution. It is superior to the TOF setup for the ability to cooperate with continuous ion sources such as electron impact ionizers. But we also find TOF setup and bender are helpful to study and control the initial energy of the produced ion. In the Extrel system, the quadrupole mass filter cooperating with the quadrupole bender provides a robust mass selection of the ions.

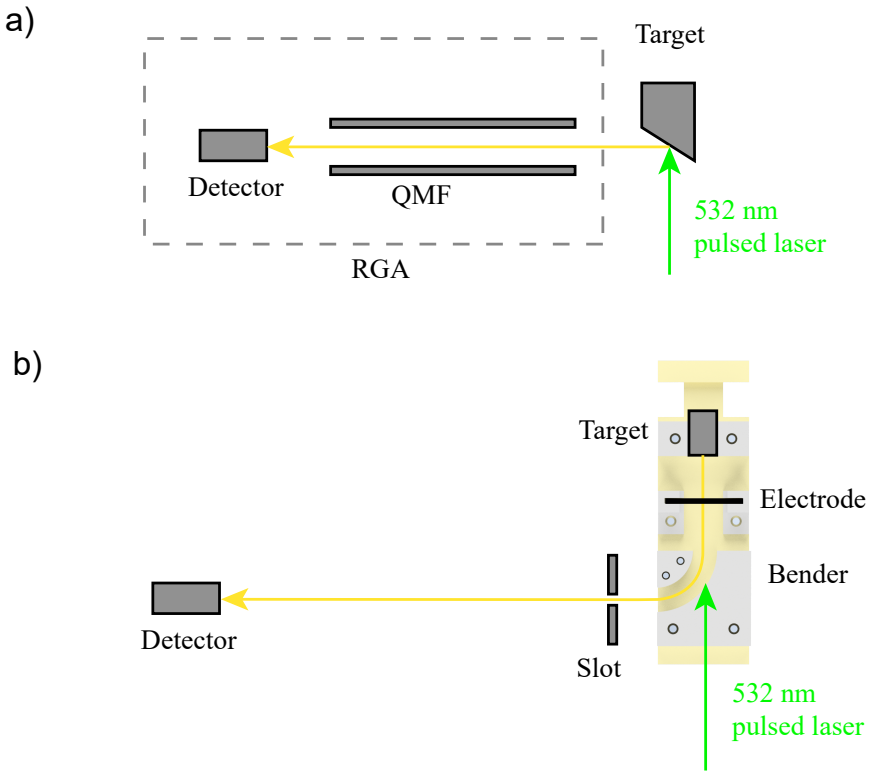

Figure B.1: The schematic diagram of the experimental setup to test a) the QMF in the RGA and b) the TOF mass spectrometry with the bender.

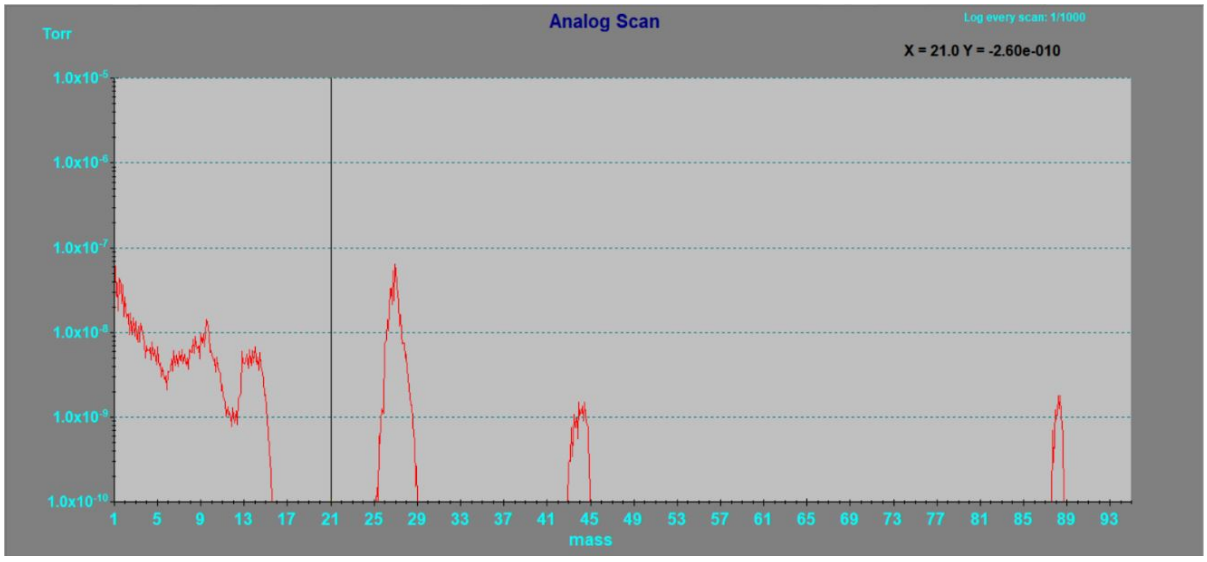

Figure B.2: Mass spectrum of Al-Sr alloy. Mass selection is performed with the QMF in the RGA. Software copyright belongs to Stanford Research Systems.

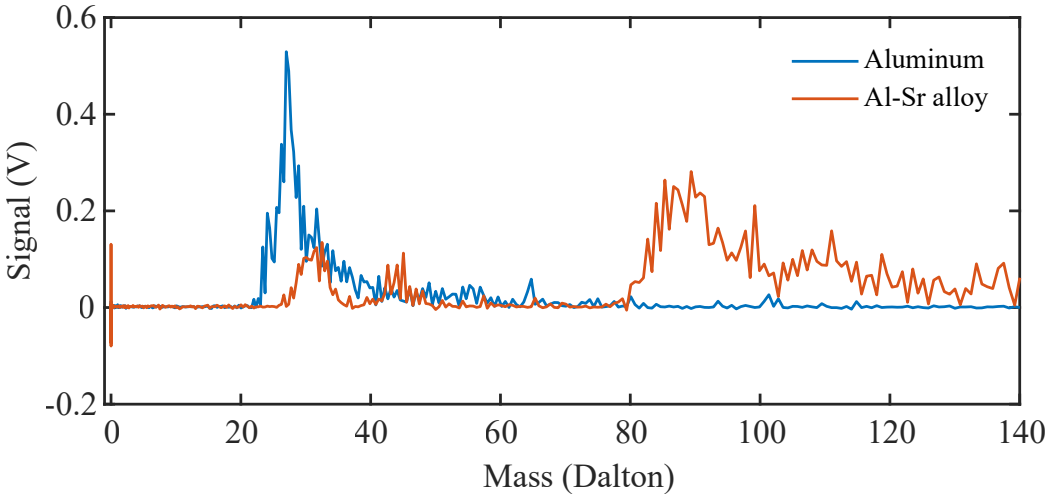

Figure B.3: Mass spectrum of pure aluminum and Al-Sr alloy. Mass selection is performed with the TOF mass spectrometry.

Appendix C

Objective Stack

The design of the objective lens stack is shown below. It is designed by Ce Pei and is optimized for 10× magnification. The working distance of the objective is about 5 cm. To achieve a larger tuning range and a greater depth of field, the lens stack is used as a 5× objective in the bottom (main) imaging system I designed, where the performance is sacrificed.

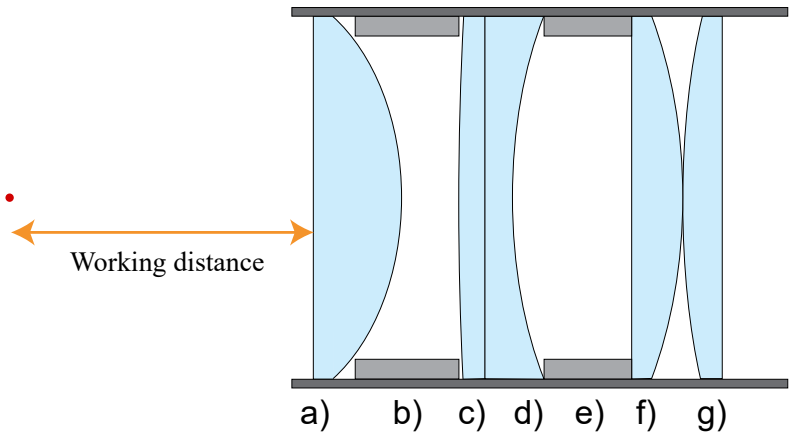

Figure C.1: Objective lens stack of the main imaging system. The lenses are two-inch diameter plano-convex/concave lenses from Thorlabs, and the spacer rings are home--machined with inner diameters of 1.875 inches and outer diameters of 2 inches. a) Thorlabs LA1145-A. b) 0.745-inch-long spacer ring. c) Thorlabs LA1779-A. d) Thorlabs LC1611-A. e) 0.707-inch-long spacer ring. f) Thorlabs LA1417-A. g) Thorlabs LA1301-A.

Appendix D

Graphical User Interface

I wrote a graphical user interface (GUI) in Matlab to monitor the lock-in signal, control the axial tickle and take data. It controls two timers. One timer updates and records the lock-in R-value (amplitude) about every 0.5 seconds, and the other one controls and records the opening and closing of the mechanical shutter in the mid-IR beam path. Since the timer's period is inaccurate, a timestamp is included in each data point and shutter event to determine the exact order of the events. This recorded data enables the auto-determination of the total exposure time before a de-tagging event. The axial tickle frequency to apply is automatically determined based on the resonance frequency of the ion crystal containing the bare molecule.

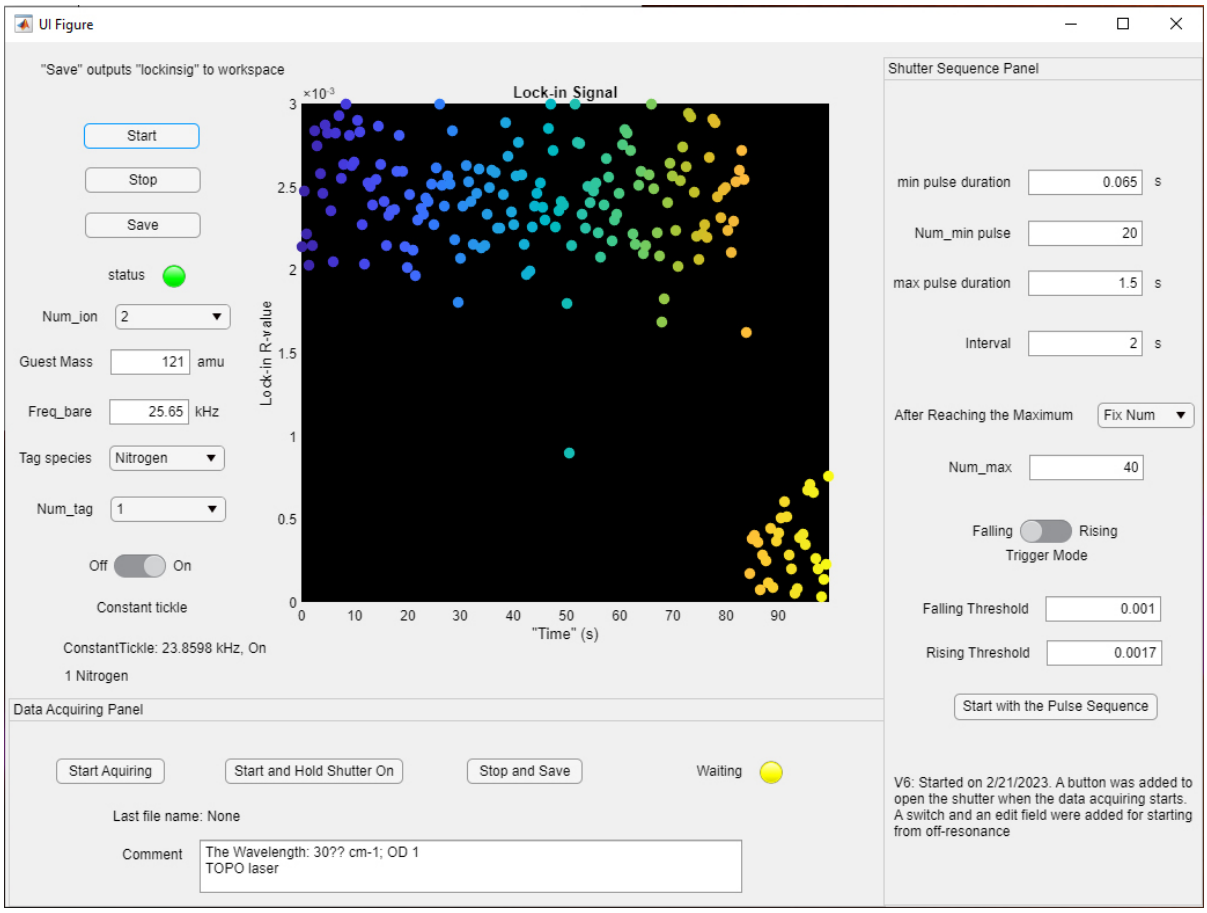

Figure D.1: The graphical user interface monitoring a de-tagging event.

Appendix E

Optical Tweezers

Optical tweezers are a promising tool to generate a state-dependent potential.[104] Such a state-dependent potential is predicted as a general tool for the internal state readout of polyatomic molecular ions.[105] We built and tested optical tweezers using a 532 nm CW laser (Sprout-Solo from Lighthouse Photonics Inc.). The tweezers laser is focused on the trap center from the opposite direction to the side camera, allowing the observation of the ions and the tweezers simultaneously (see in figure E.2). The optical setup is shown in figure E.1. We use the first-order output of the AOM, enabling fast gating of the beam. A pair of cylindrical lenses calibrate the elliptical beam shape of the first-order output. Two beam expanders expand the beam to about 2 cm wide. Passing the expanders, the beam is directed to a $f = 20$ cm objective lens mounted on a three-axis translation stage, which focuses the beam to the trap center. The smallest beam waist observed is about 10 μm based on the images taken by the side imaging system.

In later testing with a two-ion crystal, we found the optical tweezers could cause a displacement of the ions of tens microns after the tweezers laser was turned on for a few seconds. Moreover, the ions tend to return to the origin positions with a delay of seconds to minutes after the laser is off. We believe these facts indicate the displacement

is caused by either heating or photon-induced charging phenomenon. This displacement is so large that measuring the optical tweezers' direct effects on ions becomes impossible. The further test of the optical tweezers has been postponed since then. A better focus and a larger trap may be helpful for later experiments with optical tweezers and cryogenic ion traps.

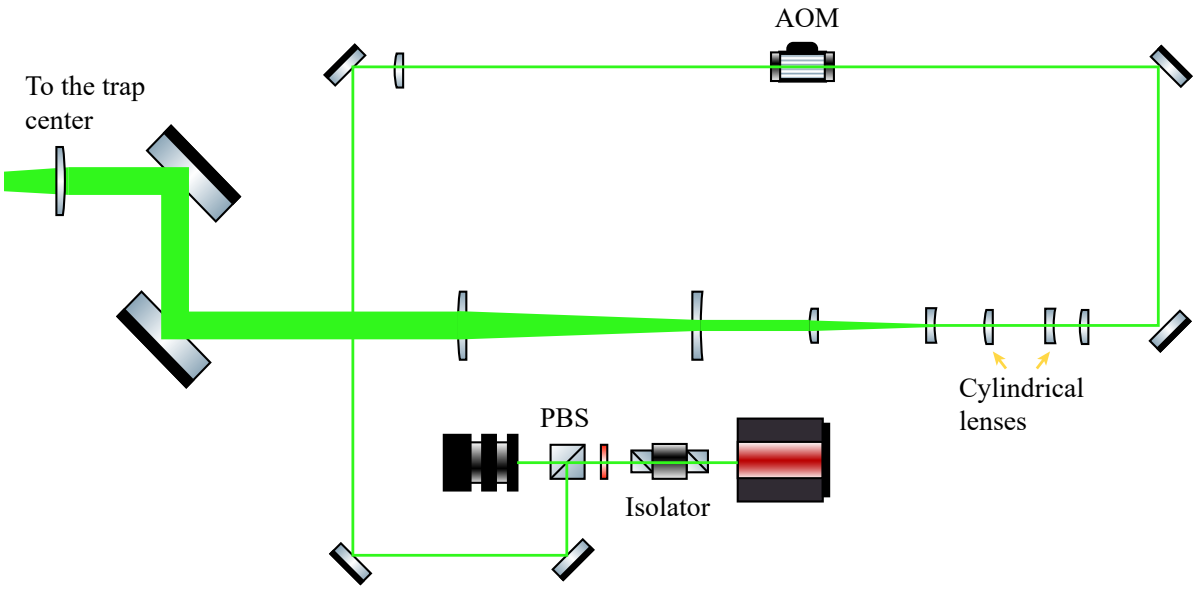

Figure E.1: The optical tweezers setup.

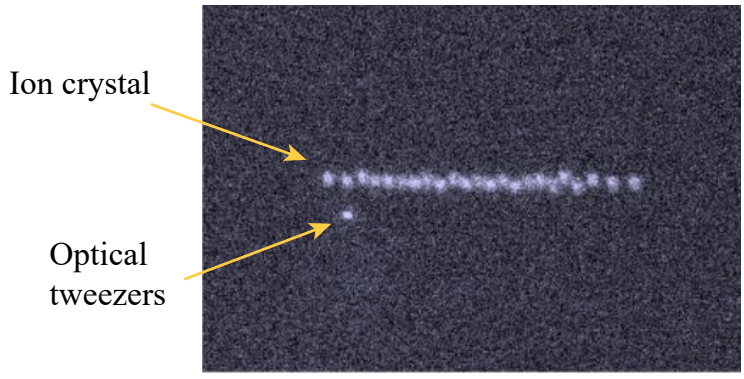

Figure E.2: The optical tweezers is focused to a point below the $^{88}Sr^{+}$ ion crystal. The beam waist of the optical tweezers is estimated to be 10 μm.

Bibliography

[1] A. Pereverzev and J. Roithová, *Experimental techniques and terminology in gas-phase ion spectroscopy*, *Journal of Mass Spectrometry* **57** (2022), no. 5 e4826.

[2] J. N. Dodds and E. S. Baker, *Ion mobility spectrometry: fundamental concepts, instrumentation, applications, and the road ahead*, *Journal of the American Society for Mass Spectrometry* **30** (2019), no. 11 2185–2195.

[3] V. Yatsyna, A. H. Abikhodr, A. Ben Faleh, S. Warnke, and T. R. Rizzo, *High-throughput multiplexed infrared spectroscopy of ion mobility-separated species using hadamard transform*, *Analytical Chemistry* **94** (2022), no. 6 2912–2917.

[4] A. B. Wolk, C. M. Leavitt, E. Garand, and M. A. Johnson, *Cryogenic ion chemistry and spectroscopy*, *Accounts of chemical research* **47** (2014), no. 1 202–210.

[5] W. D. Phillips, *Nobel lecture: Laser cooling and trapping of neutral atoms*, *Reviews of Modern Physics* **70** (1998), no. 3 721.

[6] D. Leibfried, R. Blatt, C. Monroe, and D. Wineland, *Quantum dynamics of single trapped ions*, *Reviews of Modern Physics* **75** (2003), no. 1 281.

[7] T. A. Isaev and R. Berger, *Polyatomic candidates for cooling of molecules with lasers from simple theoretical concepts*, *Physical review letters* **116** (2016), no. 6 063006.

[8] C. Myatt, E. Burt, R. Ghrist, E. A. Cornell, and C. Wieman, *Production of two overlapping bose-einstein condensates by sympathetic cooling*, *Physical Review Letters* **78** (1997), no. 4 586.

[9] A. O. Wallis and J. M. Hutson, *Production of ultracold NH molecules by sympathetic cooling with mg*, *Physical review letters* **103** (2009), no. 18 183201.

[10] D. Kielpinski, B. King, C. Myatt, C. A. Sackett, Q. Turchette, W. M. Itano, C. Monroe, D. J. Wineland, and W. H. Zurek, *Sympathetic cooling of trapped ions for quantum logic*, *Physical Review A* **61** (2000), no. 3 032310.

[11] T. Rosenband, D. Hume, P. Schmidt, C.-W. Chou, A. Brusch, L. Lorini, W. Oskay, R. E. Drullinger, T. M. Fortier, J. E. Stalnaker, *et. al.*, *Frequency ratio of Al^+ and Hg^+ single-ion optical clocks; metrology at the 17th decimal place*, *Science* **319** (2008), no. 5871 1808–1812.

[12] C.-w. Chou, C. Kurz, D. B. Hume, P. N. Plessow, D. R. Leibrandt, and D. Leibfried, *Preparation and coherent manipulation of pure quantum states of a single molecular ion*, *Nature* **545** (2017), no. 7653 203–207.

[13] S. A. King, L. J. Spieß, P. Micke, A. Wilzewski, T. Leopold, E. Benkler, R. Lange, N. Huntemann, A. Surzhykov, V. A. Yerokhin, *et. al.*, *An optical atomic clock based on a highly charged ion*, *Nature* **611** (2022), no. 7934 43–47.

[14] F. Wolf, Y. Wan, J. C. Heip, F. Gebert, C. Shi, and P. O. Schmidt, *Non-destructive state detection for quantum logic spectroscopy of molecular ions*, *Nature* **530** (2016), no. 7591 457–460.

[15] M. Sinhal and S. Willitsch, *Molecular-ion quantum technologies*, *Photonic Quantum Technologies: Science and Applications* **1** (2023) 305–332.

[16] K. Sheridan and M. Keller, *Weighing of trapped ion crystals and its applications*, *New Journal of Physics* **13** (2011), no. 12 123002.

[17] P. E. Miller and M. B. Denton, *The quadrupole mass filter: basic operating concepts*, *Journal of chemical education* **63** (1986), no. 7 617.

[18] J. P. Wagner, D. C. McDonald, and M. A. Duncan, *Mid-infrared spectroscopy of $C_7H_7^+$ isomers in the gas phase: Benzylium and tropylium*, *The journal of physical chemistry letters* **9** (2018), no. 16 4591–4595.

[19] R. Coisson, G. Vernizzi, and X. Yang, *Mathieu functions and numerical solutions of the mathieu equation*, in *2009 IEEE International Workshop on Open-source Software for Scientific Computation (OSSC)*, pp. 3–10, IEEE, 2009.

[20] N. McLachlan, *Vibrational problems in elliptical coordinates*, *Quarterly of Applied Mathematics* **5** (1947), no. 3 289–297.

[21] N. Konenkov, M. Sudakov, and D. Douglas, *Matrix methods for the calculation of stability diagrams in quadrupole mass spectrometry*, *Journal of the American Society for Mass Spectrometry* **13** (2002), no. 6 597–613.

[22] C. J. Foot, *Atomic physics*, vol. 7. OUP Oxford, 2004.

[23] W. Demtröder, *Atoms, molecules and photons*, vol. 3. Springer, 2010.

[24] P. O. Schmidt, T. Rosenband, C. Langer, W. M. Itano, J. C. Bergquist, and D. J. Wineland, *Spectroscopy using quantum logic*, *Science* **309** (2005), no. 5735 749–752.

[25] Z. Meir, G. Hegi, K. Najafian, M. Sinhal, and S. Willitsch, *State-selective coherent motional excitation as a new approach for the manipulation, spectroscopy and state-to-state chemistry of single molecular ions*, *Faraday discussions* **217** (2019) 561–583.

[26] W. E. Gifford and R. Longsworth, *Surface heat pumping*, in *Advances in Cryogenic Engineering: Proceedings of the 1965 Cryogenic Engineering Conference Rice University Houston, Texas August 23–25, 1965*, pp. 171–179, Springer, 1966.

[27] T. Tomaru, T. Suzuki, T. Haruyama, T. Shintomi, A. Yamamoto, T. Koyama, and R. Li, *Vibration analysis of cryocoolers*, *Cryogenics* **44** (2004), no. 5 309–317.

[28] C. Day, *Basics and applications of cryopumps*, CERN, 2007.

[29] H. G. Dehmelt, *Radiofrequency spectroscopy of stored ions i: Storage*, in *Advances in atomic and molecular physics*, vol. 3, pp. 53–72. Elsevier, 1968.

[30] P. K. Ghosh, *Ion traps*, Dec, 1995.

[31] A. Reuben, G. Smith, P. Moses, A. Vagov, M. Woods, D. Gordon, and R. Munn, *Ion trajectories in exactly determined quadrupole fields*, *International Journal of Mass Spectrometry and Ion Processes* **154** (1996), no. 1-2 43–59.

[32] A. Zangwill, *Modern electrodynamics*. Cambridge University Press, 2013.

[33] K. Jennings, *Collision-induced decompositions of aromatic molecular ions*, *International Journal of Mass Spectrometry and Ion Physics* **1** (1968), no. 3 227–235.

[34] U. Justesen, *Collision-induced fragmentation of deprotonated methoxylated flavonoids, obtained by electrospray ionization mass spectrometry*, *Journal of Mass Spectrometry* **36** (2001), no. 2 169–178.

[35] B. L. Lan and J. M. Bowman, *Collision induced isomerization of a semirigid bender hydrogen cyanide*, *The Journal of chemical physics* **101** (1994), no. 10 8564–8571.

[36] K. Mølhave and M. Drewsen, *Formation of translationally cold MgH^+ and MgD^+ molecules in an ion trap*, *Physical Review A* **62** (2000), no. 1 011401.

[37] J. Koelemeij, B. Roth, A. Wicht, I. Ernsting, and S. Schiller, *Vibrational spectroscopy of HD^+ with 2-ppb accuracy*, *Physical Review Letters* **98** (2007), no. 17 173002.

[38] S. Willitsch, M. T. Bell, A. D. Gingell, S. R. Procter, and T. P. Softley, *Cold reactive collisions between laser-cooled ions and velocity-selected neutral molecules*, *Physical review letters* **100** (2008), no. 4 043203.

[39] O. Krohn, K. Catani, and H. Lewandowski, *Formation of astrochemically relevant molecular ions: Reaction of translationally cold CCl^+ with benzene in a linear ion trap*, *Physical Review A* **105** (2022), no. 2 L020801.

[40] H. Häffner, W. Hänsel, C. Roos, J. Benhelm, D. Chek-al Kar, M. Chwalla, T. Körber, U. Rapol, M. Riebe, P. Schmidt, *et. al.*, *Scalable multiparticle entanglement of trapped ions*, *Nature* **438** (2005), no. 7068 643–646.

[41] D. Tabor, V. Rajagopal, Y.-W. Lin, and B. Odom, *Suitability of linear quadrupole ion traps for large coulomb crystals*, *Applied Physics B* **107** (2012) 1097–1104.

[42] S. X. Wang, G. Hao Low, N. S. Lachenmyer, Y. Ge, P. F. Herskind, and I. L. Chuang, *Laser-induced charging of microfabricated ion traps*, *Journal of Applied Physics* **110** (2011), no. 10 104901.

[43] A. Härter, A. Krükow, A. Brunner, and J. Hecker Denschlag, *Long-term drifts of stray electric fields in a paul trap*, *Applied Physics B* **114** (2014) 275–281.

[44] D. Field, O. Plekan, A. Cassidy, R. Balog, N. Jones, and J. Dunger, *Spontaneous electric fields in solid films: spontelectrics*, *International Reviews in Physical Chemistry* **32** (2013), no. 3 345–392.

[45] A. Holmes, *Theoretical and experimental study of space charge in intense ion beams*, *Physical review A* **19** (1979), no. 1 389.

[46] S. D. Tanner, *Space charge in ICP-MS: calculation and implications*, *Spectrochimica Acta Part B: Atomic Spectroscopy* **47** (1992), no. 6 809–823.

[47] M. Brownnutt, V. Letchumanan, G. Wilpers, R. Thompson, P. Gill, and A. Sinclair, *Controlled photoionization loading of $^{88}Sr^+$ for precision ion-trap experiments*, *Applied Physics B* **87** (2007) 411–415.

[48] S. Amoruso, R. Bruzzese, N. Spinelli, and R. Velotta, *Characterization of laser-ablation plasmas*, *Journal of Physics B: Atomic, Molecular and Optical Physics* **32** (1999), no. 14 R131.

[49] J. Benedikt, A. Hecimovic, D. Ellerweg, and A. Von Keudell, *Quadrupole mass spectrometry of reactive plasmas*, *Journal of Physics D: Applied Physics* **45** (2012), no. 40 403001.

[50] D. Egorov, T. Lahaye, W. Schöllkopf, B. Friedrich, and J. M. Doyle, *Buffer-gas cooling of atomic and molecular beams*, *Physical Review A* **66** (2002), no. 4 043401.

[51] D. Patterson, J. Rasmussen, and J. M. Doyle, *Intense atomic and molecular beams via neon buffer-gas cooling*, *New Journal of Physics* **11** (2009), no. 5 055018.

[52] A. Kellerbauer, T. Kim, R. Moore, and P. Varfalvy, *Buffer gas cooling of ion beams*, *Nuclear Instruments and Methods in Physics Research Section A: Accelerators, Spectrometers, Detectors and Associated Equipment* **469** (2001), no. 2 276–285.

[53] A. Hansen, O. Versolato, Ł. Kłosowski, S. Kristensen, A. Gingell, M. Schwarz, A. Windberger, J. Ullrich, J. C. López-Urrutia, and M. Drewsen, *Efficient rotational cooling of coulomb-crystallized molecular ions by a helium buffer gas*, *Nature* **508** (2014), no. 7494 76–79.

[54] S. Aiba, M. Ohashi, and S.-Y. Huang, *Rapid determination of oxygen permeability of polymer membranes*, *Industrial & Engineering Chemistry Fundamentals* **7** (1968), no. 3 497–502.

[55] F. Giacobbe, *Oxygen permeability of teflon–PFA tubing*, *Journal of applied polymer science* **39** (1990), no. 5 1121–1132.

[56] H. Margolis, G. Barwood, G. Huang, H. Klein, S. Lea, K. Szymaniec, and P. Gill, *Hertz-level measurement of the optical clock frequency in a single $^{88}Sr^{+}$ ion*, *Science* **306** (2004), no. 5700 1355–1358.

[57] H. Zhang, M. Gutierrez, G. H. Low, R. Rines, J. Stuart, T. Wu, and I. Chuang, *Iterative precision measurement of branching ratios applied to 5p states in $^{88}Sr^{+}$*, *New Journal of Physics* **18** (2016), no. 12 123021.

[58] A. Madej, L. Marmet, and J. Bernard, *Rb atomic absorption line reference for single Sr^{+} laser cooling systems*, *Applied Physics B* **67** (1998) 229–234.

[59] A. Shiner, A. Madej, P. Dubé, and J. Bernard, *Absolute optical frequency measurement of saturated absorption lines in Rb near 422 nm*, *Applied Physics B* **89** (2007) 595–601.

[60] D. W. Preston, *Doppler-free saturated absorption: Laser spectroscopy*, *American Journal of Physics* **64** (1996), no. 11 1432–1436.

[61] F. Diedrich, E. Peik, J. Chen, W. Quint, and H. Walther, *Observation of a phase transition of stored laser-cooled ions*, *Physical review letters* **59** (1987), no. 26 2931.

[62] M. Raizen, J. Gilligan, J. C. Bergquist, W. M. Itano, and D. J. Wineland, *Ionic crystals in a linear paul trap*, *Physical Review A* **45** (1992), no. 9 6493.

[63] L. Hornekær and M. Drewsen, *Formation process of large ion coulomb crystals in linear paul traps*, *Physical Review A* **66** (2002), no. 1 013412.

[64] E. L. Pollock and J.-P. Hansen, *Statistical mechanics of dense ionized matter. ii. equilibrium properties and melting transition of the crystallized one-component plasma*, *Physical Review A* **8** (1973), no. 6 3110.

[65] W. Slattery, G. Doolen, and H. DeWitt, *Improved equation of state for the classical one-component plasma*, *Physical Review A* **21** (1980), no. 6 2087.

[66] J. Wesenberg, R. Epstein, D. Leibfried, R. Blakestad, J. Britton, J. Home, W. M. Itano, J. D. Jost, E. Knill, C. Langer, *et. al.*, *Fluorescence during doppler cooling of a single trapped atom*, *Physical Review A* **76** (2007), no. 5 053416.

[67] T. Sikorsky, Z. Meir, N. Akerman, R. Ben-Shlomi, and R. Ozeri, *Doppler cooling thermometry of a multilevel ion in the presence of micromotion*, *Physical Review A* **96** (2017), no. 1 012519.

[68] D. Larson, J. C. Bergquist, J. J. Bollinger, W. M. Itano, and D. J. Wineland, *Sympathetic cooling of trapped ions: A laser-cooled two-species nonneutral ion plasma*, *Physical review letters* **57** (1986), no. 1 70.

[69] G. Morigi and H. Walther, *Two-species coulomb chains for quantum information*, *The European Physical Journal D-Atomic, Molecular, Optical and Plasma Physics* **13** (2001) 261–269.

[70] D. Berkeland, J. Miller, J. C. Bergquist, W. M. Itano, and D. J. Wineland, *Minimization of ion micromotion in a paul trap*, *Journal of applied physics* **83** (1998), no. 10 5025–5033.

[71] M. Fan, C. Holliman, X. Shi, H. Zhang, M. Straus, X. Li, S. Buechele, and A. Jayich, *Optical mass spectrometry of cold $RaOH^+$ and $RaOCH_3^+$*, *Physical Review Letters* **126** (2021), no. 2 023002.

[72] G. G. Brown, B. C. Dian, K. O. Douglass, S. M. Geyer, S. T. Shipman, and B. H. Pate, *A broadband fourier transform microwave spectrometer based on chirped pulse excitation*, *Review of Scientific Instruments* **79** (2008), no. 5 053103.

[73] K. Von Puttkamer, H.-R. Dübal, and M. Quack, *Time-dependent processes in polyatomic molecules during and after intense infrared irradiation*, *Faraday Discussions of the Chemical Society* **75** (1983) 197–210.

[74] K. Spears, *Ion-neutral bonding*, *The Journal of Chemical Physics* **57** (1972), no. 5 1850–1858.

[75] C. J. Johnson, A. B. Wolk, J. A. Fournier, E. N. Sullivan, G. H. Weddle, and M. A. Johnson, *Communication: He-tagged vibrational spectra of the SarGlyH$^+$ and H$^+$(H$_2$O)$_{2,3}$ ions: Quantifying tag effects in cryogenic ion vibrational predissociation (CIVP) spectroscopy*, *The Journal of Chemical Physics* **140** (2014), no. 22 221101.

[76] C. J. Johnson and M. A. Johnson, *Vibrational spectra and fragmentation pathways of size-selected, D_2-tagged ammonium/methylammonium bisulfate clusters*, *The Journal of Physical Chemistry A* **117** (2013), no. 50 13265–13274.

[77] T. N. Olney, N. Cann, G. Cooper, and C. Brion, *Absolute scale determination for photoabsorption spectra and the calculation of molecular properties using dipole sum-rules*, *Chemical physics* **223** (1997), no. 1 59–98.

[78] P. Zoller, M. Marte, and D. Walls, *Quantum jumps in atomic systems*, *Physical Review A* **35** (1987), no. 1 198.

[79] S. Gleyzes, S. Kuhr, C. Guerlin, J. Bernu, S. Deleglise, U. Busk Hoff, M. Brune, J.-M. Raimond, and S. Haroche, *Quantum jumps of light recording the birth and death of a photon in a cavity*, *Nature* **446** (2007), no. 7133 297–300.

[80] P. Jusko, A. Simon, S. Banhatti, S. Brünken, and C. Joblin, *Direct evidence of the benzylium and tropylium cations as the two long-lived isomers of $C_7H_7^+$*, *ChemPhysChem* **19** (2018), no. 23 3182–3185.

[81] U. Jacovella, M. S. Scholz, and E. J. Bieske, *Electronic spectrum of the tropylium cation in the gas phase*, *The Journal of Physical Chemistry Letters* **11** (2020), no. 20 8867–8872.

[82] Q. B. Zum Bezolproblem and Q. B. zum Problem, *Quantentheoretische beiträge zum benzolproblem*, *Zeitschrift Fuer Physikalische Chemie* **70** (1931) 204–286.

[83] W. Von E. Doering and L. Knox, *The cycloheptatrienylium (tropylium) ion*, *Journal of the American Chemical Society* **76** (1954), no. 12 3203–3206.

[84] G. Merling, *Ueber tropin*, *Justus Liebigs Annalen der Chemie* **216** (1883), no. 3 329–355.

[85] P. N. Rylander, S. Meyerson, and H. M. Grubb, *Organic ions in the gas phase. ii. the tropylium ion*, *Journal of the American Chemical Society* **79** (1957), no. 4 842–846.

[86] G. Féraud, C. Dedonder-Lardeux, S. Soorkia, and C. Jouvet, *Photo-fragmentation spectroscopy of benzylium and 1-phenylethyl cations*, *The Journal of Chemical Physics* **140** (2014), no. 2 024302.

[87] W. G. Fateley and E. R. Lippincott, *Vibrational spectrum and structure of the tropylium ion*, *The Journal of Chemical Physics* **26** (1957), no. 6 1471–1481.

[88] J. Oomens, B. G. Sartakov, G. Meijer, and G. Von Helden, *Gas-phase infrared multiple photon dissociation spectroscopy of mass-selected molecular ions*, *International Journal of Mass Spectrometry* **254** (2006), no. 1-2 1–19.

[89] J. Polanyi and K. Woodall, *Mechanism of rotational relaxation*, *The Journal of Chemical Physics* **56** (1972), no. 4 1563–1572.

[90] S. Albert, K. K. Albert, P. Lerch, and M. Quack, *Synchrotron-based highest resolution fourier transform infrared spectroscopy of naphthalene ($C_{10}H_8$) and indole (C_8H_7N) and its application to astrophysical problems*, *Faraday discussions* **150** (2011) 71–99.

[91] N. Chalyavi, K. Catani, J. Sanelli, V. Dryza, and E. Bieske, *Gas-phase electronic spectrum of the indole radical cation*, *Molecular Physics* **113** (2015), no. 15-16 2086–2094.

[92] J. B. Fenn, M. Mann, C. K. Meng, S. F. Wong, and C. M. Whitehouse, *Electrospray ionization for mass spectrometry of large biomolecules*, *Science* **246** (1989), no. 4926 64–71.

[93] F. Hillenkamp, M. Karas, R. C. Beavis, and B. T. Chait, *Matrix-assisted laser desorption/ionization mass spectrometry of biopolymers*, *Analytical chemistry* **63** (1991), no. 24 1193A–1203A.

[94] S. Brünken, F. Lipparini, A. Stoffels, P. Jusko, B. Redlich, J. Gauss, and S. Schlemmer, *Gas-phase vibrational spectroscopy of the hydrocarbon cations l-C_3H^+, HC_3H^+, and c-$C_3H_2^+$: Structures, isomers, and the influence of ne-tagging*, *The Journal of Physical Chemistry A* **123** (2019), no. 37 8053–8062.

[95] U. Jacovella, E. Carrascosa, J. T. Buntine, N. Ree, K. V. Mikkelsen, M. Jevric, K. Moth-Poulsen, and E. J. Bieske, *Photo-and collision-induced isomerization of a charge-tagged norbornadiene–quadricyclane system*, *The Journal of Physical Chemistry Letters* **11** (2020), no. 15 6045–6050.

[96] H. Naraoka, Y. Takano, J. P. Dworkin, Y. Oba, K. Hamase, A. Furusho, N. O. Ogawa, M. Hashiguchi, K. Fukushima, D. Aoki, *et. al.*, *Soluble organic molecules in samples of the carbonaceous asteroid (162173) ryugu*, *Science* **379** (2023), no. 6634 eabn9033.

[97] D. Garay-Ruiz, M. Álvarez-Moreno, C. Bo, and E. Martínez-Núñez, *New tools for taming complex reaction networks: the unimolecular decomposition of indole revisited*, *ACS Physical Chemistry Au* **2** (2022), no. 3 225–236.

[98] E. K. Campbell, M. Holz, D. Gerlich, and J. P. Maier, *Laboratory confirmation of C_{60}^+ as the carrier of two diffuse interstellar bands*, *Nature* **523** (2015), no. 7560 322–323.

[99] S. Chakrabarty, M. Holz, E. K. Campbell, A. Banerjee, D. Gerlich, and J. P. Maier, *A novel method to measure electronic spectra of cold molecular ions*, *The journal of physical chemistry letters* **4** (2013), no. 23 4051–4054.

[100] O. Asvany, S. Brünken, L. Kluge, and S. Schlemmer, *Coltrap: a 22-pole ion trapping machine for spectroscopy at 4 K*, *Applied Physics B* **114** (2014) 203–211.

[101] P. C. Schmid, O. Asvany, T. Salomon, S. Thorwirth, and S. Schlemmer, *Leak-out spectroscopy, a universal method of action spectroscopy in cold ion traps*, *The Journal of Physical Chemistry A* **126** (2022), no. 43 8111–8117.

[102] P. F. Staanum, K. Højbjerre, P. S. Skyt, A. K. Hansen, and M. Drewsen, *Rotational laser cooling of vibrationally and translationally cold molecular ions*, *Nature Physics* **6** (2010), no. 4 271–274.

[103] R. Glöckner, A. Prehn, B. G. Englert, G. Rempe, and M. Zeppenfeld, *Rotational cooling of trapped polyatomic molecules*, *Physical review letters* **115** (2015), no. 23 233001.

[104] A. Lambrecht, J. Schmidt, P. Weckesser, M. Debatin, L. Karpa, and T. Schaetz, *Long lifetimes and effective isolation of ions in optical and electrostatic traps*, *Nature Photonics* **11** (2017), no. 11 704–707.

[105] D. Hume, C. Chou, D. Leibrandt, M. Thorpe, D. Wineland, and T. Rosenband, *Trapped-ion state detection through coherent motion*, *Physical review letters* **107** (2011), no. 24 243902.